Transient Absorption Spectroscopy Of Metal Complexes: Dithizonatophenylmercury(II) And Derivatives

By

Gurthwin Wendell Bosman

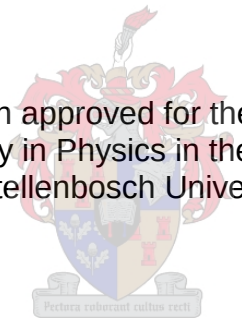

Dissertation approved for the degree of
Doctor of Philosophy in Physics in the Faculty of Science
at Stellenbosch University

Promoter: Prof. H. Schwoerer
Co-promoters: Prof. E.G. Rohwer

December 2012

Declaration

By submitting this thesis electronically, I declare that the entirety of the work contained therein is my own, original work, that I am the owner of the copyright thereof (unless to the extent explicity otherwise stated) and that I have not previously in its entirety or in part submitted it for obtaining any qualification.

Dedicated to my Parents.

Abstract

The availability of laser systems capable of generating ultrashort optical pulses in the visible spectral range have made it possible to study molecular species with a temporal resolution in the order of intra-molecular dynamics which previously were not accessible. Henceforth, in this study a popular pump-probe technique called ultrafast transient absorption spectroscopy (UTAS) is employed to study the initial photochromic reaction of metal complex, dithizonatophenylmercury (II) (DPM) under various conditions. These conditions include the use of different solvents and electronically altering DPM by the addition of substituents with specific electron affinity properties.

For this study the photochromic behaviour of DPM dissolved in methanol is used as standard. Using this standard, the initial photochromic reaction after ultrafast excitation within less than 100 fs caused a radiationless photoreaction with a time constant of about 2 ps, which is interpreted as C=N isomerization along the twist coordinate. It is found that during this isomerization reaction an orthogonally twisted intermediate state was formed and observed through its excited-state absorption, which funnels through a conical intersection onto the ground state potential. Once here, bifurcation along pathways towards the ground states of the reactant and product configurations occurs. This was the first observation of photochromism for DPM in a strong polar solvent such as methanol.

From the results of the test compound in methanol, comparisons to the photo-behaviour of DPM dissolved in deuterated methanol and dichloromethane are made. What is established is that changing the solvent resulted in slightly different decay times as well as spectral shifts in the absorption profile which suggested that the potential energy surface of the excited state is modified. This is similar to the results found from the electronically altered DPM species. Here the entire photoreaction is found to either be sped up (1 ps) or slowed down (4 ps) depending on the sample investigated.

Previous studies on the photochromicity of DPM like systems concluded that apart from the photo-activated forward reaction, a back reaction occurs in the absence of light. Therefore a detailed look at the back reaction of DPM and its derivatives are also studied. This is done by temporally monitoring the absorption change of the photo-product as it converts back to the reactant. In doing so the lifetime of the photo-product is determined and found to differ greatly depending on the solvent and substituent used. Lastly, in assuming that the back reaction follows first order kinetics, an Arrhenius type measurement on the photo-product of DPM is conducted. The result of this measurement is that a potential energy barrier of 64.8 kJ/mol is overcome in the back reaction.

The measurements performed and the results obtained from the photochromicity of DPM contribute to the understanding of photo-induced *cis-trans* isomerization reactions about a C=N double bond.

Uittreksel

Die beskikbaarheid van laser sisteme in staat om ultrakort optiese pulse te genereer in die sigbare spektrale gebied, het die studie van molekulêre spesies met 'n tydresolusie in die orde van intra-molekulêre dinamika wat voorheen nie toeganklik was nie. Voortaan, in hierdie studie word 'n populêre aktiveer-interogeer tegniek genaamd ultravinnige tydafhanklike absorpsie spektroskopie (UTAS) aangewend om die aanvanklike fotochromiese reaksie van die metaal kompleks, ditisoonfenielkwik (II) (DFK) onder verskillende kondisies te bestudeer. Hierdie kondisies sluit in die gebruik van verskillende oplosmiddels en die elektroniese verstelling van DFK deur die toevoeging van substituente met spesifieke elektron affiniteit eienskappe.

Vir hierdie studie word die fotochromiese gedrag van DFK, opgelos in metanol, as standaard gebruik. Met hierdie standaard, word gevind dat die aanvanklike fotochroom reaksie na ultravinnige opwekking binne minder as 100 fs, 'n stralingslose fotoreaksie met 'n tydkonstante van 2 ps veroorsaak. Hierdie fotoreaksie word verklaar as die C=N isomerisasie met betrekking tot die draai koördinaat. Daar is ook gevind dat gedurende hierdie isomerisasie reaksie, 'n ortogonaal verdraaide oorgangstoestand gevorm word wat waargeneem is deur sy absorpsie in die opgewekte toestand wat tregter deur 'n koniese kruispunt na die potensiaal van die grondtoestand. By hierdie punt vurk die proses na die grondtoestande van die reaktant en die produk vorme. Dié was die eerste waarneming van fotochromisme van DFK opgelos in 'n sterk polêre oplosmiddel soos metanol.

Vanuit die resultate vir die toets mengsel in metanol word vergelykings getrek tot die fotogedrag van DFK opgelos in gedeureriese metanol en dichlorometaan. Wat hieruit vasgestel is, is dat die verandering in oplosmiddel wel die fotoreaksie beïnvloed deurdat verskillende vervaltye en spekrale verskuiwings in die apsorpsie profiel waargeneem word.

Hierdie verskille dui aan dat die potensieële energie oppervlakte van die opgewekte toestand wel gemodifiseer word. Dit is ook soortgelyk aan die resultate vir die elektronies verstelde BFK spesies. Hier is gevind dat die tempo van die totale fotoreaksie òf toeneem (1 ps) òf afneem (4 ps) afhanklik van die spesifieke spesie wat bestudeer word.

Vorige studies van die fotochromiese gedrag van sisteme soortgelyk aan DFK het gevind dat behalwe vir die fotogeaktiveerde voorwaartse reaksie, daar ook 'n keersy reaksie plaasvind in die afwesigheid van lig. Dus word die keersy reaksie vir DFK en sy derivate ook in detial bestudeer. In hierdie studie word die absorpsie verskille van die fotoproduk tydelik waargeneem soos dit terugkeer na die reaktant. Op hierdie manier word die leeftyd van die fotoproduk bepaal en gevind dat dit grootliks afhang van die tipe oplosmiddel en tipe substituent wat gebruik word.

Ten slote, wanneer daar aanvaar word dat dié keersy reaksie eerste orde kinetika volg, word 'n Arrhenius tipe meting op die fotoproduk uitgevoer. Die resultaat van hierdie meting is dat 'n potensieële enrgie versperring van 64.8 kJ/mol oorkom word in die keersy reaksie.
Die metings wat uitgevoer is en die resultate wat verkry is van die fotochromiese gedrag van DFK dra by tot die verstandhouding van lig-geïnduseerde *cis-trans* isomerisasie reaksies rondom 'n C=N dubbelbinding.

Acknowledgements

My sincere thanks goes to the following people and institutions for their gracious contributions to this work:

- Prof H. Schwoerer and Prof. E. G. Rohwer for their outstanding supervision and for creating an environment in which academic and social growth is inevitable.
- The entire Laser Research Institute family, your steadfast support still amazes me.
- The staff and students at the physics department for especially the thought provoking discussions during tea time.
- Dr Karel von Eschwege for a fruitful collaboration and supplying the samples which were studied within this dissertation.
- Olufemi Olaoye for support on some of the DFT calculations.
- The Department of Science and Technology, the National Research foundation and the Andrew Mellon Foundation for financial support.
- A special mention goes to Pieter Neethling and Marguerite Blignaut for particularly the obligatory coffee sessions, much needed and appreciated.
- To Alexander Heidt for not only being a good friend, but also a helpful colleague.
- Thanks to my Ultrafast Science Laboratory partners, sharing a space earmarked for scientific endeavors has never been this convenient. What a pleasure working with you all.
- All my family and friends across the Rainbow nation. Thanks for your unwavering support and encouragement through the all of the highs and lows.
- And finally to Robyn Philander, no words can describe how grateful I am for having your love and support.

CONTENTS

1. Introduction

What happens when light and matter interact? A seemingly simple question which becomes increasingly more complex when the nature of light and matter is factored in. Answering this question for isolated systems has gradually enhanced our understanding of the world around us. For example, the high efficiency of the human eye to detect light in a wide spectral range typically between 400 nm - 800 nm is due to the ultrafast conformational change which retinal rhodopsin undergoes when photo-activated [1–4]. Rhodopsin is the photoreceptor protein present in the rod and cone cells of all vertebrates. It contains a retinal chromophore which is bonded to an apoprotein through a Schiff base. The retinal chromophore responsible for light harvesting and the initial conformational change is 11-*cis*-retinyl. As seen in figure 1.1, 11-*cis*-retinyl undergoes photo-induced isomerization towards the *trans* form of all-*trans*-retinyl. The isomerization occurs around the C=C double bond at position C11. Leading to the thermally unstable photo-product bathorhodopsin, which is formed in about 200 fs [2].

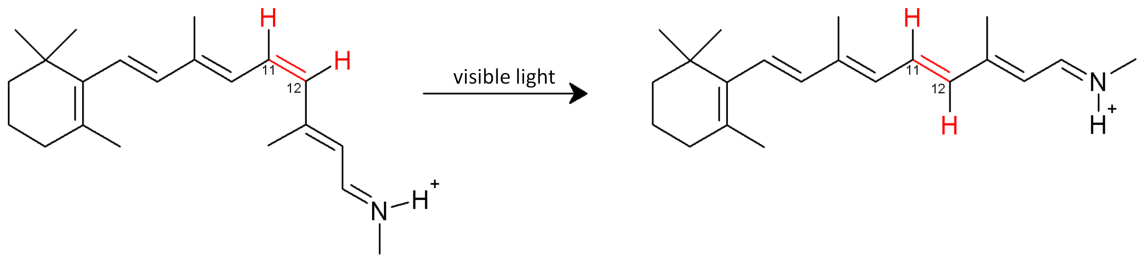

Figure 1.1: Photo-induced isomerization of 11-*cis*-retinyl (left) to all-*trans*-retinyl (right).

This ultrafast transformation of rhodopsin to bathorhodopsin is thus a primary step in the vision process which exemplifies the importance of photo-induced isomerization reactions. *Cis-trans* isomerizations of molecules containing C=C double bonds are rigorously studied both theoretically and experimentally [5–8]. Molecular systems such as olefins, hexatrienes, stillbene and the aforementioned rhodopsin are all examples of C=C double bond isomerization. For all of these, the isomeric pathway is believed to be out of plane rotation. Where the photochemical reaction occurs largely on the excited potential energy surface, which is accessed through adequate photo-excitation. On this excited surface various short-lived intermediate products could be formed which inevitably evolve towards a conical intersection (CI) region. Here funneling through the CI proceeds generally to a local or global maximum on the ground potential energy surface. At this point either products can be formed or the initial reactant can be repopulated.

The specifics of how fast and the type of intermediates formed depends on the substituents on the carbon atoms. When one of the carbon atom's is replaced with a nitrogen atom isomerization is still possible, but it is however a bit more intricate. The reason for this is the presence of electron lone pair on the nitrogen atom. This electron lone pair allows for $\pi \rightarrow \pi^*$ and $n \rightarrow \pi^*$ transitions which becomes important when determining a possible mechanism for activation and deactivation [5]. Furthermore, the C=N double bond permits not only rotation but also inversion as a possible isomeric pathway. In reality however, isomerization might be a linear combination of the two independent motions if allowed.

In this context the molecular system of dithizonatophenylmercury(II) (DPM) was chosen as a test sample. DPM is a mercury dithizonate complex which in solution undergoes isomerization when illuminated with blue-green light. Here the isomerization occurs about a C=N double bond (see figure 1.2). What makes DPM an interesting system to study is the pronounced photochromic effect which accompanies the isomerization [9–11]. Allowing to envision possible applications of DPM in the field of molecular electronics and also as a light harvesting compound. This in essence is compounded by the fact that isomerization is reversible and greatly dependent on the type of solvent (polar, non-polar, etc.) used and on the solution temperature.

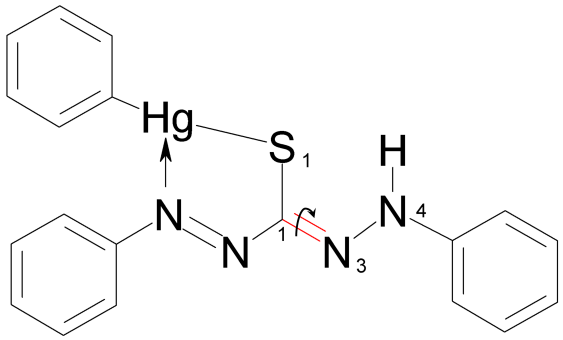

Figure 1.2: Chemical structure of dithizonatophenylmercury(II).

Due to the striking photochromic effect of DPM in solution, conventional ultrafast transient absorption spectroscopy is the preferred (see chapter 2) diagnostic method, which allows for temporal and spectral analysis. Meaning that the lifetimes of electronic states can be accurately determined giving a handle on the times at which intermediate species and products are formed. In order to determine the parameters which influence the photo-induced isomerization of DPM, derivatives of DPM are also investigated. The derivatives are formed through specific substitutions on the phenyl rings attached to the nitrogen rich, dithizone backbone. These substituents influence the π electron delocalization on the backbone which may alter the rate of isomerization in both the forward and backward directions. It is therefore the task of

this dissertation to determine through the use of transient absorption spectroscopy the rate of isomerization in DPM. This includes the identification of possible intermediate species which may indicate a preferential minimum energy pathway. Also, to form a consistent quantum mechanical view of the evolution of the photo-excited system on a potential energy surface and its subsequent deactivation.

2. Ultrafast Transient Absorption Spectroscopy

The study of molecular dynamics in the pico- to femtosecond timescale has nowadays become the standard in ultrafast transient absorption (UTA) spectroscopy [8, 12–15].This is largely due to the need to understand fast molecular processes and the ability to design and build systems capable of investigating it. Independent on the physical process one wishes to investigate, it is best practice that the UTA system have both high temporal and high spectral resolution. Below is the schematic overview of the UTA setup currently being utilized at the Laser Research Institute (LRI), Stellenbosch University. A Clark-MXR CPA 2101 with pulse energies in the range of 1 mJ, repetition rate of 1 kHz, pulse duration of 150 fs centered at 775 nm is used as source for both a noncollinearly phased matched optical parametric amplifier (NOPA) and a white light generation setup in order to perform transient measurements. The detail of the NOPA and the white light setup will be addressed shortly.

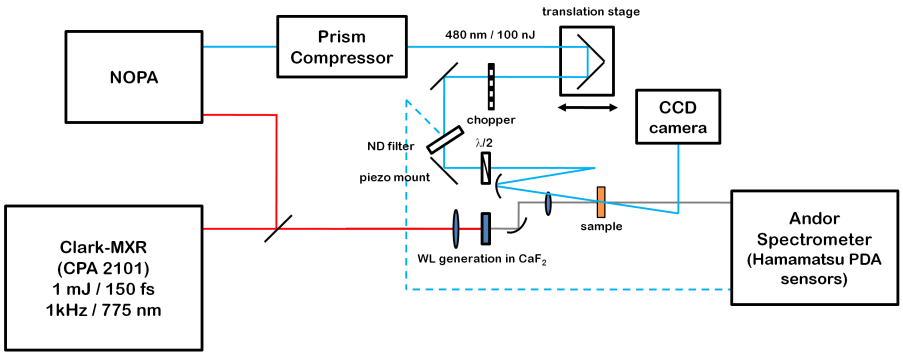

Figure 2.1: Schematic overview of the home-built ultrafast transient absorption setup.

As is common with most transient absorption setups, the basis is grounded in the pump-probe method. This is a method in which a molecular system is activated with a pump pulse and subsequently interrogated by a probe pulse. Optical activation of the molecular ensemble may lead to a variety of effects like phase transition, isomerization, intermolecular charge transfer, intramolecular charge transfer, oxidation, reduction, etc.[3, 16–18]. Therefore to form a dynamic view of the system after activation, the temporal delay between activation and interrogation is changed sequentially. Here it is important to note that for each delay time a new unperturbed system must be investigated. Otherwise monitoring a previously irradiated system might result in erroneous data. The following sections will focus on the generation of ultrashort pump and probe pulses as well as the data collection for time resolved absorption measurements.

2.1 Noncollinearly phased matched Optical Parametric Amplification

All of the pump-probe experiments in this work were made possible using tunable pulses generated in a NOPA. Depending on the requirements of the measurement, the NOPA can be adjusted to emit pulses with various center wavelengths and bandwidths. In figure 2.2 the general scheme of the NOPA is indicated. In this scheme, pump and seed pulses interact with a nonlinear optical crystal β-barium borate (BBO) resulting in the instantaneous generation of an idler, amplified seed (signal) and depleted pump pulse. As seen in figure 2.2, due to the noncollinear nature of this setup, the three generated pulses are spatially separated. Thus nullifying the need of expensive dielectric filters or dispersion elements. What should also be stated that the core of the NOPA process is energy and momentum conservation. Energy conservation ensures that the photon energy of the pump pulse equals the sum of the photon energies for the seed and the idler. Whilst momentum conservation is adhered to through phase matching, which is responsible for the overall generation of broad bandwidth pulses.

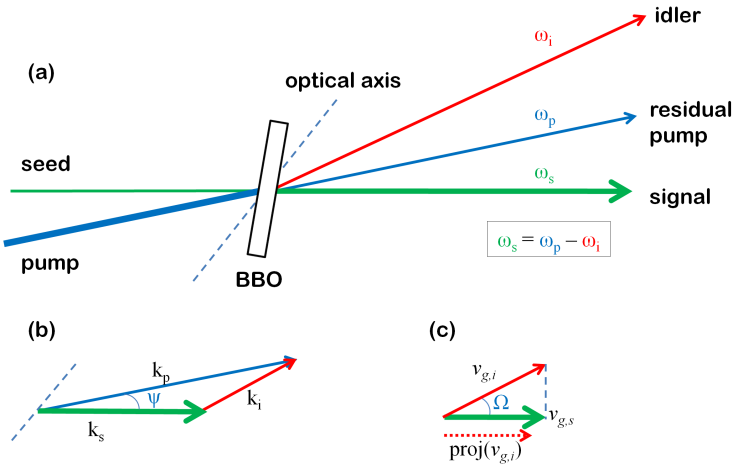

Figure 2.2: Schematic of a noncollinear phased matched optical parametric amplification (a).The wave vector geometry shows the case of zero wave vector mismatch, for the pump k_p, the seed k_s and the idler k_i (b). The group velocity of the idler pulse $v_{g,i}$ is projected into the same direction as that of the seed's group velocity $v_{g,s}$.

In order to understand how this is accomplished, consider the expansion of the wave-vector mismatch Δk of the amplified seed in powers of the seed wavelength detuning $\Delta\lambda_s$,

$$\Delta k = \Delta k_0 + \frac{\partial \Delta k}{\partial \lambda_s}\Delta\lambda_s + \frac{\partial^2 \Delta k}{\partial \lambda_s^2}\Delta\lambda_s^2 + \cdots . \tag{2.1}$$

Momentum conservation thus implies that for $\Delta k = 0$ both the zeroth expansion coefficient Δk_0 and the wave-vector mismatch dispersion term $\frac{\partial \Delta k}{\partial \lambda_s}$ should vanish for perfect phase matching.

This requirement is equivalent to the condition that

$$v_{g,s} = v_{g,i}\cos(\Omega), \tag{2.2}$$

where $v_{g,s}$ and $v_{g,i}$ are the group velocities of the signal (seeded) and the idler pulse with Ω the angle between them (see figure 2.2 (c)). When group velocity mismatch (GVM) is non-zero for the idler and signal pulse there exists a significant walk-off angle which ultimately results in signal pulse lengthening [19]. For a noncollinear geometry however, the projection of the idler group velocity onto the seed is the only relevance, hence combating GVM leading to no pulse lengthening.

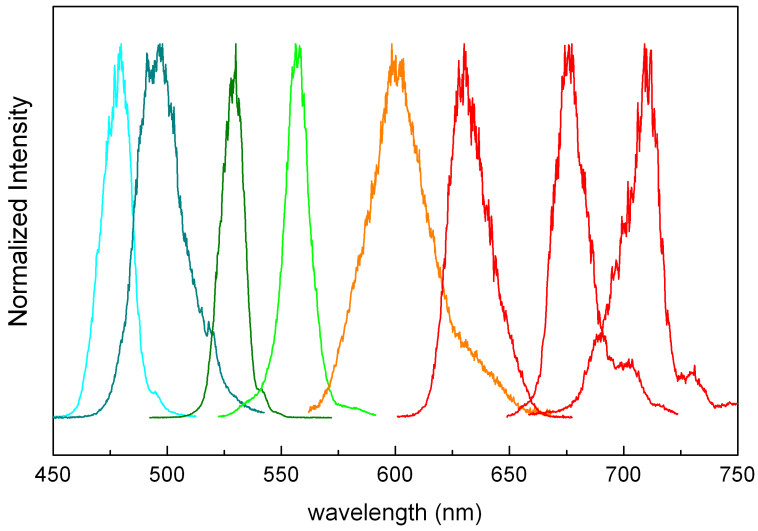

Figure 2.3: Typical spectra of femtosecond pulses generated in the NOPA.

In order to generate a signal with an ultrashort duration (say sub 50 fs) significant spectral bandwidth is required. This is readily seen from the time-bandwidth product (TBP) of an unchirped laser pulse with Gaussian profile (TBP= 0.441). Using this TBP the bandwidth required to generate for example a 20 fs pulse with a center wavelength of 500 nm, is at least 18 nm. Therefore, a single white light (WL) filament generated in a transparent medium is used as seed pulse, but more on the generation of the WL in the following section. Due to the manner in which the WL is generated it has a rather large linear chirp. This linear chirp turns out to be very favourable, because through merely changing the temporal delay of the WL (seed) with respect to the pump pulse in the NOPA, it is possible to preferentially choose a section of the WL to be amplified. In

figure 2.3 the measured spectra of various output pulses from the NOPA are shown.
These generated pulses however are also chirped. Luckily, the largest contribution to the chirp, when considering the temporal or spectral phase as a Taylor expansion, is the quadratic term. This quadratic phase distortion is equivalent to a linear instantaneous phase which can be corrected by using a prism compressor setup (see figure 2.4). The specific prism compressor in

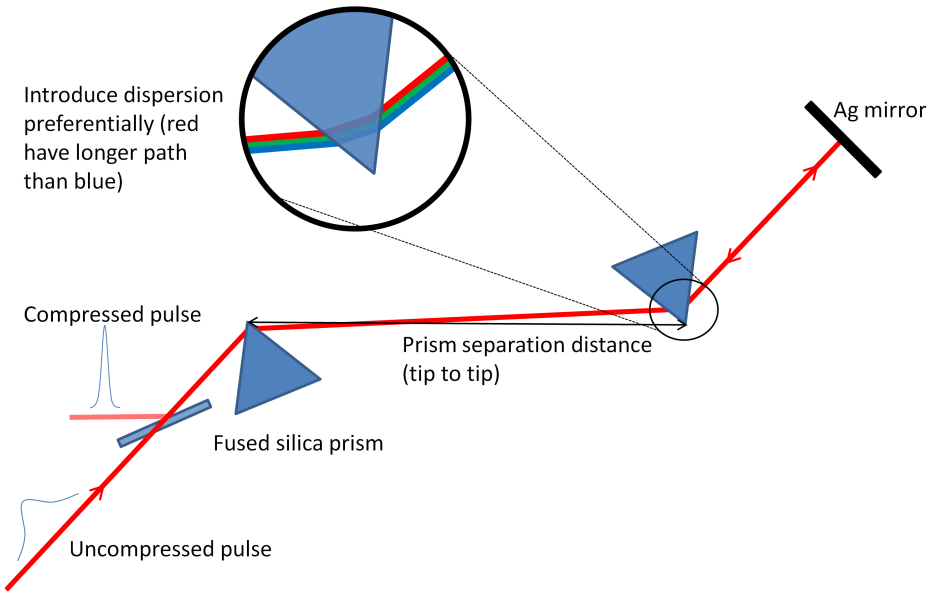

Figure 2.4: Schematic diagram of the prism compressor.

use consist of two fused silica 60° prisms aligned to minimum deviation which coincides with the Brewster angle for the given polarization of the pulses generated by the NOPA. After the light passes through the two prisms it is reflected off a Ag mirror which is slightly tilted forward. Therefore when the light travels back through both prisms it is coupled out at a lower position. This double-pass geometry allows for double the compression and due to the symmetry the spatial mode is not destroyed. In order to obtain compression the separation distance between the two prisms (tip to tip distance) as well as the amount of glass introduced in the second prism is varied. Table 2.1 summarizes typical pulse durations ($\Delta\tau$) determined through a background-free autocorrelation for various compressed NOPA pulses. The data in table 2.1 indicates however that optimum compression of the various NOPA pulse is not achieved. This is seen when comparing the measured pulse duration ($\Delta\tau$) with the Fourier limited pulse duration ($\Delta\tau_{FL}$). One possible reason for this large discrepancy is that the pulses generated in this NOPA might have non-zero nonlinear temporal phase distortions which the prism compressor

Table 2.1: Pulse duration at various NOPA center wavelengths and bandwidths at optimized compressor settings.

λ (nm)	$\Delta\lambda$ (nm)	$\Delta\tau_{FL}$ (fs)$^{\alpha}$	prism separation (cm)	$\perp$ distance from tip of P2$^{\beta}$ (mm)	$\Delta\tau$ (fs)
480	17.98	18.88	58	8	26.71
510	32.72	11.75	66	7	18.37
540	37.70	11.70	66	10	23.65
570	49.09	10.03	76	6	22.70
600	62.42	8.58	72	5	26.31
630	73.41	7.85	90	9	19.07

α : Fourier limited pulse duration for a Gaussian pulse.
β : Second prism in compressor.

is incapable of correcting.

2.2 White Light Generation

The generation of white light in a bulk transparent medium using femtosecond IR pulses has long been studied [20–27]. More recently however, Dharmadhikari et al. reported in 2005 the systematic study of WL generation in large band-gap media like water, barium fluoride (BaF_2), acrylic and Bk-7 glass. Showing that a numerous amount of materials can be used for WL generation, with the only requirements being that it is transparent in the visible region of the spectrum and that it has a non-vanishing odd-order susceptibility $\chi^{(i)}$, $i = 1, 3, 5, ...$[25]. This means that the phenomenon is a highly non-linear optical process in which the modification of the medium by the input pulse results in the spectral broadening of the same pulse. Therefore understanding the process is inherently complex. However, it is understood that the dominant process responsible for spectral broadening in bu lk media is self phase modulation (SPM) [21]. SPM is a direct result of the intensity dependent refractive index $n(I(t))$ and can be seen as the starting mechanism of spectral broadening. To see why this is the case, consider an isotropic medium with a large third-order susceptibility $\chi^{(3)}$. Thus the expression for the refractive index becomes

$$n = n_0 + n_2 I(t) \tag{2.3}$$

where n_0 is the normal wavelength dependent refractive index, n_2 the so-called nonlinear index coefficient which describes the coupling strength between the electric field and the refractive index and $I(t)$ the input pulse intensity which is directly proportional to the square of the electric field $\mathcal{E}(t)$. The nonlinear index coefficient can also be expressed in terms of the third order

susceptibility

$$n_2 = \frac{3\chi^{(3)}}{8n_0} \tag{2.4}$$

showing the interplay between the microscopic medium properties ($\chi^{(3)}$) and the macroscopic quantities (refractive indices). Now to understand what effect a medium with a non-zero third-order susceptibility will have on a laser pulse as it travels through it. The need for solving the electromagnetic wave equation with the third-order polarization vector as the source term arises [20]. For an electric field $\mathcal{E}(z,t)$ propagating through this medium of length z neglecting dispersional effects it can be found that the wave equation with its source term simplifies to

$$\frac{\partial}{\partial z}\tilde{\mathcal{E}}(z,t) = -i\frac{3\omega_l^2\chi^{(3)}}{8c^2k_l} \mid \tilde{\mathcal{E}}^2 \mid \tilde{\mathcal{E}} = -i\frac{n_2k_l}{n_0} \mid \tilde{\mathcal{E}}^2 \mid \tilde{\mathcal{E}} \tag{2.5}$$

where $\tilde{\mathcal{E}}(z,t)$ is the complex electric field, ω_l is the center frequency of the light field, c the speed of light in a vacuum and k_l the wave vector of the incident field. Assuming that $\chi^{(3)}$ is a real quantity, one can substitute $\tilde{\mathcal{E}} = \mathcal{E}\exp(i\varphi)$ into the wave equation (eq. 2.5) which allows one to separate the real and imaginary parts resulting in an expression for the pulse envelope

$$\frac{\partial}{\partial z}\mathcal{E} = 0 \tag{2.6}$$

and for the pulse phase

$$\frac{\partial\varphi}{\partial z} = -\frac{n_2k_l}{n_0} \mid \mathcal{E} \mid^2 . \tag{2.7}$$

The pulse amplitude $\mathcal{E}$ in the coordinate system is constant while traveling with the group velocity due to neglecting dispersional effects. This allows one to solve eq.2.7 through integration resulting in the following expression for the phase,

$$\varphi(z,t) = \varphi_0(t) - \frac{k_ln_2}{n_0}z\mathcal{E}^2(t). \tag{2.8}$$

To visualize this the input pulse intensity and instantaneous frequency $\omega_{inst}(t) = \frac{\partial\varphi}{\partial t}$ is plotted in figure 2.5 . The frequency modulation as seen in figure 2.5 results from the fact that different parts of the input pulse essential interact with different refractive indices. This phase change across the pulse generates new frequency components which broaden the pulse spectrum. In order to characterize the effect of SPM lets define the nonlinear phase shift (NPS) from eq.2.8 as the coefficient of the intensity term ($I(t) \approx \mathcal{E}^2(t)$). Figure 2.6 shows what increasing the NPS does to the input pulse. This suggests that sufficient spectral broadening can be achieved in a medium with a large enough nonlinear refractive index.

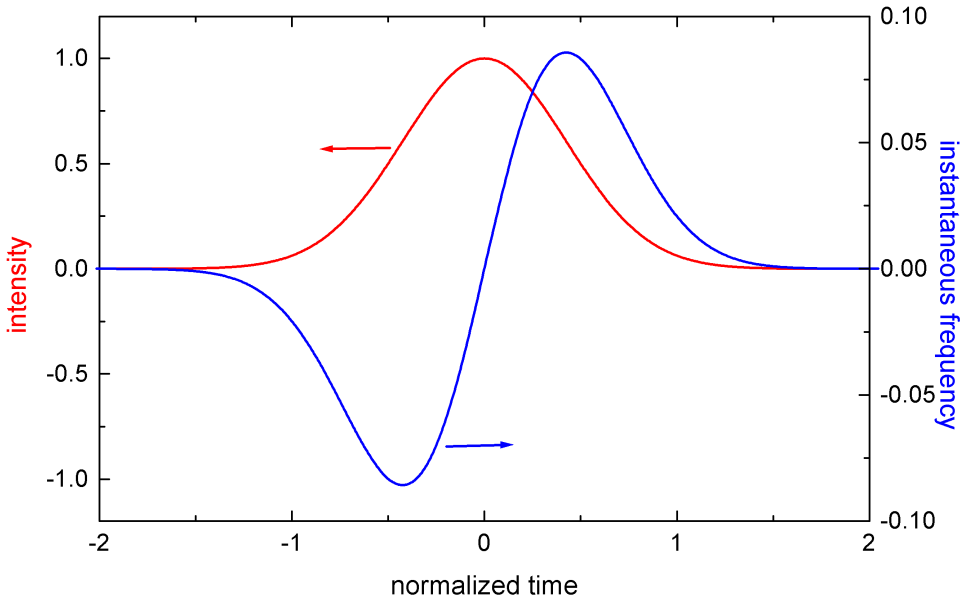

Figure 2.5: Intensity profile and frequency modulation of self-phase modulation.

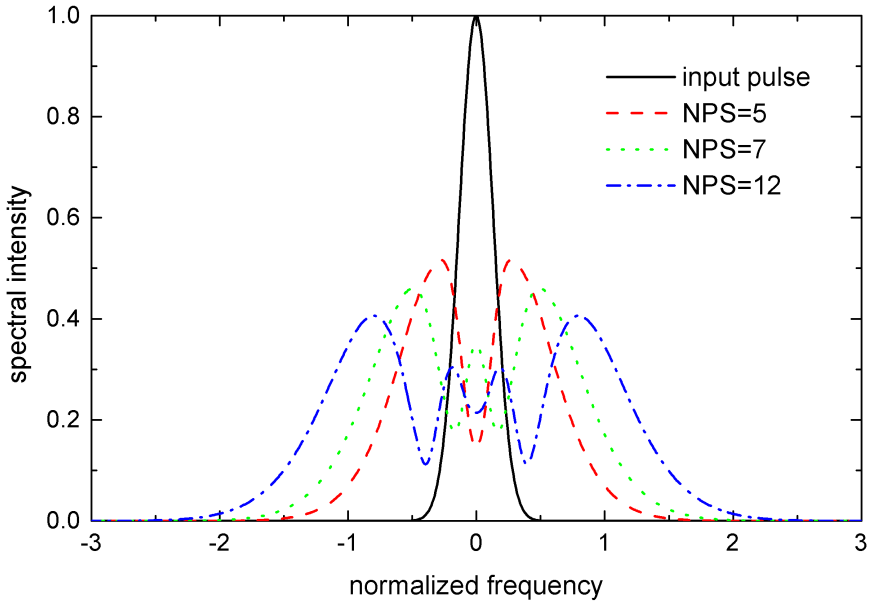

Figure 2.6: Spectrum of self-phase modulated Gaussian pulses at different non-linear phase shift (NPS).

So far we have only considered the time dependent aspect of the intensity refractive index and neglected the spatial (transverse) dependence. The intensity distribution of a ultrashort laser pulse impinging on a medium with large n_2 results in a transverse variation of the refractive index. This variation leads either to focusing or defocusing. In the case of self-focusing it is important to note that this spatial confinement of the laser pulse as it travels through the medium only occurs if a quantity called the critical input power P_{crit} is exceeded [28, 29]. Therefore, when the critical power

$$P_{crit} = 3.72 \frac{\lambda_0^2}{8\pi n_0 n_2} \tag{2.9}$$

is reached, the beam diameter decreases such that the intensity becomes sufficiently large to initialize SPM. Self-focusing however does not continue indefinitely and is limited by multi-photon absorption (MPA) and subsequent ionization which generates free electrons[1] causing defocusing [23]. As defocusing now increases the intensity distribution, MPA decreases and allows for self-focusing and SPM to initiate again. This pattern of self-focusing and defocusing continues along the medium resulting in the generation of a single white light filament.

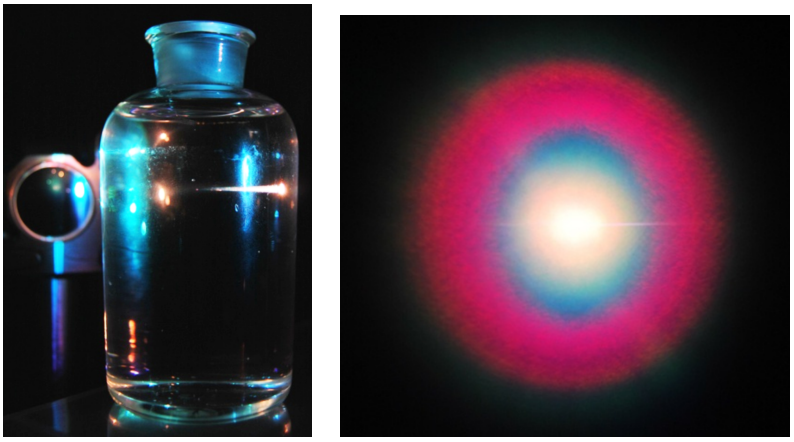

Figure 2.7: Picture of white light being generated in water (left) and its spatial distribution (right).

This generated white light filament has a conical emission with a central bright white spot and is surrounded with a red halo (see figure 2.7) and it also shares the same polarization as the input pulse.

In figure 2.8 the white light generated in 3 mm thick calcium fluoride (CaF_2) and sapphire crystals are shown. Both of the generated spectra cover the visible spectrum with the one in CaF_2 extending further into the UV. Also the generated white light for both tails off around 900 nm, which is not due to the low spectral responsivity of the detector in the IR. The shaded

[1] The change in the refractive index due to free electrons is negative, thus limiting self-focusing.

area where there is a dramatic drop in intensity is a result of spectrally filtering the center pump wavelength (775 nm) of the CPA pulse. This is done as to eliminate damage by this intense pulse on subsequent optics and molecular samples in the case of transient absorption measurements.

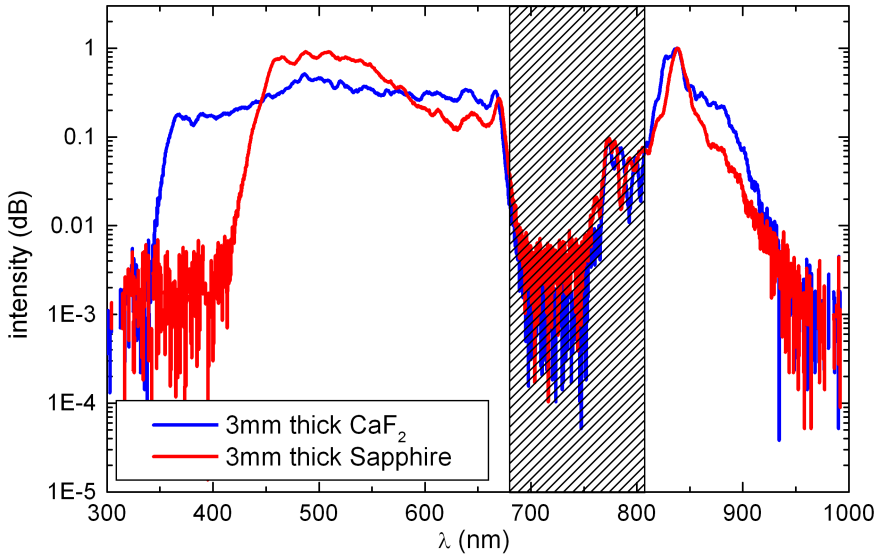

Figure 2.8: Spectra of white light generated in 3 mm thick bulk CaF_2 and sapphire.

The above description of white light generation includes the dominant processes involved but is however not the full picture. To date, it is generally accepted that white light generation is in all probability the result of the interaction between SPM, self-focusing, GVD, intensity clamping, self-steepening, anti- Stokes spectral broadening and conventional four-wave mixing [23, 25, 26, 30–35].

2.3 Transient Measurement Data Collection

The measurement of reliable transient absorption spectra depends on meeting numerous requirements. In this section the requirements using the UTA system at the LRI (see figure 2.9) as model will be discussed. Firstly, information about both the spectral signatures and the lifetime of the particular photo-activated process in a molecular sample should roughly be known. The change in spectral signatures should occur within the wavelength window (340 - 680 nm) of the UTA system and the lifetime of the process should be far less than the period (1 ms) of the laser source. If the photo-activated process under investigation is orders of magnitude smaller than the period of the laser, subsequent measurement of a pre-irradiated sample volume, pro-

vided that the sample has not been irrevocably altered, is possible. If this is not the case, the previously pumped and probed volume has to be removed. In the home-built UTA system at the LRI, a thin flow cell with optical pathlength of 200 μm and an in-line rotary pump (HNP Mikrosysteme GmbH: MZR 2921) connected to a reservoir with teflon tubing (i.d. 5 mm) is used to secure a new pump volume to be analyzed. To verify this, a simple measurement to determine the amount of liquid that the flow cell apparatus transfers at typical pump settings is done. The result of this measurement is that a transfer (flow) rate of 400 nL/ms is achieved, which due to the geometry of the flow cell and its narrow optical pathlength is substantially higher in the cell itself[2]. Now if the pump beam has a diameter at the cell of 200 μm, this means that a volume[3] of approximately 2π nL should be replaced in 1 ms. This required flow rate 2π nL/ms is far less than the rate of the system and hence achieves its purpose. Besides the increased flow rate through the flow cell, the effect of group velocity mismatch (GVM) through the cell is also decreased due to the short optical pathlength as well as the type of material it is made from. GVM describes the relative group velocities of the specific optical frequencies traveling through a transparent medium. Minimizing the effect of GVM ensures that the different wavelength components all have roughly the same group velocities, which will ultimately increase the temporal resolution.

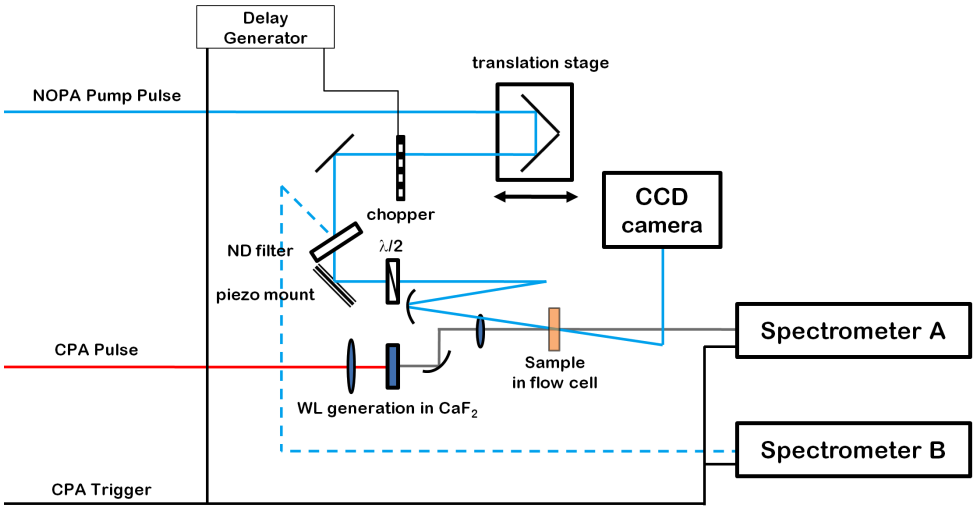

Figure 2.9: More detailed schematic overview of the UTA setup.

The pump pulse which initiates photo-induced reactions in the test sample is temporally delayed with respect to the probe pulse using retro-reflector (two UV enhanced Ag mirrors moun-

[2]According to flow dynamics, the transfer (flow) rate increases when the flow cross section decreases.

[3]The calculation of the volume is done through approximating the illuminated volume as a cylinder. The diameter of the cylinder is the pump beam diameter and the height is equal to the optical pathlength of the cell.

ted 45°) mounted on a linear translation stage. This allows for unambiguous control of the time delay. In order to generate an on-off signal for referencing, the pump beam passes through an optical chopper (Thorlabs Optical Chopper: MC1000A) triggered by the CPA laser through a delay generator (Stanford Research Systems: DG 645) and set to half the laser repetition rate at the chopper control unit. The delay generator is used to optimize the phase of the chopper rotation as to ensure that every second pump pulse is efficiently blocked (on-off signal). The input pulse energies of the pump pulse on the sample is carefully controlled using a linear neutral density filter. This filter is aligned slightly off-axis such that the reflection is directed to a optical fiber with a diameter of 100 μm which is coupled to one of the two spectrometers (Andor Czerny-Turner Spectrograph model 163 fitted with a Hamamatsu photo-diode array (PDA) sensor by Entwicklungsbüru) in the setup. The transmitted pump pulse is then reflected off a piezo controlled mirror and passes through a lambda half ($\frac{\lambda}{2}$) wave plate set at magic angle[4]. At this point the pump pulse is focused onto the sample with a spherical mirror ($f = 200$ mm). After propagating through the sample cell the pulse is imaged onto a CCD camera where the pump position is monitored for subsequent control of the pump-probe overlap through correction of the piezo mirror mount during a transient measurement.

White light generated in a 3 mm thick CaF_2 crystal, serves as probe pulse. Unfortunately however CaF_2 has a very low damage threshold, which when reached causes WL generation instabilities. In order to combat this, the crystal is continuously translated as to increase the WL generation stability. The specific translation of the crystal should be done in a way in which the linear polarization of the white light across the entire spectrum and over time is conserved. This means that the orientation of the crystal axes relative to the fundamental near IR pulse should be kept constant. This is easily achieved by moving the crystal in a circular translation[5] rather than a circular rotation. After WL generation and collimation with a off-axis parabolic mirror ($f = 50$ mm) the probe pulse passes through a 0° HR 775 nm mirror which filters out the remnant fundamental. After which its focused with a UV lens ($f = 100$ mm) to a size smaller then 50 μm onto the sample cell at the same spatial position of the pump pulse (focus size ¿ 100 μm) with a non-collinear geometry at an angle of roughly 10°. The transmitted probe pulse is then imaged onto a 300 μm diameter fiber coupled to the second spectrometer which is on a common clock with the first spectrometer.

During an UTA measurement every probe pulse is recorded and analyzed using National Instruments LabView 8.5 software. The software determines which transmitted probe pulse has

[4]The magic angle $\theta_m = 54.7°$, is the relative angle between the pump and probe pulse polarizations to allow UTA spectra free of rotational reorientation of the pumped molecular sample.

[5]Here circular translation refers to translating the crystal around an axis in a circular motion without rotating it.

traveled through an activated sample (T^*) and an unactivated sample (T) by monitoring the on-off signal from the pump pulse spectrum. This is only possible because the two spectrometers which monitors the pump and probe pulses are synchronously clocked. The transmittance of the probe pulse is related to the optical density OD in the following way

$$T = 10^{-\mathrm{OD}}, \tag{2.10}$$

where according to the Beer-Lambert law for linear absorption $\mathrm{OD} = \varepsilon c l$, with ε being the molar absorptivity, c the concentration of the molecular sample and l the pathlength of the cuvette. The change in the optical density $\Delta\mathrm{OD}$ due to sample activation through interaction with the pump pulse is obtained from the ratio of the transmittance as

$$\begin{aligned} \tfrac{T^*}{T} &= 10^{-\mathrm{OD}^*+\mathrm{OD}} = 10^{-\Delta\mathrm{OD}} \\ \Delta\mathrm{OD} &= -\log\left(\tfrac{T^*}{T}\right). \end{aligned} \tag{2.11}$$

Note that $\Delta\mathrm{OD} = \mathrm{OD} - \mathrm{OD}^*$ and that it is implicitly wavelength λ and delay τ dependent $\Delta\mathrm{OD}(\lambda, \tau)$. The λ dependence is because the transmittance is spectrally resolved in a spectrometer and the τ dependence comes from the optical time delay between the pump and probe pulse. Here the important subtlety that the time taken to change the delay during a measurement is unimportant, which permits slow detection of the probe pulse. However alot of factors are taken into account in choosing an appropriate time between subsequent delays. The first factor is the number of spectra's which are averaged over at a given delay time. In a typical measurement this number is 1000, meaning that it takes the system atleast 1 s (1 ms laser period) to record the averaged data. The second factor is the computing time, because depending on the computing power of the CPU extra time should be taken before moving to the next delay time. The last factor is the time required to change delay, this envolves moving the retro-reflector which is mounted on the linear translation stage. Taking all of this into account the time between subsequent delays is varied between 2 - 5 s resulting in typical measurement times of 15 - 40 minutes depending also on the number of delay times chosen.

2.4 Specifications of the UTA setup

In this section the various specifications of the UTA setup at the LRI will be addressed. This includes information about the limitations of the system with regards to the white light chirp, the temporal resolution and the detection limit.

2.4.1 White Light Chirp

As discussed previously, the white light generated in both sapphire and calcium fluoride are inherently chirped. This dispersion in the group velocity of the different spectral components within the white light pulse also just worsen as it propagates in air and through optics. In the UTA setup there is no white light compression, however the optics used to collimate, steer and focus the white light is chosen as to minimize GVD. In order to measure the chirp of the white light, an UTA measurement is done with the solvent dichloromethane as sample. Figure 2.10 shows this transient measurement for dichloromethane pumped with the NOPA pulse set to a center wavelength of 480 nm and probed with white light generated in 3 mm thick sapphire. The intense feature across the entire spectrum is the coherent artifact which predominantly stems from the nonlinear interaction of the pump and probe pulses in the solvent at temporal overlap. The particular nonlinear interaction includes phenomena like two-photon absorption, stimulated Raman amplification and cross-phase modulation [36].

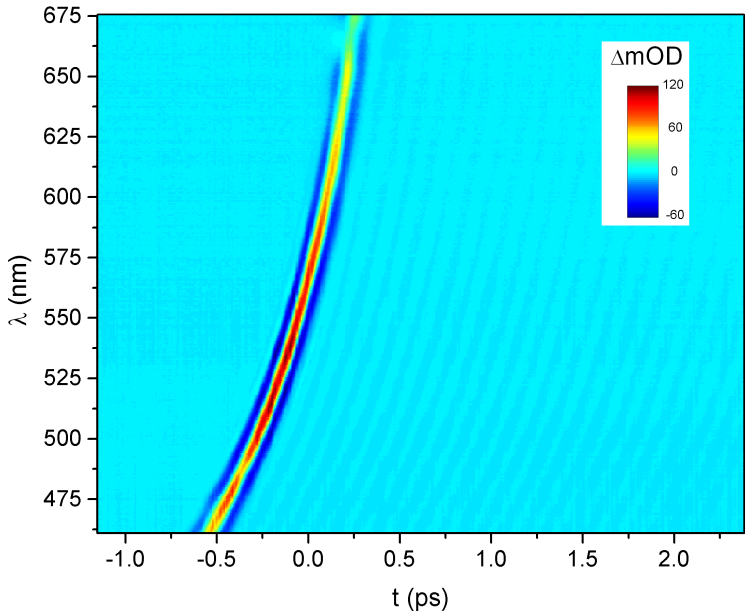

Figure 2.10: UTA measurement of dichloromethane. White light is generated in a 3 mm thick sapphire and pump pulse is set to 480 nm.

The first two is generally caused through the application of ultrashort pump pulses (sub 100 fs) which intrinsically have high pump power densities ($> 10\ \mathrm{GW/cm^2}$). Whilst the third arise due to the broad spectral range of the probe pulse together with its large linear chirp. The position in both time and wavelength of the maximum of this artifact is chosen as the point of overlap between the pump and probed pulse, thus revealing the white light chirp. In order to

quantify this chirp, a 5^{th} order polynomial is fitted to the overlap positions (see figure 2.11). The coefficients as indicated on the figure 2.11 of the polynomial fit describes the nature of the chirp and is hence used to correct the temporal overlap problem[6] in all subsequent UTA data.

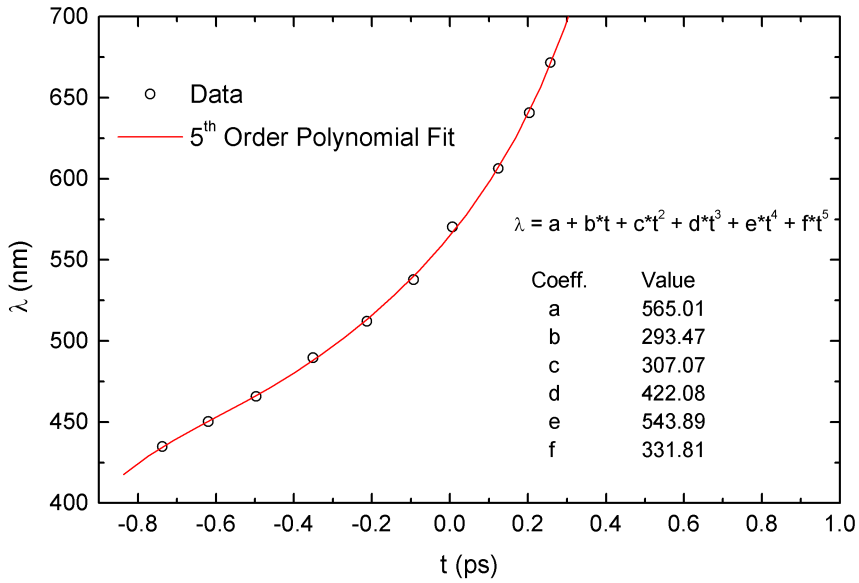

Figure 2.11: 5^{th} Order polynomial fit of the white light chirp.

What should also be mentioned is that the white light chirp is positive. Here this means that the red part of the white light spectrum of the probe pulse travels ahead of the blue part in time. To understand how this is determined from figures 2.10 & 2.11, it is important to note that during the UTA measurement the pump pulse temporally scanned over the probe pulse from times before overlap to times after overlap. Meaning that the spectral components of the white light in the rear is first to interact with the pump pulse, which leads to the chirp having its current form.

2.4.2 Temporal Resolution

The temporal resolution of the UTA system is estimated as the full width at half maximum (FWHM) of the coherent artifact obtained form the flow cell when filled with dichloromethane. Thus to determine the resolution qualitatively, the second derivative of a Gaussian function is chosen to fit the transient behaviour of the artifact. The kinetics trace in figure 2.12 is taken from the UTA data of dichloromethane at 600 nm. From the fit in figure 2.12 it is determined that the

[6] Temporal overlap occurs at different spectral positions.

temporal resolution (i.e. FWHM of Gaussian) is roughly 70 fs.

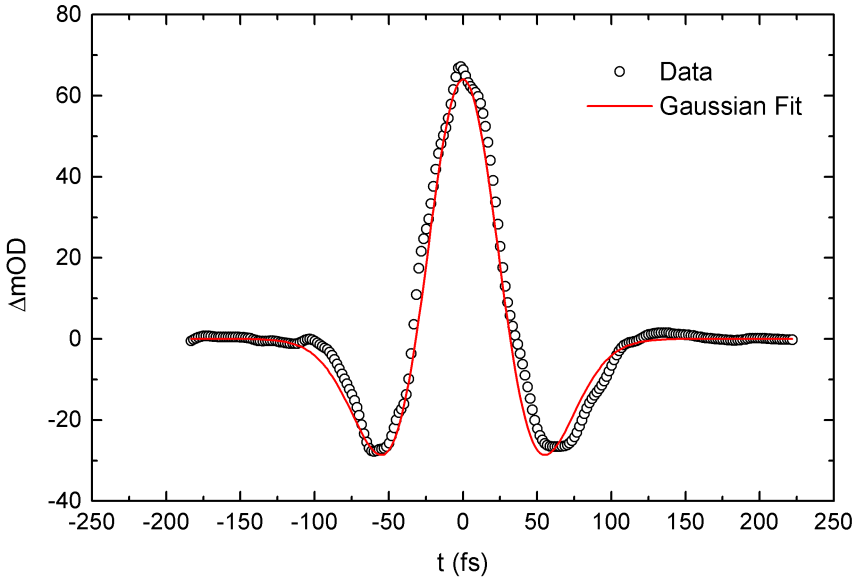

Figure 2.12: Kinetic trace and Gaussian fit for the UTA measurement of dichloromethane at 600 nm.

An analogous method to determine the temporal resolution of the UTA setup, is to generate stimulated impulsive Raman scattering (SIRS) [37]. In this method the ultrashort pump pulse activates Raman modes in the solvent. The vibration of these modes result in a modification of the refractive index of solvent such that oscillation are generated in the kinetic trace. These oscillations are clearly visible in figure 2.10 and have a period in the order of 100 fs. Therefore the temporal resolution is definitely less than this period, because these oscillations are observable.

2.4.3 Detection Limit

The transient absorption signal before pump-probe overlap gives information about the pulse to pulse fluctuations of the probe light. This is because no transient behaviour is expected in this region seeing that the sample is effectively probed without being pumped. Therefore any fluctuantions here will persist even after overlap, limiting the detection of optical density changes. Keeping this in mind, a general definition of the detection limit of the system is as the variance in the transient absorption signal before pump probe overlap. From this definition one finds that the detection limit is roughly 10^{-4} (see figure 2.13).

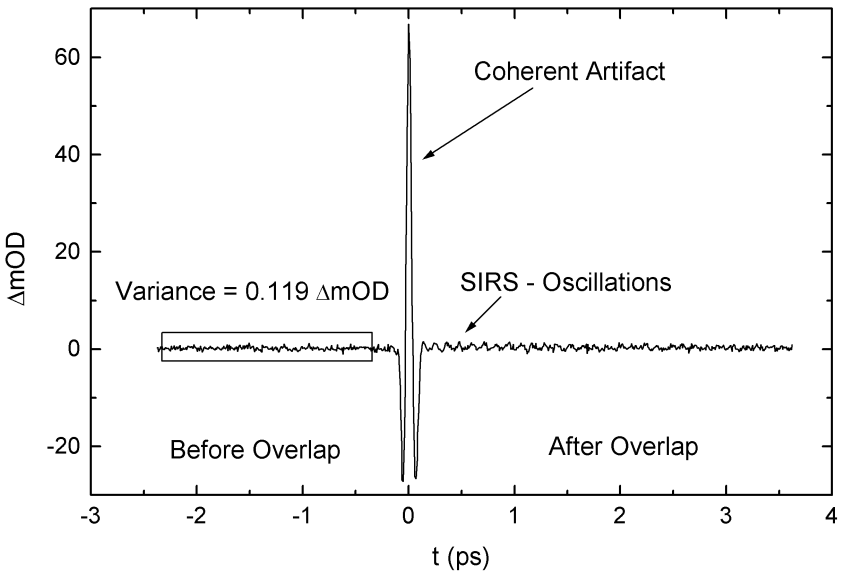

Figure 2.13: Kinetic trace of dichloromethane at 600 nm.

3. The Process of Nonradiative Deactivation

When a molecular system is electronically excited, the lifetime of this new state is short and can generally be deactivated through various processes [4, 5, 38–43]. In this chapter both the photophysical and photochemical dissipation of this excess energy will be consider. The terms photophysical and photochemical are not readily distinguishable but here we limit the former to deal with alternative states of the same molecule where the latter deals with the conversion of a molecule into another chemical form. The molecular system which this dissertation is concerned with is the photochromic metal complex, dithizonatophenylmercury(II) - DPM (see figure 3.1). In DPM isomerization is initiated by an incident photon of correct energy resulting in a product with a distinctly different absorption spectrum than that of the reactant. The specifics of this photoreaction will be addressed in the following chapters, but at this stage it is worthwhile to mention that the photochromism of DPM constitutes both photochemical and photophysical processes.

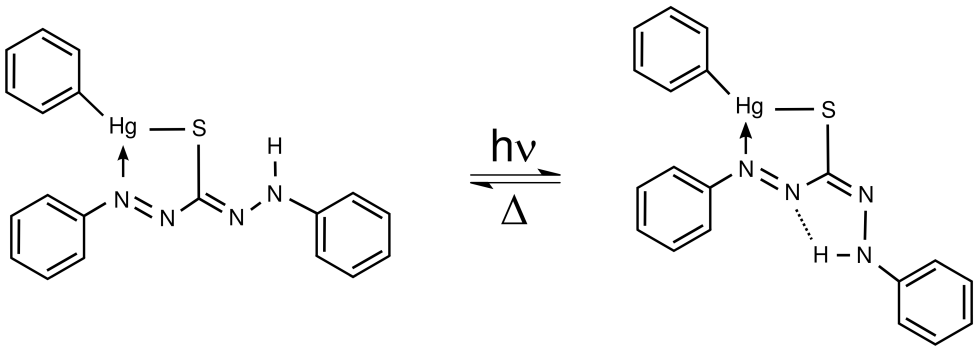

Figure 3.1: Isomerization of dithizonatophenylmercury(II).

In the description of nonradiative deactivation, both unimolecular processes and bimolecular processes will be considered. Bimolecular processes govern the transfer of the excess energy to the surrounding environment. A popular bimolecular process is that of solvation, where solvent relaxation of the molecule effectively lowers (or increases) its excited state. In the case of a fluorophore this results in a measurable Stoke-shift (or Anti-Stoke) [44, 45]. It is also possible to study the degree of solvation by varying the solvent polarity, proticity, acidity, viscosity and temperature.

The numerous unimolecular processes possible after light absorption can be summarized in a Jablonski diagram (see figure 3.2). The diagram shows the singlet ground state S_0, the first and second excited singlet states S_1 and S_2, as well as the triplet state T_1 and T_2.

In the case of polyatomic molecules where a non-harmonic potential for the various electronic states is assumed, the vibrational level spacing decreases with increasing energy. This decrease of vibrational level spacing leads to the increase of state density. For simplicity, the rotational levels have been omitted. Absorption (Ab) is shown as straight arrows, fluorescence (Fl) and phosphorescence (Ph) as dashed arrows and the nonradiative processes as dotted arrows.
The two radiative processes namely fluorescence and phosphorescence differ due to the level from which the transition to the ground state occurs. Fluorescence is said to be a spin-allowed transition while phosphorescence is a spin-forbidden transition. The nonradiative processes can also be categorized in terms of the change in multiplicity[7]. If the multiplicity after a transition remains the same it is refereed to an internal conversion (IC) whereas if it changes it is called intersystem crossing (ISC).

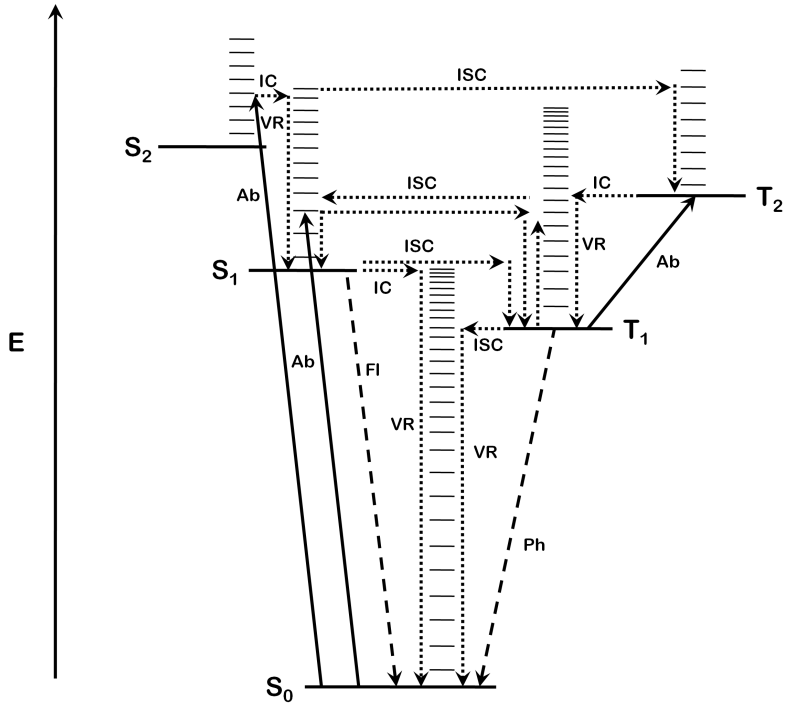

Figure 3.2: The Jablonski diagram for unimolecular reactions. The process of absorption (Ab) is indicated by straight arrows and the radiative processes of fluorescence (Fl) and phosphorescence (Ph) are shown as dashed arrows. The nonradiative processes namely internal conversion (IC), intersystem crossing (ISC) and vibrational relaxation / redistribution (VR) are drawn as dotted arrows.

[7]Multiplicity is defined as 2S+1, where S is the total angular spin momentum. It is used in quantum mechanics to discriminate between degenerate wavefunctions that differ only in the orientation of their respective angular spin momenta.

It can be seen from figure 3.2 that after the absorption of a photon with a suitable energy the molecule can either be in a vibrational level of the first electronic singlet excited state S_1 or a vibrational level on the second electronic singlet excited state S_2. Once here energy dissipation may initially follow different paths. Considering firstly deactivation from the excited S_2 state. Here deactivation starts with internal conversion to a vibrationally excited S_1, followed by vibrational relaxation (VR) to the lowest vibrational level of S_1. This relaxation process in liquid solutions is generally very fast (in the order of a few picoseconds) and can be interpreted as the loss of excess vibrational energy through collisions with the solvent molecules [5]. For the excited vibronic S_1 state, VR to the lowest vibrational level in S_1 competes with ISC to either the first (T_1) or second (T_2) triplet state. On the vibrational ground state of S_1 the molecule can reach the electronic ground state S_0 through IC and VR or fluorescence or through ISC to a vibrationally excited triplet state T_1 which cools[8] and returns to S_0 by phosphorescence. Nonradiative deactivation from T_1 to S_0 can also occur through intersystem crossing and subsequent vibrational relaxation.

When the rate of intersystem crossing is much larger then fluorescence or vibrational relaxation, higher triplet states can readily be formed. After the formation of say T_2 through ISC or light absorption from T_1, deactivation in the triplet manifold occurs through internal conversion and followed by vibrational relaxation to T_1. Finally, ISC from T_1 to S_1 followed by radiative decay in the form of fluorescence is also possible. This type of fluorescence is termed delayed-fluorescence and could be mistaken as phosphorescence because the transition rates of both are similar.

3.1 Nonradiative Deactivation

The mechanism of nonradiative deactivation for a system is dependent on its physical state and therefore the following sections will go into the details of nonradiative transitions for gas and liquid phase systems.

3.1.1 Internal Conversion

From figure 3.2 it is clear that internal conversion relates to transitions $S_{n'}^{\nu'} \rightarrow S_n^{\nu}$ or $T_{n'}^{\nu'} \rightarrow T_n^{\nu}$ between two isoenergetic vibrational levels ν and ν' of different electronic levels n and n' with the same multiplicities and generally vastly different energies at equilibrium. It is however common to include vibrational relaxation in the description of internal conversion, leading to the nonradiative transitions $S_{n'} \rightarrow S_n$ and $T_{n'} \rightarrow T_n$.

[8] Here cools refers to the vibrational relaxation process.

Internal conversion from a higher excited energy levels to the first excited energy level are generally very rapid (sub picoseconds) which suggests that these higher excited states are very short-lived [6, 42, 46]. This equates to the quantum yields of emission from these higher levels being very small. In the case of fluorophores it is common that luminescence is solely observed from the first excited state. This observation is termed *Kasha's Rule*, which is obeyed in a majority of fluorophores. For example, in a recent study of the dynamics of o-xylene (see figure 3.3) through femtosecond photoelectron imaging coupled with time-resolved mass spectroscopy [47]. Liu et al showed that ultrafast internal conversion from the second singlet S_2 state to the vibrationally excited first singlet S_1 state, occurs on in about 60 fs. Here the vibrationally hot S_1 state decays to the ground singlet state S_0 state in 9.85 ps. What was also noted is that the lifetime of the lowest vibronic S_1 state is significantly longer with an estimated time of 12.7 ns. They concluded that the vast differences of lifetime of different vibrational S_1 states are largely due to their different nonradiative deactivation paths.

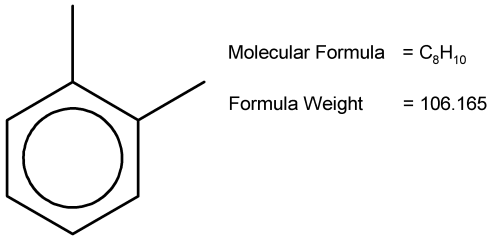

Figure 3.3: Chemical structure of o-xylene (dimethyl-1,2-benzene).

Kasha's Rule also supports the fact that the nonradiative transition $S_n \rightarrow S_1$ is generally much faster than $S_1 \rightarrow S_0$, for larger of aromatics compounds [45]. These compounds are known to fluoresce and that nonradiative deactivation of the first electronic excited state only partially occurs. This means that rapid IC from higher excited states ends up populating the S_1 state where fluorescence becomes the preferential deactivation path.

3.1.2 Intersystem Crossing

Intersystem crossing, as seen in figure 3.2 involves the transition ($S_{n'}^{\nu'} \rightarrow T_n^{\nu}$ or $T_{n'}^{\nu'} \rightarrow S_n^{\nu}$) between isoenergetic vibrational levels of electronic levels with different multiplicities. This is only possible through spin inversion (also termed spin flipping) which is a consequence of spin-orbit coupling. In a number of molecular systems, nonradiative deactivation through ISC of the first excited singlet (S_1) and triplet (T_1) states are particularly important [48].

ISC of the first singlet state S_1 to the first triplet state T_1 takes place through spin-orbit coupling of S_1 to a vibrationally excited T_1 state or a higher triplet state (say T_n). The rate of ISC is

generally slower compared to that of IC, because it is forbidden by the rules of conservation of angular momentum. However according to the *El Sayed's Rule*, the rate of ISC becomes larger (more probable) if these type of transitions include the change in molecular orbital. The selection rules for allowed ISC transitions can thus be summarized,

$$^1(\mathrm{n},\pi^*) \leftrightarrow {}^3(\pi,\pi^*) \qquad {}^3(\mathrm{n},\pi^*) \leftrightarrow {}^1(\pi,\pi^*)\,. \tag{3.1}$$

The *El Sayed's Rule* also imply that the forbidden ISC transitions will be those where no molecular orbital change occurs which is summarized as,

$$^1(\mathrm{n},\pi^*) \leftrightarrow {}^3(\mathrm{n},\pi^*) \qquad {}^1(\pi,\pi^*) \leftrightarrow {}^3(\pi,\pi^*)\,. \tag{3.2}$$

An interesting femtosecond time-resolved photoelectron spectroscopy experiment by Minns et al. on the nonradiative deactivation of benzene, showed that both internal conversion and intersystem crossing competes for effective deactivation [49]. This is attributed to the similarity in the timescales of both processes. In addition, the S_1 and T_2 states for benzene across a wide range of geometries are near degenerate. This in essence allows for ISC to become more efficient even though spin-orbit coupling is weak[9].

3.2 Beyond The Born-Oppenheimer Approximation

In this section the quantum mechanical theory which supports nonradiative deactivation of an excited molecular system which goes beyond the Born-Oppenheimer (BO) approximation as described by Matsika et al will be discussed [50]. Within this context, the formation of conical intersections (CIs) becomes crucial in understanding phenomena such as vision and photostability of dioxyribose nucleic acid (DNA) [51, 52]. Conical intersections can be seen as actual degeneracies between energy levels which facilitates non-adiabatic events. In quantum mechanical terms this implies the breakdown of the BO approximation, allowing for coupling between electronic and nuclear degrees of freedom.

3.2.1 Nonadiabatic Events

For a given chemical process within the BO approximation, nuclear motion occurs due to a force associated with the potential energy surface (PES). To understand the origin of the PES, the electronic part of the Hamiltonian equation for a molecule is solved first, resulting in a set of eigenvalues at a given nuclear geometry. The energy eigenvalues as a function of the

[9] Spin-orbit coupling becomes more prominent for heavy atoms.

nuclear geometry creates the adiabatic PES. In the BO approximation the adiabatic PES can be used to discuss a chemical reaction such as dissociation, which can be interpreted as a nuclear motion on the surface towards increasing bond length. It is important to note however that a non-trivial number of PESs exists for a molecule, because of its dependence on the nuclear geometry. This allows for nonadiabatic events to occur when two or more PESs comes within touching distance. Here coupling between these surfaces becomes important. Quantum mechanically, a wave function moves on a PES and if two PESs are close to each other, the wave function may change surfaces. Suggesting that nuclear motion occurs while the electronic configuration changes, resulting in a coupling which is then termed to be nonadiabatic. To understand these events and the properties of molecular systems, it is necessary to first solve the time-independent Schrödinger equation (TISE)

$$\hat{H}\Psi\left(\mathbf{r},\mathbf{R}\right)=E\Psi\left(\mathbf{r},\mathbf{R}\right), \tag{3.3}$$

where $\mathbf{r}$ denotes the electronic and $\mathbf{R}$ the nuclear coordinates. The non-relativistic Hamiltonian in eq.3.3 is given by

$$\hat{H}\left(\mathbf{r},\mathbf{R}\right)=\hat{T}^{n}\left(\mathbf{R}\right)+\hat{H}^{e}\left(\mathbf{r};\mathbf{R}\right), \tag{3.4}$$

where $\hat{T}^{n}$ is the nuclear kinetic energy operator and $\hat{H}^{e}\left(\mathbf{r};\mathbf{R}\right)$ is the electronic Hamiltonian. The electronic Hamiltonian in turn, consist of the electronic kinetic energy and the various Coulomb interactions between the particles. The electronic wave functions which are the eigenfunctions of $\hat{H}^{e}\left(\mathbf{r},\mathbf{R}\right)$ form a complete basis set and can be obtained by solving the following electronic equation

$$\hat{H}^{e}\Psi_{I}^{e}\left(\mathbf{r};\mathbf{R}\right)=E_{I}^{e}\Psi_{I}^{e}\left(\mathbf{r};\mathbf{R}\right). \tag{3.5}$$

The electronic eigenfunctions $\Psi_{I}^{e}\left(\mathbf{r};\mathbf{R}\right)$ can be used in a so-called BO expansion to determine the total wave function

$$\Psi\left(\mathbf{r},\mathbf{R}\right)=\sum_{I}\Psi_{I}^{e}\left(\mathbf{r};\mathbf{R}\right)\chi_{I}\left(\mathbf{R}\right), \tag{3.6}$$

where $\chi_{I}\left(\mathbf{R}\right)$ are the expansion coefficients which become the nuclear wave function $\chi\left(\mathbf{R}\right)$ when the summation in total wave function expression is not truncated. At this point inserting the total wave function into the TISE (eq.3.3) becomes

$$\left[\hat{T}^{n}+E_{I}^{e}\left(\mathbf{R}\right)\right]\chi_{I}-\sum_{J}\hat{\Lambda}_{IJ}\left(\mathbf{R}\right)\chi_{J}\left(\mathbf{R}\right)=E\chi_{I}\left(\mathbf{R}\right), \tag{3.7}$$

where $\hat{\Lambda}_{IJ}$ depends on K_{IJ} and f_{IJ} which couples the electronic states I and J. These coupling terms form when the nuclear energy operator acts on the electronic wave function in the following way

$$f_{IJ}^{\alpha}(\mathbf{R}) = \left\langle \Psi_I^e(\mathbf{r};\mathbf{R}) \mid \nabla_\alpha \Psi_J^e(\mathbf{r};\mathbf{R}) \right\rangle \tag{3.8}$$

and

$$K_{IJ}(\mathbf{R}) = \sum_{\alpha} \left\langle \Psi_I^e(\mathbf{r};\mathbf{R}) \mid \nabla_\alpha^2 \Psi_J^e(\mathbf{r};\mathbf{R}) \right\rangle. \tag{3.9}$$

The bra-ket notation above signifies the integration over all electronic coordinates $\mathbf{r}$ with ∇_α being the gradient over the nuclear coordinate $\mathbf{R}_\alpha$. When only considering the diagonal form of K_{IJ} in eq.3.9, it is clear that this term relates to the nonadiabatic corrections of a PES commonly referred to as BO corrections. The f_{IJ} term in eq.3.8 is the derivative or nonadiabatic coupling (NAC) between states I and J. This nonadiabatic coupling term depends on the change in the electronic wave function with the nuclear coordinates and is also inversely proportional to the energy gap between states I and J,

$$f_{IJ}(\mathbf{R}) = \frac{\left\langle \Psi_I^e \mid \nabla \hat{H}^e \mid \Psi_J^e \right\rangle}{E_J^e - E_I^e}. \tag{3.10}$$

In the case of the BO approximation, where coupling between the nuclear and the electronic degrees of freedom is ignored. The total wave function reduce to the product of the electronic wave function $\Psi_I^e(\mathbf{r};\mathbf{R})$ and the nuclear wave function $\chi_I(\mathbf{R})$,

$$\Psi_I(\mathbf{r},\mathbf{R}) = \Psi_I^e(\mathbf{r};\mathbf{R})\,\chi_I(\mathbf{R}). \tag{3.11}$$

This allows for the nuclear and electronic parts of the TISE to be separated and solved through the insertion of the electronic eigenfunctions. Here it is assumed that the electronic states are far apart resulting in a small coupling. However, if the difference in electronic eigenvalues become smaller, a minute change in the nuclear position may lead to a huge change in the electronic wave functions. In this case the BO approximation breaks down and eq.3.7 is preferred. The expanded form of the total wave function in eq.3.11 ensures that the coupling matrix elements $\left\langle \Psi_I^e \mid \hat{H}^e \mid \Psi_J^e \right\rangle$ are zero and that coupling is only present in the nuclear kinetic energy terms. This representation is termed adiabatic and makes solving the TISE difficult when singularities are present in the derivative coupling vector $f_{IJ}(\mathbf{R})$. This can be easily remedied through changing the representation to a diabatic one [53, 54]. In this representation the derivative coupling terms vanishes when the TISE is diagonalized.

3.2.2 Conical Intersections

Nonradiative transitions between two (or more) electronic states becomes more efficient when these states are near degenerate. This is evident from the specific form of the derivative coupling vector in eq.3.10. If however these states are degenerate, f_{IJ} goes to infinity and a conical intersection is formed which offers the most efficient nonradiative pathway.
In order to determine the requirements for the existence of a conical intersection, consider a diabatic two-state Hamiltonian

$$\mathbf{H}^e = \begin{bmatrix} H_{11}(\mathbf{R}) & H_{12}(\mathbf{R}) \\ H_{21}(\mathbf{R}) & H_{22}(\mathbf{R}) \end{bmatrix}, \tag{3.12}$$

where $H_{ij} = \langle \phi_i \mid \hat{H}^e \mid \phi_j \rangle$ and ϕ_i the diabatic wave functions. The eigenvalues of eq.3.12 is easily obtained through an orthogonal transformation $\mathbf{S}^\dagger \mathbf{H}^e \mathbf{S}$ with

$$\mathbf{S} = \begin{bmatrix} \cos(\alpha(\mathbf{R})/2) & \sin(\alpha(\mathbf{R})/2) \\ -\sin(\alpha(\mathbf{R})/2) & \cos(\alpha(\mathbf{R})/2) \end{bmatrix}. \tag{3.13}$$

This transformation rotates the wave functions as well as the derivative coupling. In this configurational space the eigenvalues become

$$E_{1,2} = \bar{H} \pm \sqrt{\triangle H^2 + H_{12}^2}, \tag{3.14}$$

where $\bar{H} = (H_{11} + H_{22})/2$ and $\triangle H = (H_{11} - H_{22})/2$. In eq.3.13 the rotational angle α describes the transformation from diabatic to adiabatic states and is determined as

$$\sin\alpha = \frac{H_{12}}{\sqrt{\triangle H^2 + H_{12}^2}}, \tag{3.15}$$

$$\cos\alpha = \frac{\triangle H}{\sqrt{\triangle H^2 + H_{12}^2}}. \tag{3.16}$$

In order for the eigenvalues to be degenerate, the following conditions need to be fulfilled,

$$H_{11}(\mathbf{R}) - H_{22}(\mathbf{R}) = 0, \tag{3.17}$$

$$H_{12}(\mathbf{R}) = 0. \tag{3.18}$$

In the case of a molecule with N internal degrees of freedom, the conditions in eqs.3.17 & 3.18

are fulfilled in a $N-2$ subspace and is often described as the non-crossing rule. This becomes evident when considering the diatomic sodium chloride (NaCl) molecule which has only one degree of freedom. This system can be described by two separate wave functions, one ionic (Na^+Cl^-) and the other covalent (Na-Cl). Figure 3.4(a) shows the corresponding potential energy curves for the ionic and covalent wave functions as a function of the internuclear separation. It is clear that at a specific internuclear separation, the two wave function cross. This however is impossible because the two electronic states has the same symmetry. To remedy this, a different wave function is chosen to describe the system. To this end a mixture of the ionic and covalent wave functions through self-consistent field methods in combination with the variational principle offers the best results. The schematic representation for the potential energy curves of the new optimized wave functions are shown in figure 3.4(b). In this representation the crossing of the two potential energy curves are avoided and suggest that the calculated potential energies from the original wave functions repel each other.

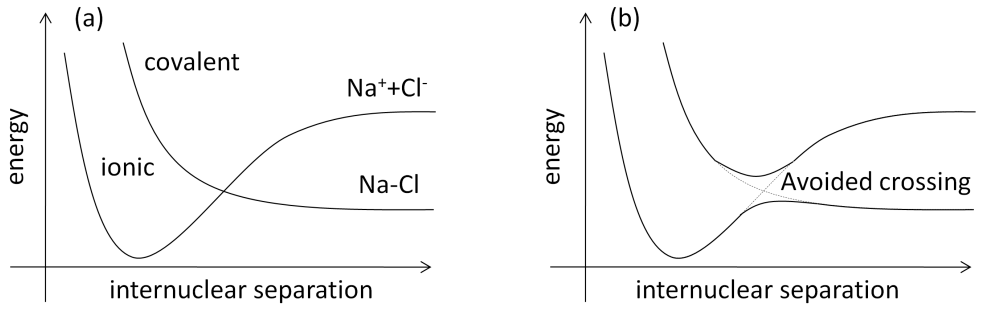

Figure 3.4: Schematic representation of the crossing (a) and avoided crossing (b) found in the potential energy curves for the prototypical diatomic molecule sodium chloride (NaCl).

For polyatomic molecules which generally have a large number of nuclear degrees of freedom, degeneracies in their electronic states becomes possible. The non-crossing rule state that the CIs are therefore not mere isolated points in space, but rather an infinite number of points, connected together to form a subspace called the seam which has the dimensions of $N-2$. The space orthogonal to the seam space is known as the branching or $g-h$ space in which the degeneracies are naturally lifted linearly in the nuclear coordinates. It is in this branching space where the phrase conical intersection arose from, because the PESs in this space resembles a double cone in the region surrounding the degeneracy.

3.2.3 Molecular Dynamics

In order to describe nonadiabatic molecular dynamics of both the electronic and nuclear degrees of freedom however it is crucial that the time dependence is also considered. Therefore one is faced with the additional problem of solving the nonrelativistic time-dependent Schrödinger equation (TDSE):

$$i\hbar\frac{\partial}{\partial t}\Psi\left(\mathbf{r},\mathbf{R},t\right)=\hat{H}\Psi\left(\mathbf{r},\mathbf{R},t\right) \tag{3.19}$$

where $\mathbf{r}$ and $\mathbf{R}$ represent the electronic and nuclear coordinates. As in the previous section the full wave function $\Psi\left(\mathbf{r},\mathbf{R},t\right)$ is expanded into the adiabatic eigenstates of the electronic Hamiltonian, now with explicit time dependence included in the expansion coefficients which are interpreted as the nuclear wave functions. This provides the wave packet description required to discuss various chemical reactions. In solving the TDSE for a system containing a large number of atoms, numerical methods have become the norm. The self-consistent field (SCF) method is an *ab initio* method in which the molecular wavefunction is approximated as the product of single electron wavefunctions. This is often referred to as the Hartree-Fock (HF) method which together with the SCF method in an iterative way solves the Schrödinger equation for a minimized energy through approximating the Hamiltonian. In this way the energy values calculated are generally higher than the actual values. This is a consequence of the variational principle and the fact that here coulombic repulsion between electrons is treated in an average way. Another method termed configuration interaction gives a more accurate picture and lower energy values by considering the instantaneous interactions between electrons. Here the calculated correlation energy (due to the correlated electron picture) is essentially the difference between exact energy and the calculated HF energy.

The most popular method used nowadays is time-dependent density functional theory (TD-DFT) where the energy is obtained from the density of the electrons in the system [55]. TD-DFT is not an *ab initio* method as it does not explicitly solve Schrödinger equation it nevertheless allows for the treatment of nonadiabatic events. In a recent publication by Hirai et al, TD-DFT together with an adiabatic local density approximation (ALDA) was used to study the photo-induced isomerization reaction of formaldimine (CH_2=NH) [56]. Furthermore nonadiabatic dynamics and dissipation effects were studied through Langevin dynamics of the five atom system. This molecule is similar to the test sample DPM, of this dissertation. In that it also undergoes isomerization about a C=N double bond when excited with the appropriate amount of photon energy. Unfortunately, monitoring the photo-induced isomerization of formaldimine through UTA spectroscopy is extremely challenging due to the high photon energy (5.2 eV) required to excite the molecule. An added difficulty would also be to distinguish between the

spectral features of the reactant versus the product because the two isomeric forms are mirror images of one another. Meaning that they will have identical spectral signatures. Formaldimine is the smallest molecule in the class of imines (DPM being another) and has been used by various groups as a prototype for photo-induced isomerization studied through quantum mechanical simulations in order to understand the wave packet dynamics at a conical intersection. Hirai et al through these type of simulations followed the motion of the hydrogen atom which is covalently bonded to the nitrogen atom as the molecule undergoes isomerization. Two dynamical variables were considered as specific pathways for isomerization. One being the twist angle ϕ and the other the in-plane inversion angle θ as described in figure 3.5.

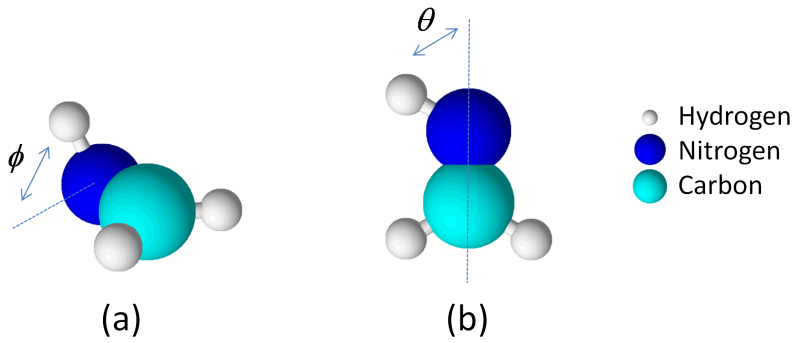

Figure 3.5: The twisting (a) and inversion (b) paths for isomerization of formaldimine.

For these calculations all the other bond lengths and angles were kept constant to the values determined at PES minimum. In figure 3.6 the first three calculated adiabatic potential energy surfaces of formaldimine are shown. From this plot of the PESs a number of interesting points can be highlighted:

1. an avoided crossing between S_0 and S_1 at $(\phi = 90°, \theta = 90°)$,
2. the energy minimum of S_1 at $(\phi = 90°, \theta = 70°)$.

It is also evident from figure 3.6 that the second excited state (S_2) is somewhat separated from the first excited state (S_1) and ground state (S_0), which underpins the notion that the molecular dynamics after excitation to S_1 will not involve S_2. In order to understand which coordinate (ϕ or θ) is responsible for isomerization, the nonadiabatic coupling (NAC) terms becomes important.

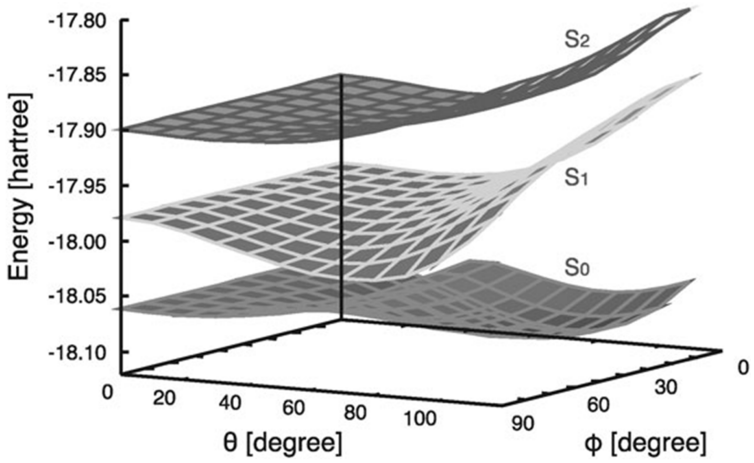

Figure 3.6: The adiabatic potential energy surface S_0, S_1 and S_2 of formaldimine. Taken from reference [56].

From figure 3.7 it can be seen that the NAC increases towards the avoided crossing region in the ϕ direction which is larger than the NAC in the θ direction. Suggesting that nonadiabatic transition between S_1 and S_0 occurs for the most part through the twisting motion.

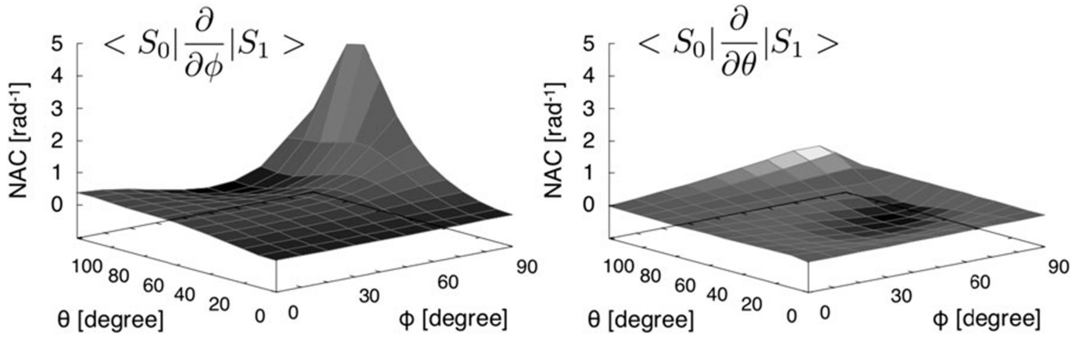

Figure 3.7: The first order nonadiabatic coupling (NAC) terms for both the twisting ϕ and inversion θ coordinates. Taken from reference [56].

Figure 3.8 shows the temporal evolution of the wave packets on both the S_1 and S_0 potential energy surfaces. Here the initial Gaussian type (half-width 10°) wave packet was set at $\phi = 30°$ and fixed inversion angle $(\theta = 80°)$ which corresponds to the slope of S_1. The wave packet then oscillated around the energy minimum of S_1 passing the avoided crossing region on each round-trip. It is at this crossing point where nonadiabatic transition occurred which diminishes the wave packet amplitude on S_1. The nonadiabatic transition results in the wave packet being allowed to propagate to the S_0 surface.

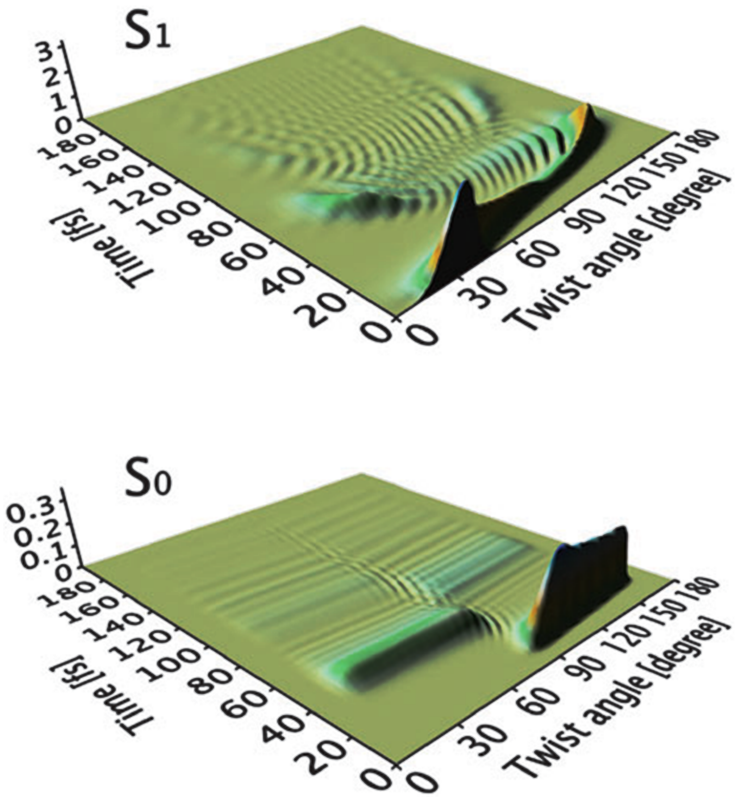

Figure 3.8: Temporal evolution of wave packets on the potential energy surfaces S_1 (upper) and S_0(lower). Taken from reference [56].

In summary Hirai et al found that for effective isomerization in formaldimine both inversion and twisting occurs. More particularly, after photo-excitation of the reactant, the inversion motion is initiated followed by the twisting motion. During this twisting motion the wave packet is free to propagate on the first excited state to the energy minimum located at $\phi = 90^\circ$ (orthogonal geometry), here nonadiabatic transition allows for propagation to the product or back to the reactant. It should be noted that the simulation of frictional forces through Langevin dynamics effected the yields of the both the product and reactant after initial excitation. This showed that the interaction with the environment should be considered when discussing isomerization of this type.

4. Photochromism of Dithizonatophenylmercury(II)

The term photochromism refers to the photo-induced transformation of a molecule between two structural forms which have distinctly different absorption spectra. In general this transformation may be reversible, but not always by means of photo-activation [46, 57, 58]. As in the case of dithizonatophenylmercury(II) the reverse reaction occurs thermally in the absence of light (see figure 4.1). In essence the structural change could be by means of a variety of reactions such as excited state proton transfer resulting in a bond breakage and more commonly through isomerization [13, 39]. Inevitably the two forms have different physical properties. Meaning that measurable quantities like the refractive index, polarizability and electrical conductivity are greatly influenced by the structural change.

Dithizonatophenylmercury(II) is a metal complex which in solution displays a strong photochromic effect when illuminated with blue-green light (400 - 500 nm). As seen in figure 4.1 the colour change when DPM is dissolved in dichloromethane is from orange (reactant) to blue (product), which indicates the disappearance of the reactant absorption band in the blue and the appearance of the product absorption band in the orange spectral range.

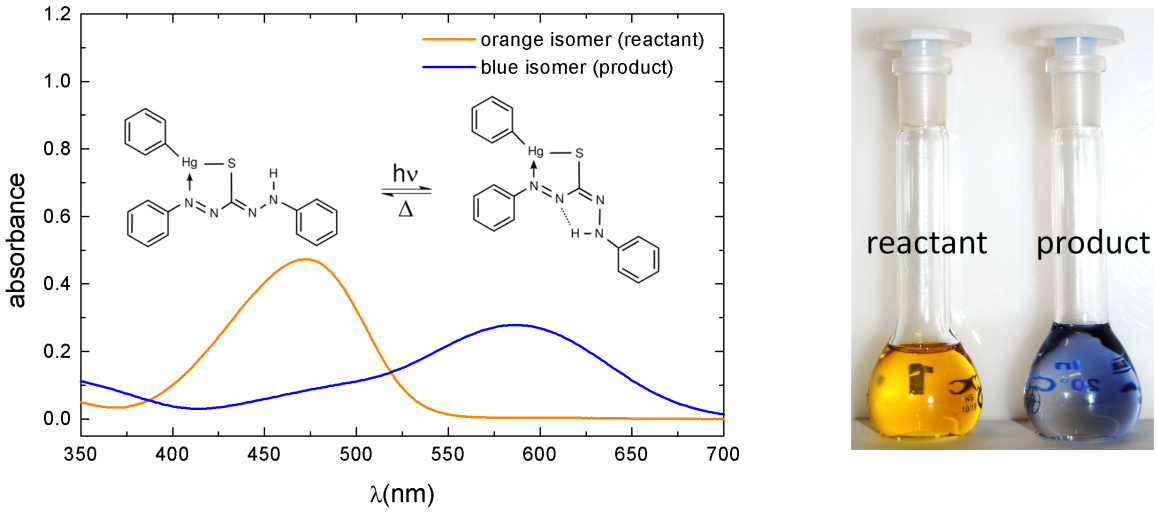

Figure 4.1: Left: Absorption spectra of DPM in dichloromethane (8×10^{-6} mol.dm^3), with λ_{max}(orange) = 480 nm, and λ_{max}(blue) = 583 nm. Molar absorptivity (470 nm) = 57300 dm^3.mol^{-1}.cm^{-1}. Insert: Isomerization of DPM. Right: Picture of DPM dissolved in dichloromethane before (reactant) and after (product) illumination of blue light.

For DPM, photochromism is merely a side-effect of the underlining photo-induced isomerization which was proposed by various researches [9, 10]. The most notable of which was by Meriwether in 1965, who synthesized 24 different metal dithizonate complexes and characterized the compounds in terms of structure, UV/Vis and IR absorption as well as the kinetics of the back reaction [10, 59]. From these initial investigations it was however never possible to determine with absolute certainty the chemical structure of the blue isomer. This is due to the fact that the photo-product does not crystallize and therefore a technique like X-ray crystallography is not possible. Recently however, von Eschwege et al. proposed that the photo-product shown in figure 4.1 & 4.2 (a) is indeed the preferred structural conformation.

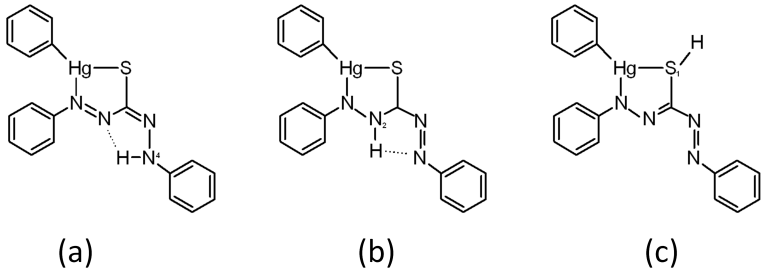

Figure 4.2: Photo-product geometries of dithizonatophenylmercury(II): (a) N4H, (b) N2H and (c) S1H.

This was done theoretically by means of density functional theory (DFT) [10]. They calculated that the N4H is favoured energetically by more than 35 kJ.mol^{-1} from the other two hypothetical photo-products N1H and S1H.

In this chapter the changes which occurs in the steady state absorption spectra of DPM when altered electronically through the addition of various substituents on the phenyl group attached to the dithizonate backbone will be reported on (see figure 4.3).

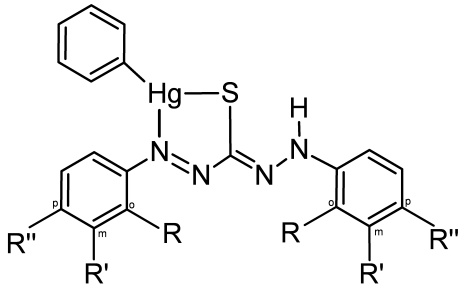

Figure 4.3: Chemical structure of DPM indicating the substituents as R, R′ and R″ at the ortho (o), meta (m) and para (p) positions of the phenyl groups in the dithizonate backbone.

The electronically altered samples are:

- meta-fluorodithizonatophenylmercury(II) (m-F-DPM),
- ortho-fluorodithizonatophenylmercury(II) (o-F-DPM),
- para-fluorodithizonatophenylmercury(II) (p-F-DPM),
- 3,4-dimethyldithizonatophenylmercury(II) (m,p-diMe-DPM),
- meta-methyldithizonatophenylmercury(II) (m-Me-DPM),
- ortho-methyldithizonatophenylmercury(II) (o-Me-DPM),
- para-methyldithizonatophenylmercury(II) (p-Me-DPM),
- meta-methoxydithizonatophenylmercury(II) (m-OMe-DPM),
- ortho-methoxydithizonatophenylmercury(II) (o-OMe-DPM),
- ortho-sulfur-methyldithizonatophenylmercury(II) (m-OMe-DPM),
- para-sulfur-methyldithizonatophenylmercury(II) (p-OMe-DPM) and
- para-chlorodithizonatophenylmercury(II) (p-Cl-DPM).

In addition the details about the transient behaviour of the photo-product and preliminary DFT calculations will also be studied.

4.1 Steady state study of DPM and its derivatives

Steady state absorption spectroscopy in the UV/Vis spectral region is generally seen as the point of departure for ultrafast transient absorption spectroscopy. As it is the simplest optical method to gain information about the electronic (and vibronic) excitation signatures of a molecule.
The absorption spectra for DPM and its derivatives are recorded with a standard UV/Vis spectrophotometer with all of the samples dissolved in dichloromethane[10]. It is observed that all samples undergo photochromism when illuminated with an UV lamp[11]. Due to the similarity of the absorption spectra of the derivatives to that of DPM (see figure 4.1). Only the spectra of m,p-diMe-DPM is shown (figure 4.4) with the more pertinent results summarized in table 4.1. From figure 4.4 it is clear that the absorption maxima's for both the reactant and product form of m,p-diMe-DPM are red-shifted by about 16 nm. This severe shift translates to a smaller energy

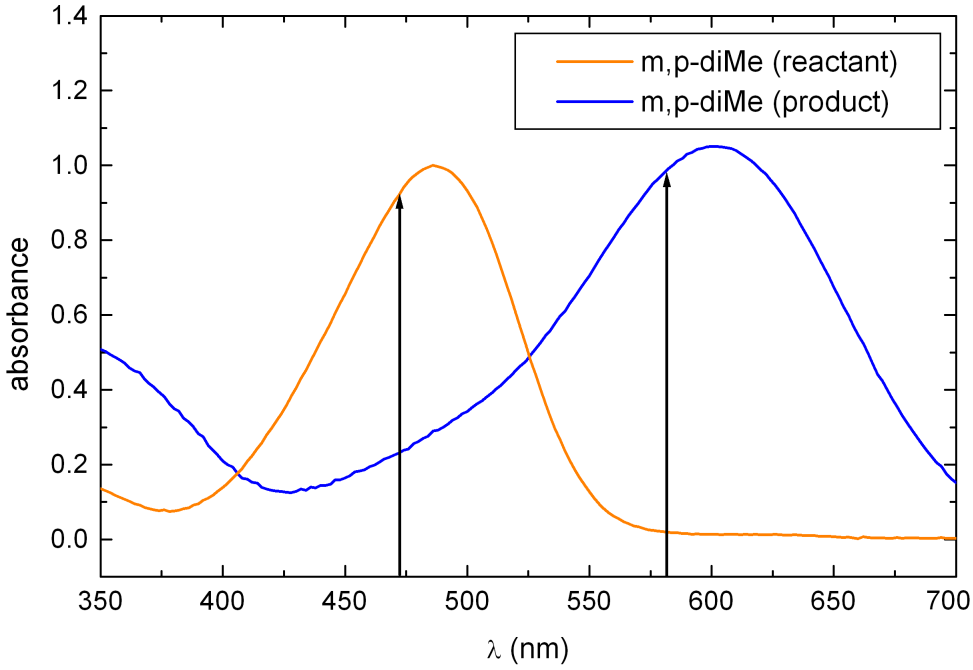

Figure 4.4: Absorption spectra of m,p-dimethyldithizonatophenylmercury(II) dissolved in dichloromethane. The arrows indicate the absorption maxima's for the unaltered DPM in both its orange (left arrow) and blue (right arrow) forms.

gap between electronic ground and excited state in both isomers. Looking at table 4.1, this scenario red-shift is common for almost all derivatives, however the orange isomers of o-F-DPM and o-Me-DPM shows a blue-shift. Whilst their blue isomeric forms display the typical red-shifted behaviour. The only test sample in the series that exhibit blue-shift in both the reactant and product form is p-F-DPM.

What should be made special mention of, is that substituents may also alter the electronic nature of the delocalized π orbitals on the dithizonate backbone. Some of the substituents are electron donating while the others have a large electron affinity. The specific electronic behaviour of these substituents when attached to DPM were determined through measuring the first oxidation potential[12] of each sample. The electron donating ability (as inferred from the first oxidation potential data) of the samples increases from left to right in the following relation,

$$\text{o-F} < \text{m-F} < \text{p-F} < \text{o-Me} < \text{R-H} < \text{p-Me} < \text{m-OMe} < \text{m-Me} < \text{o-OMe}. \tag{4.1}$$

[10]The concentrations are kept in the micro molar (μM) range.

[11]This lamp emits incoherent UV light from 340 - 500 nm.

[12]These measurements were conducted in the Chemistry Department at the University of the Free State, under Dr K. G. von Eschwege.

Table 4.1: Steady state absorption results of DPM and its derivatives when dissolved in dichloromethane.*Me: methyl (CH_3).

Substituent-DPM	Orange isomer λ_{max}(nm)	Blue isomer λ_{max}(nm)
R-H	472	588
m-F	472	589
m-Me*	476	610
m-OMe*	483	600
m,p-diMe*	486	602
o-F	470	600
o-Me*	462	600
o-OMe*	498	616
o-SMe*	490	596
p-Cl	480	600
p-F	474	586
p-Me*	482	594
p-SMe*	508	590

Whilst the sample on the left of the relation 4.1 has the greatest electron affinity and the one on the right the smallest. This electron donating and accepting nature of a given substituent is postulated to either elongate or shorten the π electron delocalization on the dithizonate backbone. Which directly translates to a blue-shift in spectral absorption maximum for samples with electron accepting substituents and a red-shift for those with electron donating substituents. In general however the specific position and shift (in reference to the position of DPM) of the absorption peak depends in a complicated manner on the combination of solvation and the electronic effect on the delocalized π orbitals which ultimately also influences the electron density around the double bond where isomerization occurs.

4.2 Transient behaviour of the Photo-product

In this section the back reaction of DPM will be investigated. Here DPM and its physical environment will be carefully altered as to see the effect it has on the rate of the back reaction. This is done through monitoring the absorbance of the photo-product at set time intervals after excitation with an UV lamp. Figure 4.5 shows the schematic of the experimental setup used to measure the transient absorption change of the photo-product. In this setup, the Clark-MXR (CPA 2101) fs laser light is used to generate a whitelight continuum in calcium fluoride (CaF_2) which is spectrally filtered to the absorption maximum of the photo-product with a narrow bandwidth (dielectric) filter. This filtered light is then allowed to pass through the sample and collected in a spectrometer (Andor Spectrometer with Hamamatsu PDA sensors capable of detecting every pulse). Using this setup allows for a temporal resolution equal to the period of the

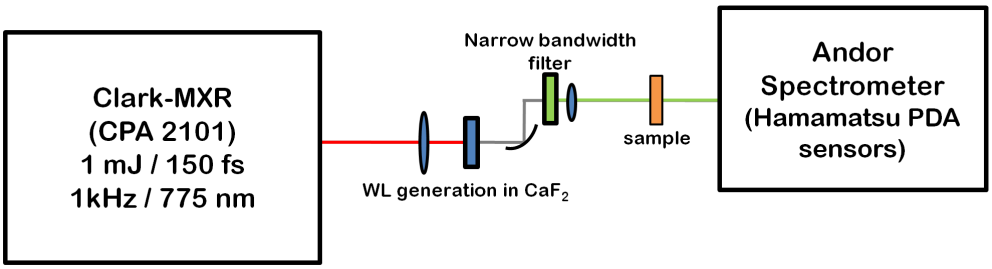

Figure 4.5: Schematic of the experimental setup used to measure the transient absorption change of the photo-product.

laser (1 ms). It should also be mentioned that the sample temperature is preferentially altered using a chiller. Whilst the temperature of the sample is measured within a tenth of a degree using a K-type thermocouple submerged in the sample.

In this measurement it is actually the transmission change that is detected but assuming no scattering the absorption can easily be calculated[13]. Due to instability of the photo-product, it will readily transform back to the reactant form. Meaning that the absorbance of the product will decay in time. This can be written in the form of a chemical reaction assuming first order kinetics as,

$$[Product] \xrightarrow{k} [Reactant] \tag{4.2}$$

where k is the decay rate and the square brackets indicates the concentration. Therefore the rate at which the photo-product decays is proportional to its concentration,

$$\frac{d\,[Product]}{dt} = -k\,[Product]\,. \tag{4.3}$$

The solution of eq.4.3 is a product concentration which decays exponentially at a rate k,

$$[Product]\,(t) = [Product]_{init} \exp\,(-kt) + A, \tag{4.4}$$

where $[Product]_{init}$ is the initial concentration of the product shortly after photo-excitation and A the time independent factor which arise from solving eq.4.3. The decay time (τ) is then defined as the time it takes for the product concentration to reach a value equal to $(1/e)$ of its initial value (for $A = 0$). For eq.4.6 this is when $\tau = 1/k$.

[13]When light of a low intensity passes through a medium, it can either be absorbed (A), transmitted (T), scattered (S) or reflected (R). Therefore starting with 100 % of light it will separated into these three contributions as follow 100% = A+T+S+R. The reflected light from the two surfaces of the cuvet remains small and constant during the measurement because the refractive index does not experience a measurable change as a result of the photo-reaction.

4.2.1 The effect of the solvent

In order to study the effect the solvent has on the lifetime of the photo-product of DPM. DPM was dissolved in a number of solvents such as methanol, dichloromethane and toluene. The first two being polar and the latter a non-polar solvent. In addition methanol is a protic (dissociable H^+) and dichloromethane an aprotic polar solvent. The two polar solvents have similar dipole moments (methanol: 1.70 ± 0.01 D[14] and dichloromethane: 1.60 ± 0.02 D) whilst toluene has a smaller dipole moment of 0.38 ± 0.01 D [60]. The transient behaviour of the photo-product of DPM dissolved in dichloromethane and toluene is shown in figure 4.6: the lifetime of the photo-product in dichloromethane (794.8 ± 4.8 s) is significantly longer than that of toluene (47.19 ± 0.14 s).

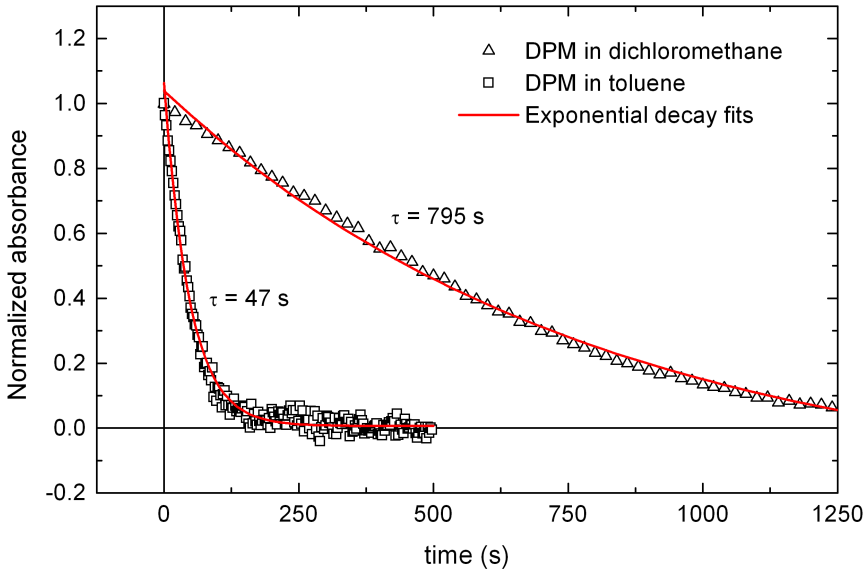

Figure 4.6: Measurement of the transient absorption signal at λ_{max} for the blue form of DPM dissolved in dichloromethane and toluene at 20.1°C.

Currently there is no specific reason why this should be the case. Even more interesting is that no product is detected for the case where DPM is dissolved in methanol. It should be stated at this point however that a short lifetime (less than 1 ms) product might be present seeing that the temporal resolution of the setup is only 1 ms. A possible reason for the different product lifetimes could be due to sterically hindered product forms.

[14] 1 Debye (D) = 3.33564×10^{-30} C·m

4.2.2 The effect of the substituent

In this section the photo-product lifetime of DPM and it's derivatives are compared. Here all the samples are dissolved in dichloromethane in an effort to limit the solvent effect as seen in the previous section. The various samples all exhibit the reversible photochromic behaviour when dissolved in DCM which indicates that this solvent does not form permanent bonds with the test samples. Table 4.2 summarizes the various lifetimes of DPM and it's electronically altered derivatives.

Table 4.2: Decay times of the photo-products for DPM and its various electronically altered derivatives, when dissolved in dichloromethane.

Substituent-DPM	Decay times (s)
R-H	795
o-Me	48.7
m-Me	66.1
p-Me	442.9
m,p-diMe	597
o-F	14.7
m-F	223.5
p-F	225.3
o-OMe	$>$1000
m-OMe	51.4
o-SMe	3713
p-SMe	143
p-Cl	527

$0.3 - 1$ % error on decay times

What is glaringly clear from the table above is that except for the ortho-methoxy (o-OMe) and ortho-sulfur methyl (o-SMe) derivatives, DPM has the largest decay time. Since a larger decay time signifies a longer photo-product lifetime this implies therefore that the products of DPM, o-OMe and o-SMe are inherently more stable. In contrast to these three, it can be seen from table 4.2 that ortho-fluoro (o-F) has the most unstable photo-product.

When considering only the methyl and fluorine substituents, an interesting trend emerges that the photo-product lifetime increases as the substituent is moved from the ortho towards the para position. Even the product lifetime for the meta, para - dimethyl (m,p - diMe) is longer lifetime than meta- and para-methyl individually. This trend is independent of the various

electron affinities (see section 4.1) of the substituents and suggests that the sterical hinder of a substituent in the ortho position plays a roll in the back reaction.

4.2.3 The effect of temperature

As previously stated, the isomerization of the back reaction in DPM occurs thermally. Therefore an increase in temperature will ultimately effect the rate at which the product returns to the reactant form. Generally higher temperatures result in faster reaction rates, because higher energy levels in the product ground state is occupied resulting in an effectively lowered energy barrier. Determining the rate of the back reaction for first order kinetics at various temperatures allows for the use of the Arrhenius equation,

$$k = A \exp\left(-\frac{E_a}{RT}\right) \tag{4.5}$$

where k is the rate of the reaction, A an exponential pre-factor, E_a the activation energy (sometimes called the potential energy barrier), R the universal gas constant and T the temperature.

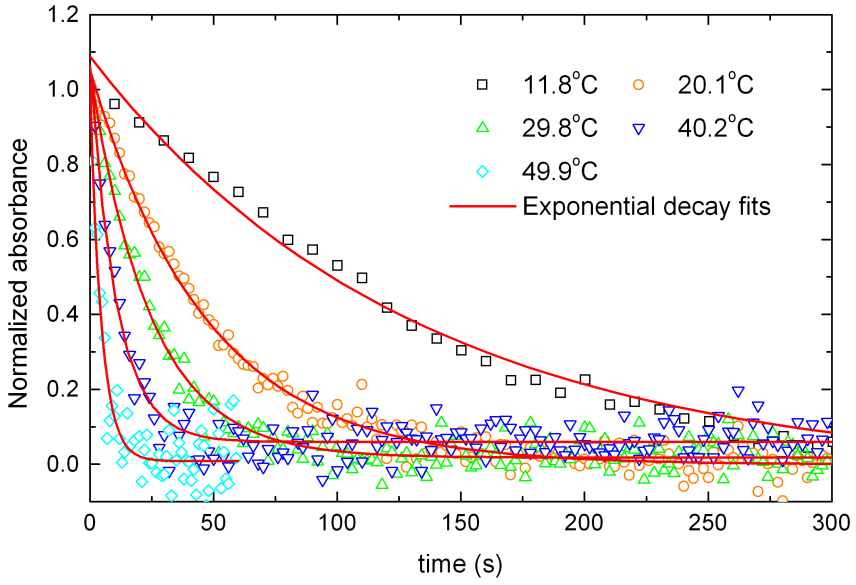

Figure 4.7: Transient absorption change of the photo-product of DPM dissolved in toluene with respect to temperature.

Thus in the case of DPM, it is simple to calculate the activation energy of the chemical reaction if the back reaction is monitored at different temperatures.

In order to study the effect temperature has on the rate of the back reaction, DPM is dissolved in non-polar solvent toluene which has a boiling point temperature of 110°C. This allowed for a large temperature range of investigation. In figure 4.7 the transient absorption change of DPM

when dissolved in toluene for five different temperatures are plotted. Also included are the exponential fits of the various measurements. Evaluating these exponential fits resulted in the values listed in table 4.3.

Table 4.3: Parameters of the temperature dependence of the rate constant from figure 4.7.

T (K)	1/RT (mol/J)	Rate constant (s^{-1})	ln(Rate constant)
323	3.72×10^{-4}	2.183×10^{-1}	-1.522
313	3.84×10^{-4}	9.302×10^{-2}	-2.375
303	3.97×10^{-4}	4.093×10^{-2}	-3.196
293	4.10×10^{-4}	2.126×10^{-2}	-3.851
285	4.22×10^{-4}	7.692×10^{-3}	-4.868

R = 8.314472 $J.mol^{-1}.K^{-1}$ (Universal gas constant)

These values consists of the rate constants corresponding to the sample temperatures as well as the inverse temperatures and the natural logarithm of the rate constants. The latter two forming the data which is fitted in figure 4.8 with the linearized form of the Arrhenius eq. 4.5,

$$\ln k = -E_a \left(\frac{1}{RT} \right) + \ln A. \tag{4.6}$$

The gradient of the straight line fit in figure 4.8 according to eq. 4.6 is thus the activation energy. The value of which is equal to 64.795 kJ/mol or 0.67 eV.

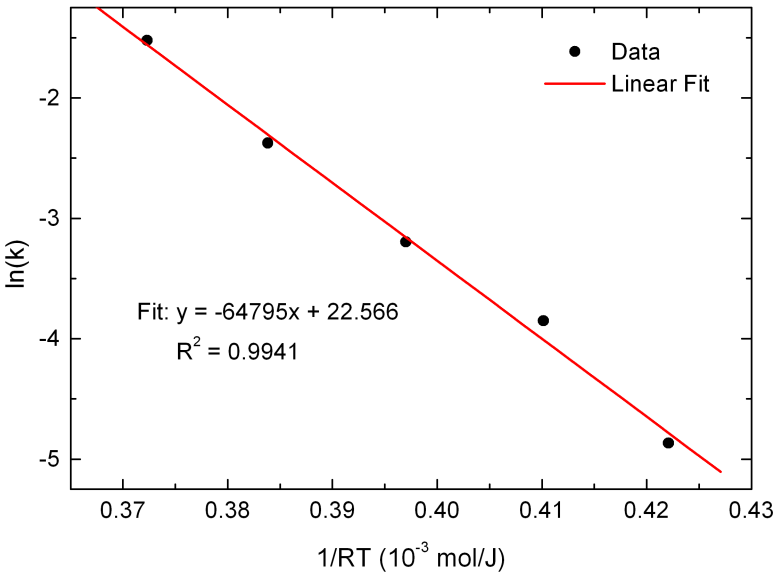

Figure 4.8: Plot of the natural logarithm of the rate versus the inverse temperature plus a linear fit.

4.3 Density functional theory calculations

The theoretical investigation of isomerization in DPM has prompted the use of density functional theory (DFT) calculations. This approach allows for a more complete description and understanding of the isomerization pathway. More specifically, DFT is used to obtain a value for the potential energy as a function of a given coordinate. In the case of isomerization from the reactant to a product, the energy is minimized as the dihedral angle S1-C1=N3-N4 (twist angle) is varied, see figure 4.9. The DFT calculations were conducted using the software package Gaussian, version 09, making use of the B3LYP (B3 Becke 3-parameter exchange and Lee-Yang-Parr correlation) functional with the CEP-31G (Stevens/Barch/Krauss) basis set [61]. Before

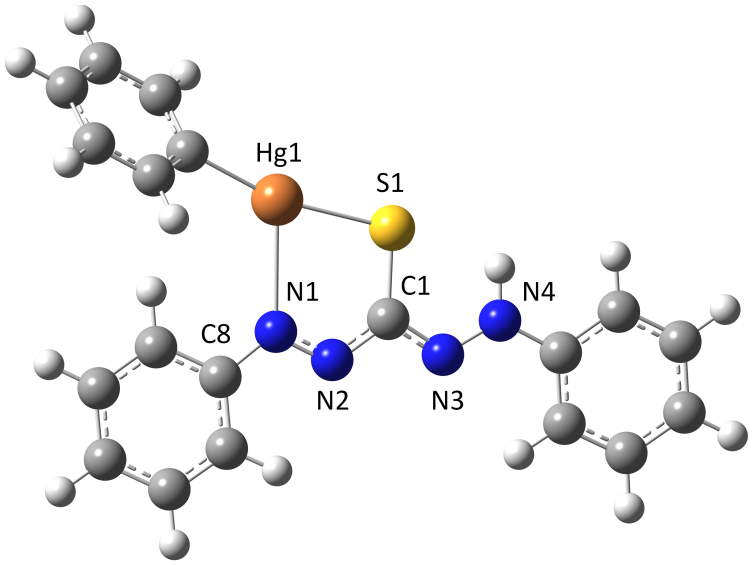

Figure 4.9: Geometrically optimized structure of the orange isomer DPM. The labeling pertains to the specific atom and the IUPAC naming scheme.

calculating the potential energy as a function of dihedral angle, it was necessary to do initial optimization of the geometry with the mentioned functional and basis set. In order to determine whether the geometrically optimized structure is at all relatable to the true molecule, the calculated singlet excitation values were compared to the experimentally obtained UV-Vis steady state spectra. Figure 4.10 graphically illustrates the comparison between the the calculated singlet excitation energy (in nanometers) of the various DPM derivatives and the measured maximum absorption wavelength in the visible spectral range. Also both the x- and y-axis have been normalized to the calculated singlet excitation (y-axis) and measured maximum absorption (x-axis) of DPM through subtraction of the calculated (y-axis) and measured (x-axis) wavelengths of DPM. In so doing DPM is set as benchmark, from which the derivatives are assessed. This permits the use of a precision line (see figure 4.10) which indicates perfect calculation and mea-

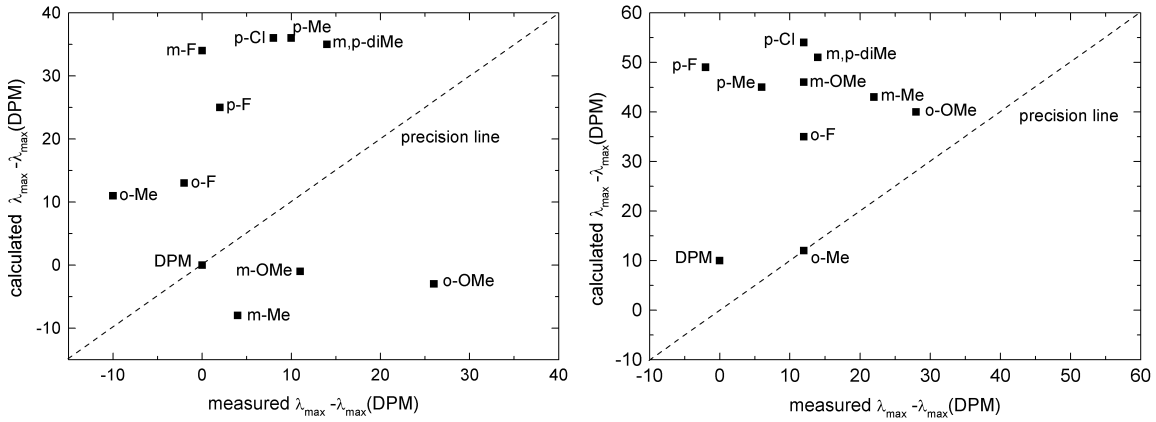

Figure 4.10: Comparison of the singlet excitation wavelength values for the orange (right) and blue (left) forms of DPM and its derivatives to the measured maximum wavelength (λ_{max}) in the visible range. Dichloromethane was used as solvent in both calculation and measurement.

surement overlap as is the case for the orange isomer of DPM and the blue isomer of o-Me. After the initial optimization of the orange isomer, the potential energy curve for the isomerization around the C=N double bond were computed by constraining the dihedral angle to fixed values between 0° and 180°. During this calculation however all the other internal coordinates were continuously optimized and no symmetry limitations were imposed. Cognizance of energy degeneracies at orthogonal geometry (90°) warranted the use of broken symmetry calculations which simply involves the rearrangement of alpha and beta electrons so that the molecule may pass through its transition state. The result of this calculation as presented in figure 4.11 shows the computed change in the ground state potential energy during twisting along the C=N rotational axis. Thus indicating the ground state isomerization of the orange isomer through a transition state at orthogonal arrangement towards the blue isomer. The pronounced barrier is similar to that of formaldimine as it is obtained at orthogonal geometry (see section 3.2.3). The computed barrier energy of 1.20 eV (orange to blue pathway) is less than half the experimental excitation energy of 2.63 eV (472 nm), which as expected is enough to overcome the barrier. However to fully describe the photo-induced isomerization of DPM, knowledge about the first excited state is also required. Unfortunately current calculations of the first excited state as a function of the dihedral angle is not conclusive and is notoriously difficult to calculate for large molecules. In the case of DPM the heavy mercury atom especially gives calculation difficulties which ultimately slows down the computation and result in less than accurate approximation for the potential energy [62]. The calculation of the highest occupied molecular orbital (HOMO) and the lowest unoccupied molecular orbital (LUMO) as displayed in figure 4.12 for the orange isomer does however elucidate some fundamentals of the photo-induced isomerization reac-

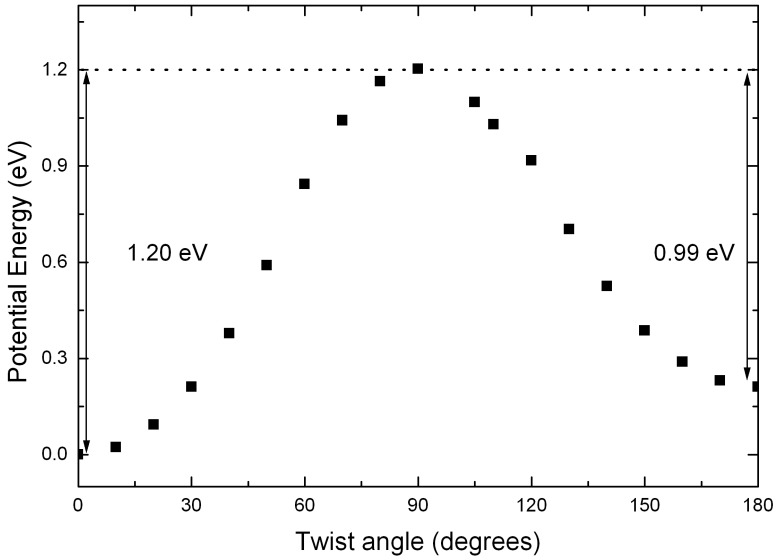

Figure 4.11: DFT calculated potential energy of DPM along the twist coordinate.

tion. More specifically, in order for free rotation to occur around the rigid C=N double bond, energetically it is more favoured for the π bond to be severed. This is indicated in figure 4.12 by the dashed circles which shows the C=N bond together with the given electron density. In the case of the HOMO, the density shows typical π bond character owing to the double bond formation. For the LUMO though a node appears in the electron density plot between the carbon and nitrogen atom which symbolizes that the double bond has been compromised. This can also be seen and similarly interpreted from the HOMO and LUMO of the blue isomer (figure 4.13). The electron density plots of the HOMO and LUMO for both the orange and blue isomers shows the delocalized π orbital system on the dithizonate backbone. This delocalization on the other hand does not appear on the phenyl attached to the Hg atom. Furthermore the relatively

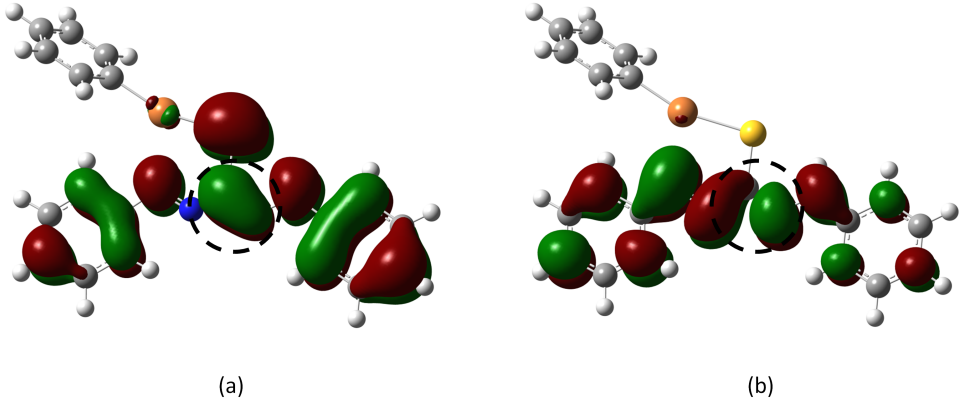

Figure 4.12: The HOMO (a) and LUMO (b) density plots for the orange isomer of DPM.

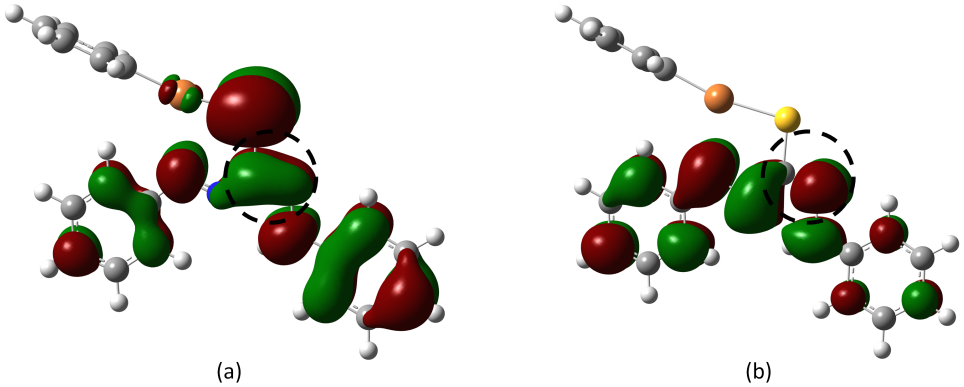

Figure 4.13: The HOMO (a) and LUMO (b) density plots for the blue isomer of DPM.

small electron density on the Hg atom itself suggest that the mercury atom and its attached phenyl ring need not be considered at photo-activation.

The ground state energy of the blue isomer is 0.21 eV higher than that of the orange isomer which means that the orange form is energetically favoured and more stable. What is clear from section 4.2 is that the blue isomer decays thermally with a potential energy barrier of 0.67 eV. If stipulating that the blue to orange isomerization pathway occurs along the twist coordinate the barrier energy would be 0.99 eV (figure 4.11) and is therefore not favoured. The minimum energy pathway of the back reaction is still being investigated and is proposed to be a combination of in-plane inversion (C1=N3-N4 angle) and the reorganization of the hydrogen atom on N4 (see figure 4.9).

5. UTA Measurements of Dithizonatophenylmercury(II)

The focus of this chapter as apposed to the previous one will be on the initial photochromic reaction of DPM and its derivatives in solution. In order to gain a greater understanding of this initial reaction and the subsequent relaxation of the molecular system, the technique of ultrafast transient absorption (UTA) spectroscopy was chosen as stipulated in section 2.3. The current UTA system at the Laser Research Institute (LRI) allows for detection of the change in optical density with a sensitivity of 10^{-4}. Also worth mentioning is that the linear translation stage used to delay the pump pulse with respect to the probe pulse has a travel of 100 mm. This translates to a maximum optical delay due to the retro-reflector setup of about 660 ps. The translation stage also has a minimum resolution of 0.1 μm and therefore a temporal delay of 0.67 fs, which is not used seeing that this will result in redundancies given that the temporal resolution is in the order of 70 fs. Considering thus the optical density sensitivity, the maximum optical delay and the temporal resolution of the setup. Detection of ground state bleaching (GSB), excited state absorption (ESA), fluorescence and phosphorescence should easily be achieved.

5.1 Sample Preparation

The concentration of a sample during any absorption type measurement is extremely important. In general, when the concentration of the test sample is too low, the issue of signal to noise arise. When it is too high, nonlinear absorption becomes a problem and in the case of DPM even dimerization could occur. Therefore to stay clear from these issues, it is required to choose a low concentration value which will result in low absorbance (linear regime) but high transmission. Thus a concentration is chosen which corresponds to a 80 to 90% transmittance. In order to calculate this concentration, the transmittance expression ($T = 10^{-\mathrm{OD}}$, eq. 2.10) is substituted in the Beer-Lambert expression ($\mathrm{OD} = \varepsilon c l$), resulting in the following

$$c = \frac{-\log T}{\varepsilon l}. \tag{5.1}$$

For DPM dissolved in dichloromethane a molar absorptivity (ε) at 470 nm of 57 300 $\mathrm{dm^3 \cdot mol^{-1} \cdot cm^{-1}}$ was previously calculated through UV/Vis steady state absorption spectroscopy. The pathlength (l) of the cuvette used in a typical UTA measurement is 100 μm, which means that concentration values between 170 (80% transmittance) and 80 (90% transmittance) $\mu\mathrm{mol/dm^3}$ are acceptable and therefore used.

5.2 The Initial Photochromic Reaction

Activation of the photochromic reaction in the majority of the samples were done using a NOPA pulse centered at 480 nm with pump energies of $80 - 150$ nJ. This translates to pump fluences in the order of $250 - 500$ μJ/cm^2 for a beam diameter at sample position of roughly 150 μm. The duration of the pump pulse for the various UTA measurements were determined before and after transient measurements and no substantial changes were detected. On average the duration of the pump pulses were between 30 and 50 fs. As for the probe pulse, white light generated in the 3 mm thick CaF_2 crystal was used. This permitted a large spectral window ($340 - 680$ nm) for the detection of the change in optical density. The diameter of the focused probe pulse at the sample was determined to be smaller than 50 μm. This was routinely checked before and after each measurement through replacing the sample with a 50 μm diameter aperture in the same plane, which when aligned properly showed no diffraction pattern.

In order to understand the initial photochromic reaction for DPM, its derivatives and solvent dependencies. DPM dissolved in methanol will be studied first as to lay the foundation for further examinations. The UTA measurements, results and discussions for DPM in methanol have already been published by us and is extended at this stage [11]. This is because there is a slight difference between the published work and the work as discussed here. In that the probe light in the UTA setup for the prior was generated in a 3 mm thick sapphire crystal rather than the 3 mm thick CaF_2 crystal. This ultimately changes the spectral range for the detection of the transient absorption signal. The effect this has on the description of the photochromic reaction will be highlighted. Figure 5.1 shows the temporally and spectrally resolved change in optical density $\Delta\text{OD}\,(t, \lambda)$ of DPM in methanol within the first 10 ps after excitation with a 40 fs pulse centered at 480 nm for the wavelength region between 300 and 650 nm. For times $t < 0$ the probe pulse arrives at the sample before the pump pulse and hence no change in the absorption spectrum is noted. This suggests that the relaxation dynamics is faster than the repetition rate of the laser and/or the activated sample volume from a previous pump pulse has been rapidly removed because of the flow cell geometry.[15] At $t = 0$ the pump and probed pulse impinge on the sample at the same time. This overlap of pump and probe generates the coherent artifact in the transient absorption signals (deleted form figure 5.1). The coherent artifact defines the onset of pump-probe overlap and is used not only to determine the chirp of the probe light, but also to correct for it. For times $t > 0$ the probe pulse arrives at the sample after the pump pulse and therefore detects the transient absorption spectrum.

[15] Remember at each time step the sample is pumped and probed or in this case ($t < 0$) probed then pumped.

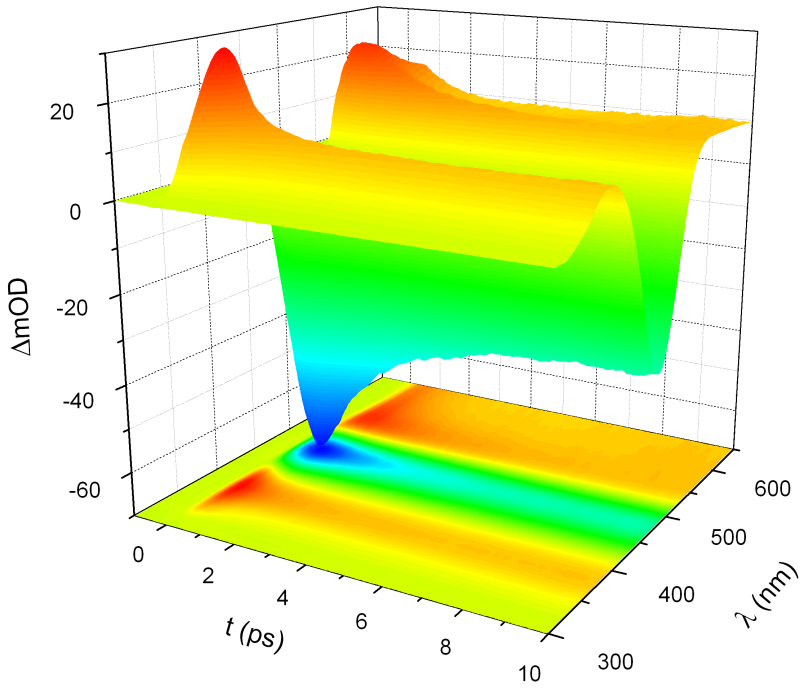

Figure 5.1: Transient change in optical density $\Delta\mathrm{OD}(t, \lambda)$ of DPM in methanol between 300 nm and 650 nm after excitation with a 40 fs short laser pulse centered at 480 nm.

The graph in figure 5.1 reveals the main features of the initial dynamics:

1. a fast increase and decay in absorption around 385 nm,
2. a fast decrease in absorption around 480 nm which partially recovers within a few picoseconds and
3. a fast and slightly asymmetric increase and subsequent decay in absorption between 520 nm and 650 nm.

The absorption band around 385 nm is not present in the steady state spectra and hence only appears after photo-excitation. The fast rise time and spectral location suggested that this band is due to ESA. The initial decrease in absorption around 480 nm is attributed to the depletion of the orange ground state in other words GSB. This is because the spectral location of the band coincides with the spectral position of the orange isomer of DPM in the steady state results. The absorption between 520 nm and 650 nm is ascribed to the formation of a photo-product. Which when considering the steady state results for DPM in dichloromethane can only be the formation of the blue isomer of DPM. This spectral region as previously stated has a slight asymmetry which is more evident in the contour plot given in figure 5.2.

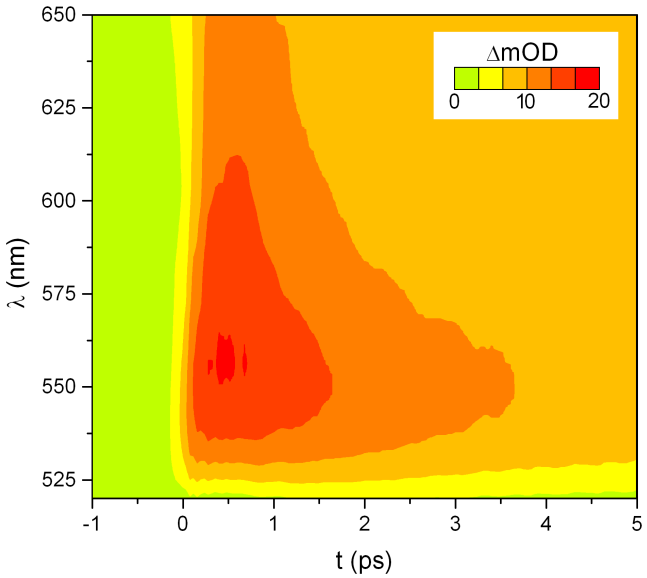

Figure 5.2: Contour plot of the transient change in optical density $\Delta OD\,(t, \lambda)$ of DPM in methanol between 520 nm and 650 nm.

This feature together with published work on the photo-induced isomerization of similar molecules is responsible for the interpretation that an intermediate specie is formed [8, 15, 38, 63, 64]. This intermediate or transient specie therefore should have a short lifetime given that re-population of the orange ground state occurs within a couple of picoseconds. Due to the overlapping of the various spectral signatures proper deconvolution both in the spectral and temporal domain is necessary to decipher the kinetics of singular species.

5.2.1 Kinetic Model

The first approach in determining the specific dynamical process and pathways for the photo-induced isomerization reaction is to assume an appropriate model for deactivation. The model is in the form of rate equations which couple the four species spectrally identified in figure 5.1. Figure 5.3 shows the overview of the proposed kinetic model. The model assumes that after initial activation of the orange isomer (O) to an excited orange isomer (O^*) at the Franck-Condon region. A transient specie (T^*) which is lower in energy (thus energetically favoured) is formed after which the orange ground state can be re-populated and/or the blue isomer (B) can be formed.

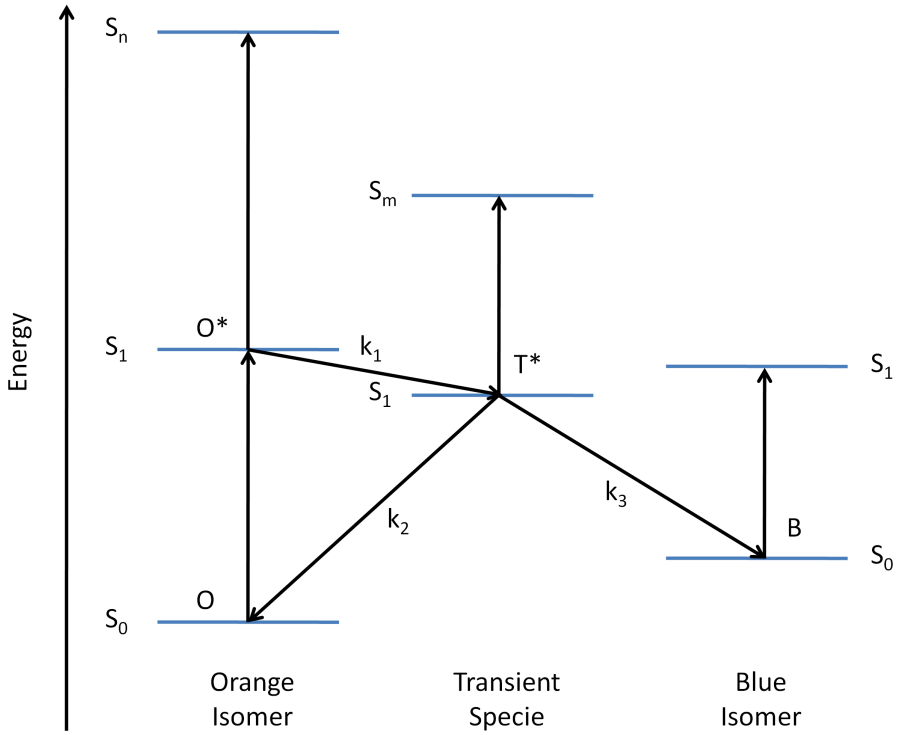

Figure 5.3: Energy diagram displaying the kinetic model for deactivation. The vertical arrows indicate absorption while the diagonal ones the nonradiative relaxation with rate constants k_1, k_2 and k_3.

Therefore starting at the excited orange isomer, the kinetic reaction scheme with reaction rates k_1, k_2 and k_3 can be formulated

$$\begin{array}{ccccc} \mathrm{O}^* & \xrightarrow{k_1} & \mathrm{T}^* & \xrightarrow{k_2} & \mathrm{O} \\ & & & \searrow_{k_3} & \\ & & & & \mathrm{B}. \end{array} \tag{5.2}$$

Which results in the following population equations,

$$\begin{aligned} \dot{n}_{O^*} &= -k_1 n_{O^*} \\ \dot{n}_{T^*} &= k_1 n_{O^*} - (k_2 + k_3)\, n_{T^*} \\ \dot{n}_{O} &= k_2 n_{T^*} \\ \dot{n}_{B} &= k_3 n_{T^*} \end{aligned} \tag{5.3}$$

where the dot on the various population terms (n_i) implies the explicit temporal derivative ($\frac{d}{dt}$). The solution of eq. 5.3 with initial conditions $n_{O^*}(0) = 1$, $n_{T^*}(0) = 0$, $n_O(0) = 0$ and $n_B(0) = 0$

reads

$$\begin{aligned} n_{O^*}(t) &= n_{O^*}(0)\exp(-k_1 t) \\ n_{T^*}(t) &= n_{O^*}(0)\left(\tfrac{k_1}{\alpha}\right)(\exp(-\beta t)-\exp(-k_1 t)) \\ n_{O}(t) &= n_{O^*}(0)\left(\tfrac{k_1 k_2}{\alpha}\right)\left(\tfrac{1}{k_1}\exp(-k_1 t)-\tfrac{1}{\beta}\exp(-\beta t)+\tfrac{\alpha}{k_1\beta}\right) \\ n_{B}(t) &= n_{O^*}(0)\left(\tfrac{k_1 k_3}{\alpha}\right)\left(\tfrac{1}{k_1}\exp(-k_1 t)-\tfrac{1}{\beta}\exp(-\beta t)+\tfrac{\alpha}{k_1\beta}\right) \end{aligned} \tag{5.4}$$

where $\alpha = k_1 - k_2 - k_3$ and $\beta = k_2 + k_3$. Figure 5.4 portrays the solution in eq. 5.4 graphically. Here the rate constants were chosen inspired by the first kinetic examination of DPM in methanol in order to elucidate the fundamentals of the kinetic rate model. As expected from eq. 5.4 the population of the excited orange isomer (O^*) decays exponentially with a time constant of $\tau_1 = 1/k_1 = 0.5$ ps.

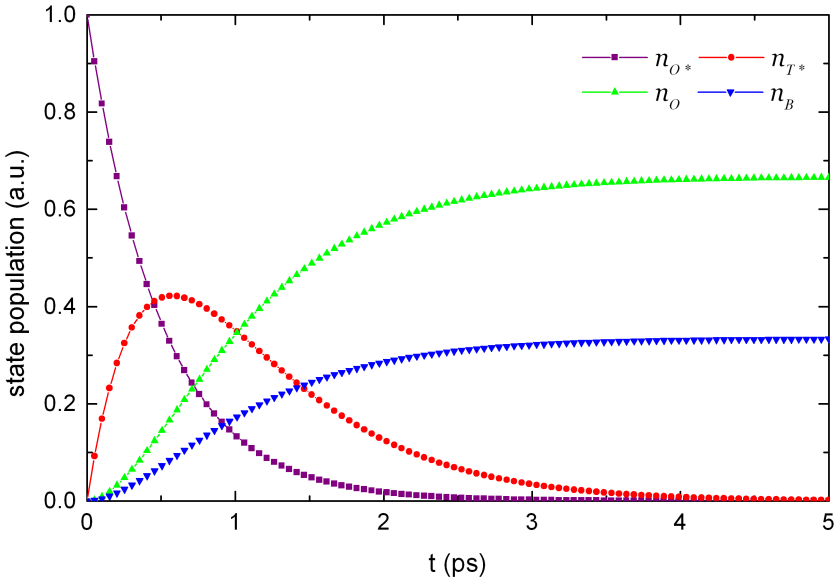

Figure 5.4: State population for the kinetic model in eq. 5.2. Arbitrary rate constants $k_1 = 2$ ps^{-1}, $k_2 = 1$ ps^{-1} and $k_3 = 0.5$ ps^{-1} were chosen.

The transient specie (T^*) has a fast initial increase in population ($\tau_1 = 1/k_1 = 0.5$ ps) which tails-off exponentially with a time constant of $\tau_\beta = 1/\beta = 0.6\dot{7}$ ps. Both the orange ground state (O) and the blue ground (B) starts with no population and increases exponentially to a constant value. The exponential growth of O and B depends on rate constants k_1 and β. However, if $k_1 \gg \beta$, which implies that the transient specie T^* is populated much quicker than the products are formed, the exponential growth can be considered only to depend on β. Another interesting result from the kinetic model is that the yield of O and B is coupled. This is easily shown by

dividing and rearranging the bottom two equations in eq. 5.4 resulting in

$$n_O(t) = \frac{k_2}{k_3} n_B(t) \tag{5.5}$$

or alternatively

$$n_O(t) = \frac{\tau_3}{\tau_2} n_B(t) \tag{5.6}$$

with $\tau_2 = 1/k_2$ and $\tau_3 = 1/k_3$. Hence if the time constant of O is greater than that of B ($\tau_2 > \tau_3$) meaning that O forms quicker than B, eq. 5.6 shows that also the yield of O will be proportionally more than that of B.

The above kinetic model, however does not fully agree with the experimental data. For example the ESA in figure 5.1 has both an initial fast decay (as described in the model) and a longer component (not described in the model). Also the initial conditions assume that the orange ground state is not populated at $t = 0$, which is not the case. The intermediate formation and subsequent decay as well as the product formation from the model though, agrees well with the experimental data in the time window of -1 ps to 10 ps as shown in figure 5.5. In figure 5.5 the population expressions in eq. 5.4 for the intermediate specie and product is first multiplied with a step function $\Theta(t)$[16] and then convoluted with the instrument response function (IRF) which is chosen as a Gaussian function (FWHM = 80 fs). The model is fitted to the data using *lsqcurvefit* in MATLAB 7.0 which allows for nonlinear least squares fitting. Here the coefficients of $n_{T^*} + n_B$ to best fit the transient data at 630 nm is $n_{O^*}(0) = 22.031$, $\tau_1 = 450$ fs, $\tau_2 = 631$ fs and $\tau_3 = 1.622$ ps. Conclusions on the significance of time constants (τ_1, τ_2 and τ_3) for describing the kinetics are reserved at this stage. The reason being that fitting at a different wavelength within the same absorption band (for both the product and reactant) result in slightly different time constant values. Therefore additional information about the spectral content of the four identified species (O, O*, T* and B) should be included for the best possible fit. Despite this inefficiency of the kinetic model it does however supply a meaningful description for deactivation which is that after the reactant is excited, a transient specie is formed which then either repopulate the reactant or form a product.

5.2.2 Global Fitting

The term global fitting in this work implies that the reconstruction of the experimental transient change in optical density $\Delta OD(\lambda, t)$ is possible through the use of parameters extracted from both temporal and spectral fitting. Here the reconstruction initially requires the simultaneous

[16] The step function ensures that at times $t < 0$ ($\Theta(t) = 0$) no kinetics without activation occurs. Whilst for times $t \geq 0$ ($\Theta(t) = 1$) kinetics are allowed.

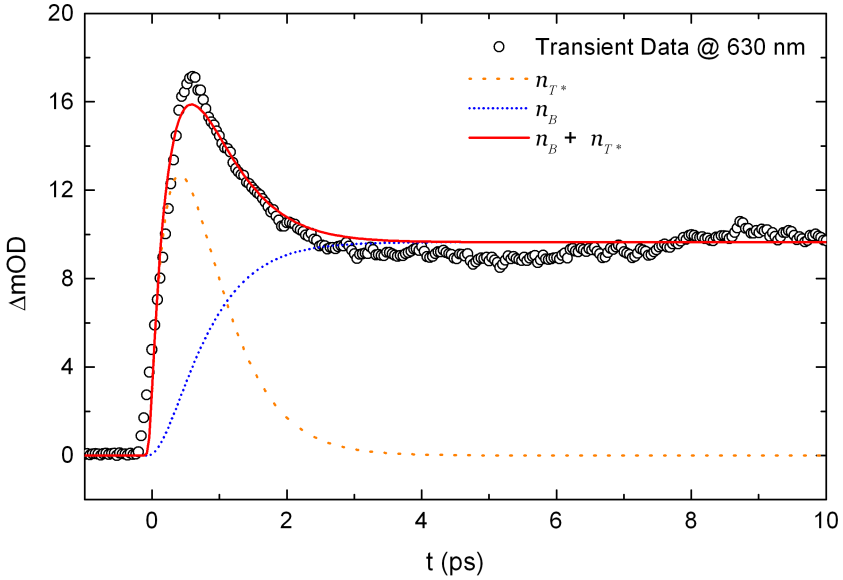

Figure 5.5: Transient change in optical density for DPM in methanol at 630 nm with the appropriate fit from the kinetic model. The experimental data (open circles) were averaged over a spectral bandwidth of 5 nm. The solid red line is the sum of the population for the transient specie (dotted orange line) and the product (short dotted blue line). Here convolution with the response function is implied.

fitting across the entire transient spectra. To accomplish this, it was assumed that the spectral signature of each of the four species can be approximated through a Gaussian function. This form of spectral decomposition therefore does not allow for the existence of any other intermediate species. In order to check whether this assumption is acceptable, a spectral slice at 1 ps after pump-probe overlap from the data displayed in figure 5.1 is selected to which the sum of four Gaussian functions is fitted using the same method as described earlier (*lsqcurvefit* in MATLAB 7.0). Figure 5.6 shows the result of this spectral fitting procedure together with the residual. The residual is merely the absolute value of difference between the data and the fit values, which when taken the average of is equal to 0.12 ΔmOD. This low number indicates that on average the spectral fitting at this particular time step is quite reasonable for this model. During this fitting procedure the amplitudes, the center wavelengths (λ_0) and the bandwidths ($\Delta\lambda$) which represents the spectra of the four species (O, O*, T* and B) are optimized (see table 5.1).

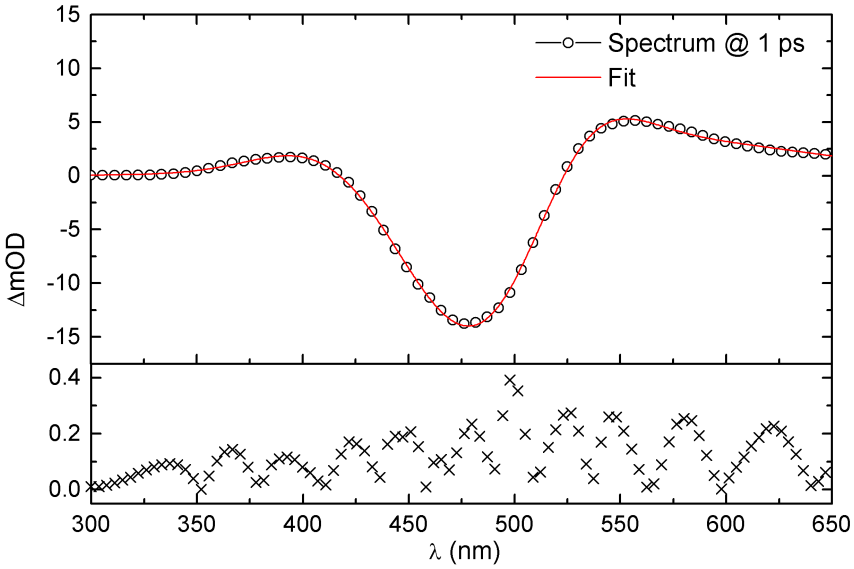

Figure 5.6: Transient change in optical density for DPM in methanol 1 ps after pump-probe overlap. The experimental data (open circles) is filtered using adjacent averaging with a bandwidth of 5 nm . The solid red line is the sum of the four Gaussian functions, whilst the residue is plotted as crosses.

Following this the outer-product of the individual spectral profile functions are taken with the temporally fitted kinetic traces at the specified center wavelength given in table 5.1. The sum of the four outer-products then represents the reconstructed change in optical density $\Delta\mathrm{OD}_{\mathrm{rec}}(\lambda, t)$ which is further optimized globally through changing the time constants (τ_i's) within a least squares algorithm in order to minimize the following difference,

$$\sum_{\lambda,t} |\Delta\mathrm{OD}(\lambda, t) - \Delta\mathrm{OD}_{\mathrm{rec}}(\lambda, t)|^2 . \tag{5.7}$$

Eq. 5.7 is the absolute squared difference between the reconstructed and the measured change in optical density summed over the free parameters of λ and t. Which when minimized within a *Levenberg-Marquardt* algorithm results in optimized values for the time constants. The kinetic traces used here are inspired by the ones obtained from the kinetic model (eq. 5.4) but has been

Table 5.1: Optimized parameters for spectral fitting of the transient data 1 ps after pump-probe overlap, using a four Gaussian function model.

Specie	λ_0 (nm)	$\Delta\lambda$ (nm)	Amplitude (ΔmOD)
O	485.9	85.5	-18.3
O*	407.2	65.9	2.1
T*	549.3	199.9	3.7
B	529.1	62.4	7.3

altered slightly as to fit the transient data efficiently (see below).

$$n_i^{new}(t) = \sum_{j=1,2} a_i^j \exp\left(-t/\tau_{a_i^j}\right) + b \quad \text{where } i = O^*, T^*, O \text{ and } B. \tag{5.8}$$

It is clear from the equations above that the state population of each specie is described by the sum of two exponential terms. The only difference therefore between the new state population equations and the original ones is the addition of an extra exponential component to the population of the excited orange isomer O^*. Figure 5.7 displays the optimally reconstructed transient change in optical density versus the experimental trace.

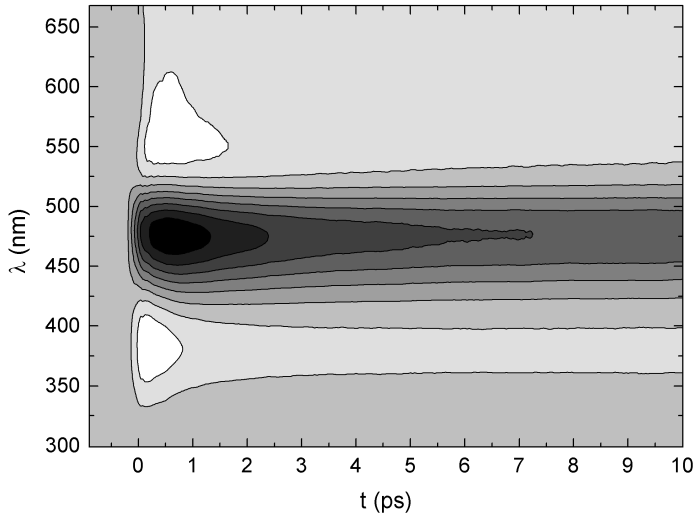

(a) Experimental.

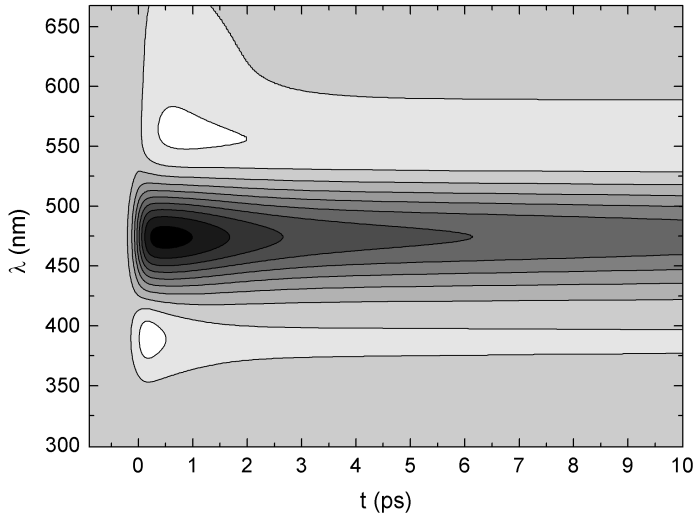

(b) Reconstructed by global fitting.

Figure 5.7: Contour plots of the transient change in optical density $\Delta\text{OD}(t, \lambda)$ of DPM in methanol.

In order to better appreciate the accuracy of the reconstructed plot. Three temporal slices at the fixed wavelengths of 395 nm, 480 nm and 650 nm are taken from the two traces in figure 5.7 and plotted in figure 5.8. These positions are chosen as to illustrate the temporal evolution of the ESA around 395 nm, the GSB around 480 nm and the interplay between the formation of both the intermediate specie and the photo-product around 650 nm.

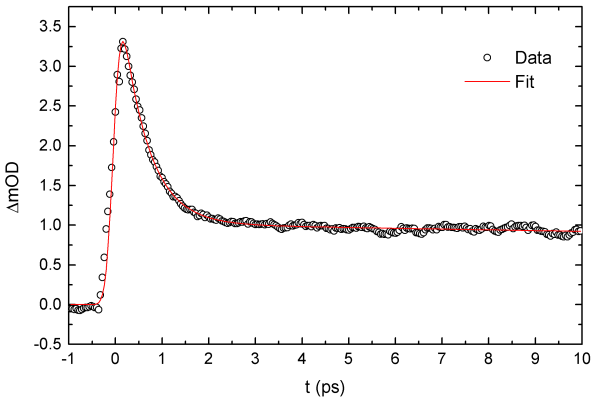

(a) 395 nm

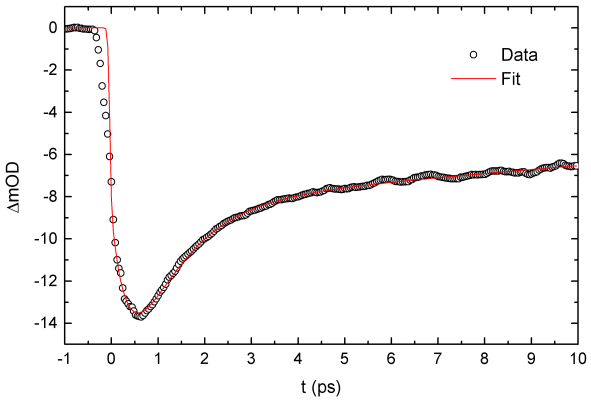

(b) 480 nm

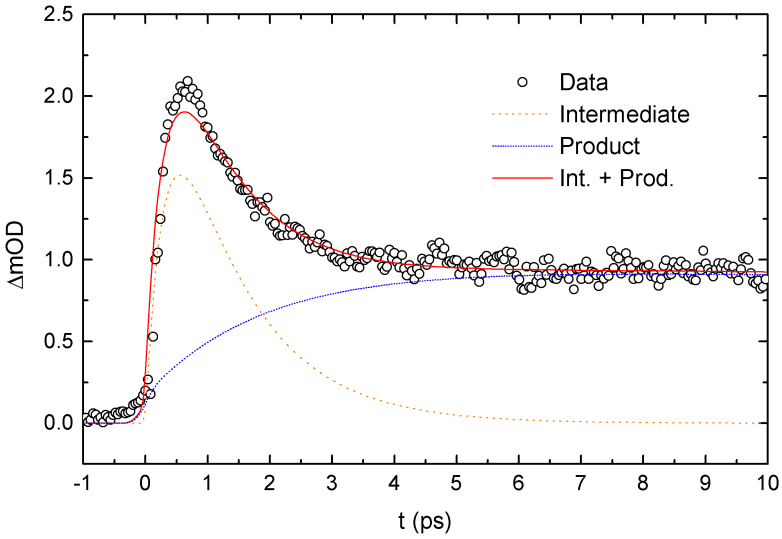

(c) 650 nm

Figure 5.8: Temporal evolution of the transient change in optical density for DPM in methanol at selected wavelengths.

In figure 5.8 (b) the change in optical density initially decreases by -14 mOD which constitutes a percentage increase of 1.4 % in transmission within the first 500 fs after pump-probe overlap. After which the signal increases by about a 1/3 with a time constant of roughly 1.4 ps. Further-

more, within the given time window of 11 ps, this GSB band also recovers one half of its original signal at a time constant of about 41 ps. This indicates that there exist at least two pathways for deactivation one fast (1.4 ps) and the other slow (41 ps). Considering only the faster dynamics (¡ 10 ps), the initial depletion of the GSB band must occur within the pump pulse duration of 40 fs. This means that with the given temporal resolution (IRF, FWHM = 80 fs) the GSB signal's initial depletion should be completed within the 80 fs. Which is not the case, as it is measured to be around 500 fs. The reason for this is due to the spectral overlapping of the ESA band with the GSB band. Figure 5.8 (a) depicts the short initial decay of the ESA and a longer decay component with time constants of 500 fs and 76 ps respectively. It is important to stress that for both the ESA and GSB that the longer time constant values of 41 ps and 76 ps are not as accurate as the shorter time constants because they exceed the time window.

The open circles in figure 5.8 (c) shows the measured transient change in optical density at 650 nm together with results from the model. Here the signal initially increases to 2.2 mOD in less than 500 fs, followed by a decrease of about 1/3 with a time constant of about 1.3 ps. This fast increase and slow decrease is attributed to the existence of an intermediate specie. After about 4 ps the signal flattens out to a value which is approximately half of the maximum. The flattening in this case is largely due to the formation of a product with a time constant of roughly 1.6 ps. The given time constants were extracted from the fit (as indicated) which is merely the sum of the product absorption and the intermediate specie absorption. This is done because of the almost complete spectral overlapping of the two specie's absorption profiles.

5.2.3 Discussions

After the physical processing of the transient absorption spectroscopy data for DPM in MeOH, a consistent interpretation for the initial photochromic reaction can be formed. Photochromism in DPM, as stated before, is due to a photo-induced isomerization reaction. In the case of simple azomethines thermal isomerization proceeds through inversion, while photo-induced isomerization proceeds along a twist coordinate [5, 38, 57]. In addition, the theoretical work on the prototypical formaldimine in chapter 3.2.3 also concluded that rotation around the C=N double bond is energetically preferred above in-plane inversion. Keeping this in mind the observed transient absorption changes for DPM are interpreted to occur between the first excited state S_1 and the ground state S_0 along the rotation coordinate of the C=N axis, with the formation of a conical intersection (CI) at orthogonal geometry. Figure 5.9 displays the proposed isomerization pathway for DPM on a hypothetical potential energy curve as a function of the rotation coordinate. As indicated, the molecule, is initially in the S_0 ground state of the orange form O.

The pump pulse ($\lambda \approx 470$ nm) then generates a molecular wavepacket within its duration of 40 fs on the first excited state S_1, vertically above the orange ground state. This wavepacket at O^* immediately moves out of the Franck-Condon region towards the CI at orthogonal geometry (path (i)). During this evolution the molecule is actually internally redistributing its vibrational energy. Which causes a delay of about 1.3 ps before it reaches orthogonal geometry. Once here the molecular wavefunction which is now on a minimum of the excited state at position T^* funnels through the CI towards a maximum on the ground state S_0. At this maximum the probability for the wavepacket to evolve towards the original orange ground state at O along path (ii) and towards the product blue ground state at B is equal if the position of the minimum of S_1 coincides with the maximum of S_0. For DPM in MeOH this seems to be the case as the re-population time (1.4 ps) of the O is similar to the population time (1.6 ps) of B[17].

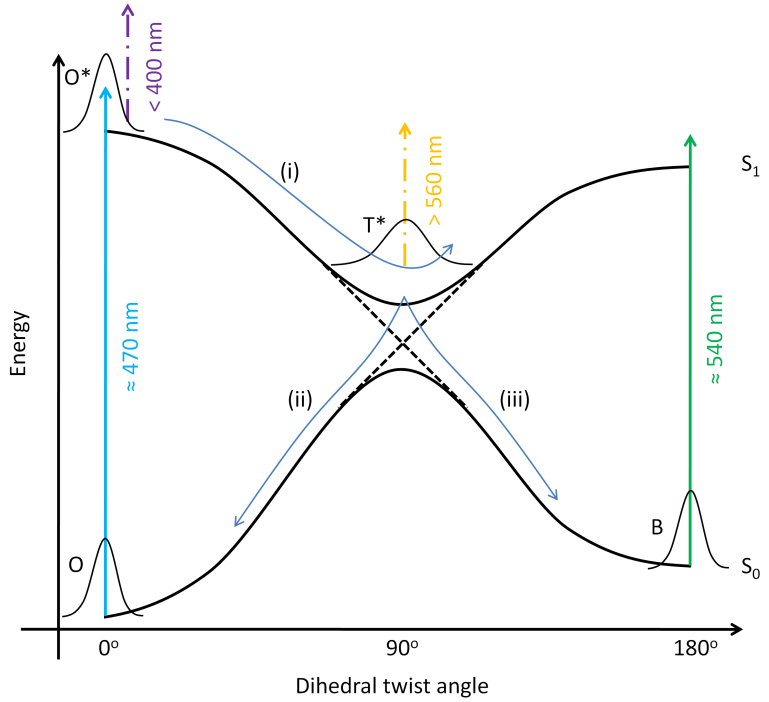

Figure 5.9: Schematic overview for the proposed isomerization pathway of DPM after $S_0 \rightarrow S_1$ photo-excitation. The wavepacket at O^* moves on S_1 via path (i) towards a conical intersection at T^* with S_0. Here it funnels onto S_0 where it bifurcates towards the reactant O path (ii) and the product B path (iii).

It should be stated that the general view of the dynamics of the wavepacket on the excited state in the CI region does not contradict the aforementioned one. Conventionally, when passing the CI the wavepacket only partially penetrate the funnel populating the product B. The rest

[17] Time constants varies by 10% depending on the data set processed.

of the wavepacket travels slightly up the slope on S_1(after orthogonal geometry) and returns again only partially penetrating the funnel re-populating the reactant O. Now the diminished wavepacket travels up the slope in path (i) and returns partially populating B again as the rest continues the cycle. This oscillation of the wavepacket on S_1 continues until the entire wavepacket is depleted at T^*. The experimental confirmation of this wavepacket oscillation is however not readily obtained for large molecules in liquid phase. Thus it is assumed that the features that would result from this oscillation is largely smoothed out due to insufficient temporal resolution and the possibility of other coherent motions on the excited state.
The occurrence of a CI normally results in an efficient deactivation pathway which allows very little time for a process like fluorescence. This has been confirmed because DPM when excited with 480 nm light exhibits no fluorescence (quantum yield $\approx 1 \times 10^{-4}$) in the wavelength region 480-700 nm in either of the solvents, DCM and methanol, confirming earlier measurements [11]. The method used here to detect fluorescence is summarized in appendix A. Besides the lack of fluorescence due to the efficient CI pathway, a rate determining step for the formation of the product and re-population of the reactant is according to the kinetic rate model, the formation of the intermediate specie. The rate determinig step, in terms of kinetic reactions, will influence the yeild of both product or re-population of reactant. This however is not focused on throughout this dissertation.

5.3 The effect of the solvent

In this section the UTA measurements, results and discussions of DPM when dissolved in various solvents are focused on. The solvents that will be concentrated on here are dichloromethane (DCM) and deutero methanol (MeOD). Comparison studies are required in order to determine the effect these solvents may or may not have on the initial ultrafast dynamics of the photochromic DPM. The case of DPM dissolved in methanol from the previous section will therefore be used as a benchmark. The UTA measurement for DPM in all the solvents have roughly the same profile and thus to avoid the redundancy of plotting similar looking three dimensional traces, only the spectral and temporal slices will be displayed and characterized.

5.3.1 Spectral Comparisons

Starting with the spectral comparisons, figure 5.10 shows the change in optical density for DPM in the various solvents 1 ps after pump-probe overlap. The three vertical lines indicate the pronounced features of the transient spectrum for DPM dissolved in methanol, whilst the arrows shows the relative shifts from these features for DPM dissolved in the other two solvents. Qual-

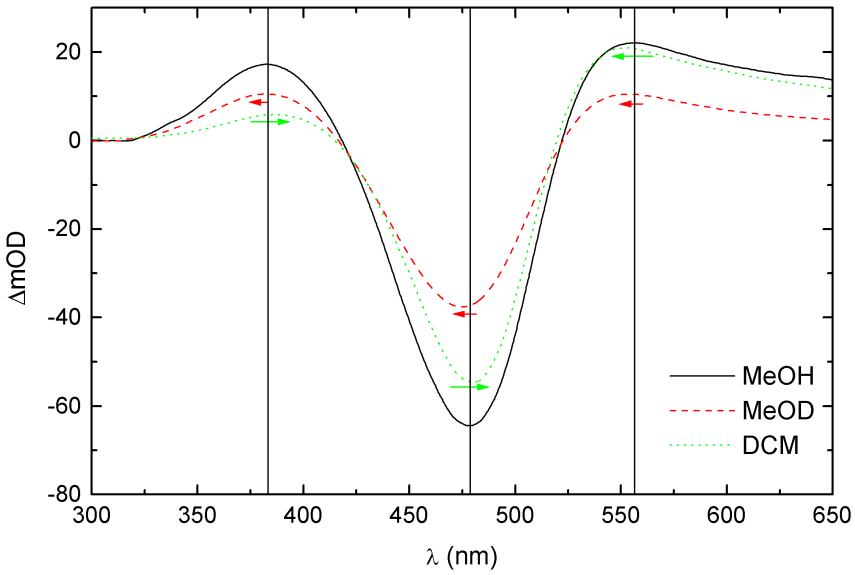

Figure 5.10: Spectral slice of the change in optical density for DPM in DCM, MeOD and MeOH 1 ps after pump-probe overlap.

itatively speaking, the shifts for DCM are larger than that of MeOD after 1 ps. Using MeOD as solvent though results in an effective blue-shift across the entire spectrum as compared to methanol. This is however not so for DCM at the given temporal delay. The transient spectrum in this case shows pronounced red-shifts at the ESA and GSB regions while a definite blue-shift is visible at the product and intermediate specie absorption band. For quantitative analysis of the spectral shift at the maximum amplitude wavelength λ_{max} positions, spectral slices of the data between 1 ps and 10 ps were taken from which the λ_{max} values are determined and plotted in figure 5.11. In figure 5.11 (a) the spectral shift at λ_{max} for DPM in MeOH and MeOD respectively follow a similar trend. This trend being a slight blue-shift after 1 ps followed by a strong red-shift towards 10 ps. Interestingly, the blue-shift for MeOH reaches a minimum at about 1.9 ps whilst MeOD only reach a minimum after about 2.4 ps. On the overall the λ_{max} values for MeOD is blue-shifted with respect to MeOH. For DPM dissolved in DCM an almost mirrored trend in this spectral region is observed. Here an initial red-shift reaching a maximum after about 2.4 ps is followed by a sharp blue-shift which even intersects the spectral shifts of both MeOH and MeOD.

The trend of λ_{max} for MeOH and MeOD in the region of the GSB band (see figure 5.11 (b)) is almost identical to the shift at the ESA region. The greatest difference being that the total blue-shift of MeOD with respect to MeOH is larger. For DPM in DCM on the other hand no specific time dependence of λ_{max} is observed in this range. In the spectral region of the product and intermediate specie (figure 5.11 (c)) the dominant characteristic shift of DPM in MeOH and

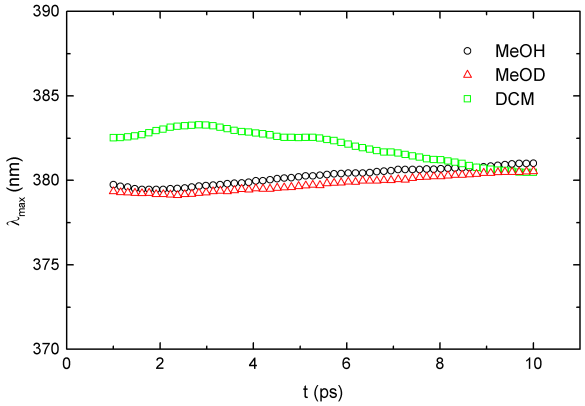

(a) ESA band.

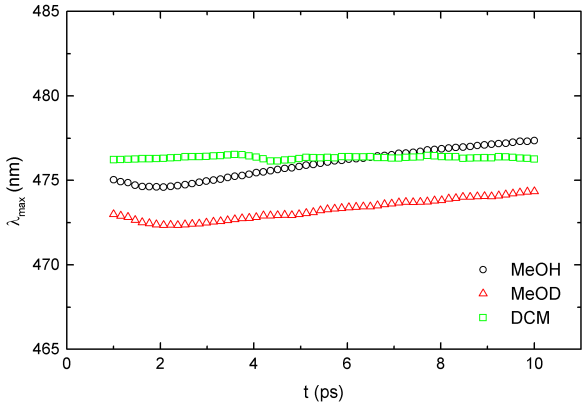

(b) GSB band.

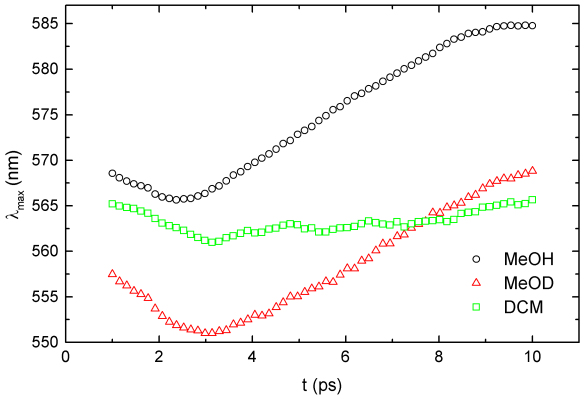

(c) Product and intermediate specie absorption band.

Figure 5.11: Wavelength positions λ_{max} as a function of time at the pronounced features in the transient absorption spectra for DPM dissolved in MeOH, MeOD and DCM.

MeOD continues but the effective blue-shift of MeOD becomes larger still. Interestingly here DPM in DCM also shows a significant blue-shift as compared to DPM in MeOH. Further discussions of the spectral shift, will be limited to the ESA and GSB regions. This is done because the spectral maximum for the product and intermediate specie is indistinguishable due to the current method of detection. The almost ubiquitous occurrence of the spectral shift albeit red or blue can be attributed to a large number of effects. Effects such as hydrogen bonding which ultimately changes the vibrational structure of the spectrum, normal acid-base chemistry and internal charge transfer [65]. In general thus, it is the interaction of the dipole moment of the molecule with its surroundings which is responsible for the spectral shift. The solvents used however does not allow for a concrete explanation of the spectral shift, because a meticulous study of the variation of the solvent polarity, proticity, acidity, viscosity and temperature is required. What can be concluded though is that the electron lone pairs on the nitrogen atoms of the dithizonate backbone of DPM acts as electron donors in a hydrogen bond with the solvent

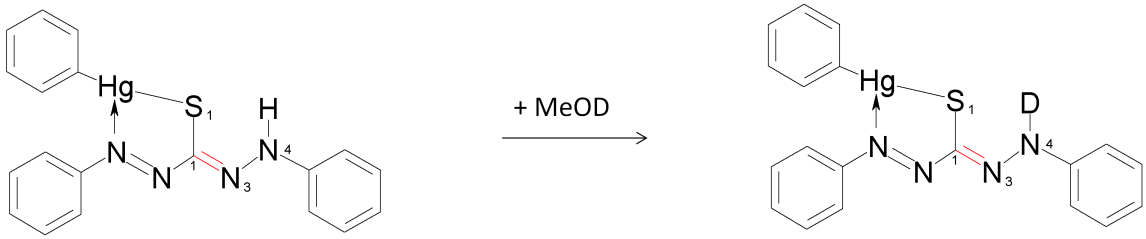

Figure 5.12: Proton substitution reaction in DPM when dissolved in MeOD.

molecule (MeOH). This lowers the energy by an amount equal to the hydrogen bond energy itself, which causes an increased energy gap between the ground and excited state. Thus explaining the blue-shift of the spectrum for DPM dissolved in MeOH as compared to DCM, because the former is a protic solvent and the latter an aprotic solvent. In the case of MeOD, it is widely accepted that dissolving a substance in this type of solvent would result in the exchange of the labile protons by the deuterated ones (see figure 5.12). This effective proton transfer alters thus potentially both the ground state and the excited state of the molecule leading to a dominant blue-shift in the spectrum. This can also be understood from a quantum mechanical point of view. In that the heavier deuterated proton causes the zero-point energy to decrease because the reduced mass has increased, thus increasing the energy gap between the ground state (HOMO) and the excited state (LUMO).

5.3.2 Temporal Comparisons

This section deals with the changes of the reaction dynamics that occurs in the ESA, GSB, product absorption and intermediate specie absorption regions when altering the solvent. The time constants extracted here is done in accordance to the model described in section 5.2. However, slightly different values for the time constants will be generated because the spectral dependence in the aforementioned regions are neglected.

Figure 5.13 (a) displays the transient change in optical density of DPM in the different solvents at the ESA region. Here a two-exponential fit is chosen to determine the fast and slow rates which is visible in all three. For the GSB region in figure 5.13 (b) a three-exponential fit is used to determine the time constants of the initial depletion, the slow and the fast components of re-population. Lastly the fit used to determine the product formation and intermediate specie formation is also a three-exponential one. Due to the similarity of the data for DPM dissolved in MeOH and in DCM at this particular wavelength, the latter was scaled to 75%. The fit in this region describes the initial formation and the decay of the intermediate, as well as the formation of the product. The various extracted time constants from the fits are summarized in table 5.2.

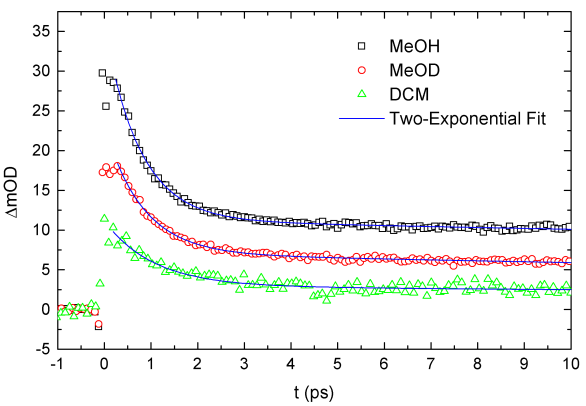

(a) ESA maximum.

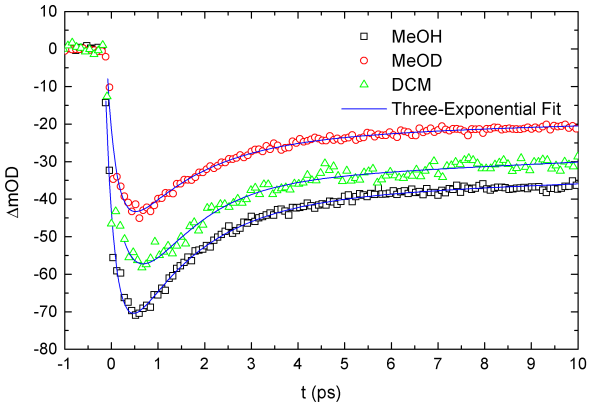

(b) GSB maximum.

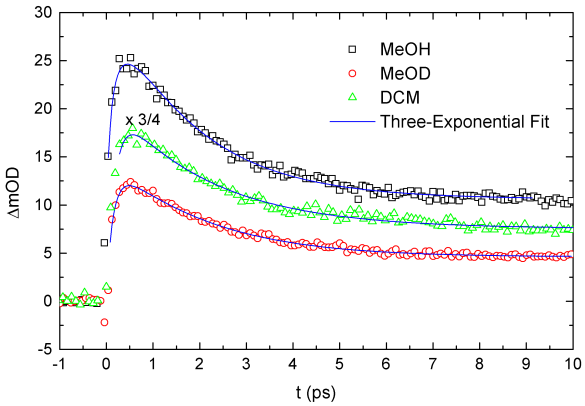

(c) Product Absorption.

Figure 5.13: Transient change in optical density for DPM in various solvents.

These values are within the 95% confidence bounds of the fit coefficients. There is a noticeable difference in time constant values is observed for the fast component of the ESA fit (first column of ESA in table 5.2) for the various solvents. The values seems to suggest that the lifetime of the orange excited state is shorter when DPM is dissolved in methanol as compared to the other two. For the slow component of the ESA fit, no real importance is attached because the values are all larger than the sample window (10 ps). The first column under the GSB heading in table 5.2 shows the time constants for the initial depletion of the ground state. Which as previously mentioned is only present due to the partial spectral overlap of the ESA and the GSB band. More importantly however is the second column. These time constant values signifies the fast re-population of the ground state. Here it seems that DPM in DCM has the fastest re-population followed by MeOH and then MeOD. The third column also pertains to ground state re-population but the rather large values questions their accuracy.

Under the last heading in table 5.2 the intermediate species population time (1st column in

Prod), its decay time (2nd column in Prod) and the product formation time (3rd column in Prod) is indicated. The time constant values displayed here mirror the similarity seen in the plots of the transient change in optical density at this region for DPM in the different solvents (figure 5.13 (c)).

Table 5.2: Time constants extracted from the fits in figure 5.13.

Solvent	ESA		GSB			Prod		
	τ_{decay}		τ_{grow}	τ_{decay}		τ_{grow}	τ_{decay}	τ_{grow}
MeOH	0.76	89.1	0.216	1.55	80.7	0.22	1.93	1.65
MeOD	0.82	54.2	0.219	1.61	60.9	0.19	2.04	1.71
DCM	1.08	66.3	0.485	1.03	47.9	0.25	2.01	1.60

All values are in ps. $0.4 - 4$ % error on fit values.

In using the proposed model for DPM in MeOH as benchmark, MeOD as a solvent leads to slower dynamics, meaning that the overall initial isomerization after photo-excitation occurs on a slightly longer timescale. Thus verifying that proton transfer (or exchange) definitely occurs from the solute to the solvent and vice verso. Taking this into consideration, the overshadowing reason for longer dynamics is thus due to the kinetic isotope effect [66]. This effect is defined as the ratio of the reaction rates between two isotopically labeled molecules which take part in a chemical reaction of some sort.

If the substituted isotope forms part of a chemical bond which might be broken or formed during the reaction, significant changes in the reaction rates are observed. This is commonly termed the primary isotope effect. In DPM however (see figure 5.12) after the substitution of deuterium, photo-activation and subsequent energy dissipation occurs through *cis-trans* isomerization.
This means that the isotopic substitution falls under a different class named the secondary isotope effect, which as seen only result in slight changes to the reaction rates (or time constants). Here it is clear that the heavier

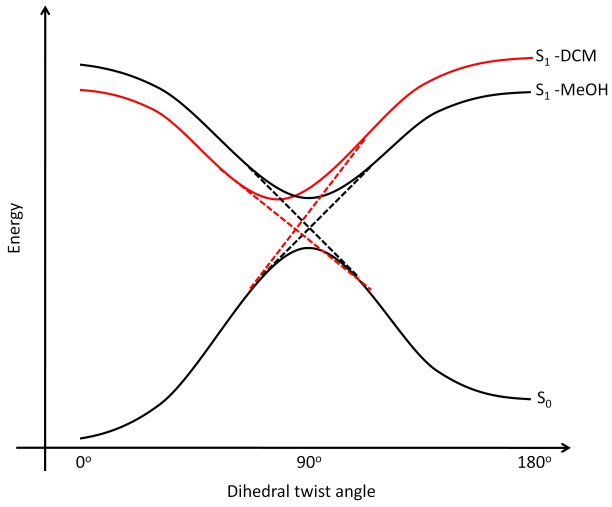

Figure 5.14: Proposed schematic of the potential energy curves for isomerization of DPM in DCM MeOH.

deuterium causes longer time constants meaning that the isomerization is slowed down due to the increased inertia.
In DCM where proton transfer is not readily achieved, longer lifetimes of the excited orange isomer is observed, whilst faster re-population of the orange ground state and identical population times for the blue isomer ground state as compared to MeOH is seen.
The increased excited state lifetime suggests that the potential energy curve on S_1 at the Franck-Condon region might be lower (see figure 5.14) or that a less prominent potential energy curve gradient is formed towards the conical intersection. Also the faster re-population of the ground state could be explained through a small shift in the excited state potential energy curve's minimum towards twist angles smaller than 90°, together with a larger slope of the S_1 curve after the minimum position. In fact, this energy curve shifting has already been hinted towards in the previous section. Especially seeing that for this proposed shifting, a lowering in the excitation energy of the orange isomer and a raising in the product absorption energy is required, which is clearly visible in the experimental data shown in figure 5.11[18].

5.4 The effect of the substituent

Adding a substituent to the phenyl rings on the dithizonate backbone of DPM resulted in a shift in the steady state absorption spectrum (section 4.1) as well as measurable differences in the kinetics of the back reaction (see section 4.2.2). This essentially allowed for a description of the possible minimum energy path for the back reaction. Keeping with this methodology, in this section light will be shed on the effect this substitution has on the initial photochromic reaction. Apart from the unsubstituted DPM, 11 electronically altered samples all dissolved in dichloromethane have been investigated. The UTA data of all are analyzed using the kinetic model and the subsequent results are summarized in table 5.3. The extracted parameters in table 5.3 are arranged according to the four species which are assumed in the kinetic model. Once again O is the orange ground state, O* the orange excited state, T* the intermediate state and B the blue ground state. Also only the respective wavelength values at the amplitude maximum (λ_{max}) of the spectral profile after 1 ps for O, O* and B as well as the relevant time constant (τ's) values including that of T* are given. The time constant for the orange isomer O indicates the re-population time, whilst the time constant at the excited orange state is its lifetime. For the intermediate state (specie) T*, τ_{grow} is the formation time with τ_{decay} being the decay time. Lastly, the time constant at the blue isomer ground state B column is the formation time of the product. Due to the sheer volume of sample set and the similarity in the extracted values (table

[18]Remember the energy-gap and excitation wavelength proportionality, $\Delta E \propto 1/\lambda_{exc.}$.

Table 5.3: Extracted parameters of the UTA measurements on the electronically altered DPM samples.

	O		O*		T*		B	
	λ_{max}	τ_{decay}	λ_{max}	τ_{decay}	τ_{grow}	τ_{decay}	λ_{max}	τ_{grow}
DPM	477	1.03	384	1.08	0.24	2.0	560	1.6
m-F	476	1.42	384	1.18	0.33	1.7	555	2.5
m-Me	483	1.36	387	1.02	0.406	2.3	559	4.4
m,p-diMe	493	1.53	394	1.27	0.23	2.5	570	2.5
o-F	474	1.95	380	0.97	0.15	2.3	552	2.3
o-Me	470	0.51	374	0.68	< 0.1	1.7	555	1.7
o-OMe	507	1.02	397	0.85	0.42	1.9	584	1.9
o-SMe	500	1.61	387	1.22	0.34	2.4	577	2.4
p-Cl	488	1.91	390	1.17	0.165	2.6	560	2.6
p-F	479	1.35	384	0.97	0.112	1.9	555	1.9
p-Me	489	1.28	393	1.08	0.195	2.5	567	2.5
p-SMe	519	3.79	426	1.54	0.53	3.6	613	3.6

λ's in nm and τ's in ps. $0.4 - 4$ % error on fit values.

5.3) of a number of them only a particular selection will be investigated with greater detail. In particular, o-Me and p-SMe which is highlighted in red in table 5.3 are important examples. This is because the o-Me group is known to be electron accepting, whilst the p-SMe group is an excellent electron donator. Therefore to determine the effect of substitution one has to compare the substituted samples against the unsubstituted DPM in DCM sample. These comparison will be the focus of the next subsections reserving the last for some interesting observations made in both the spectral and kinetic traces for selected samples.

5.4.1 Ortho - Methyl Substitution

When looking at the time constant values for o-Me in comparison to that of DPM (table 5.3), its is clear that the majority of the processes are faster. This shortened lifetime of the various states implies that the o-Me excited state is less stable than that of DPM. One reason for this inherent instability could be due to the specific position (see figure 5.15) of the methyl group, which may sterically hinder the molecule. This sterical effect spawn from possible hydrogen bonding between the hydrogen atoms on the substituted methyl and the nitrogen atoms on the backbone[19].

The substitution of the hydrogen atom at the ortho position of both phenyl rings with methyl however, definitely changes the electronic charge distribution across the entire molecule. It is this charge distribution on the dithizonate backbone which have the largest effect on the rate of isomerization and the absorption wavelength.

[19]Investigations of hydrogen bonding is still being undertaken through DFT calculations.

The backbone being largely photo-active delocalized π orbitals which when contracted result

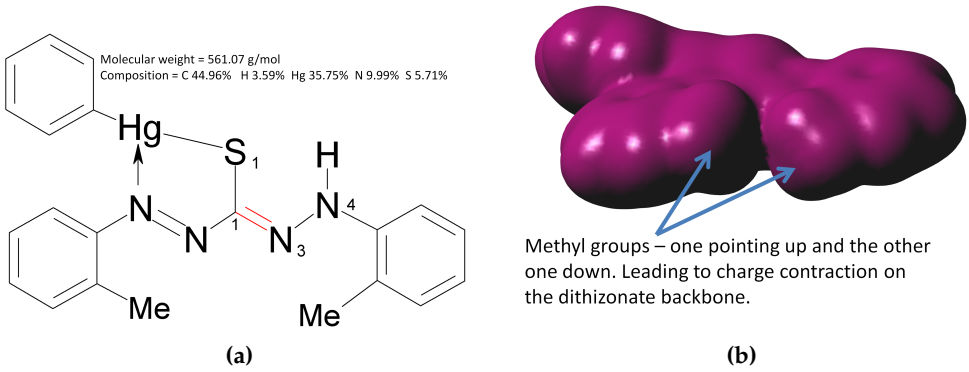

Figure 5.15: Chemical structure of ortho (o)-CH_3(or Me) DPM (a) and its total charge density (b) showing that the substituent distorts the original planar geometry of DPM.

in decreased values of the absorption wavelength. To understand this one only need to invoke the quantum mechanical image of a particle in a one dimensional box. Where if the width of the box is decreased (contracted charge distribution) the energy level spacings are increased (decrease in wavelength). For o-Me thus the ubiquitous blue spectral shift (neglecting solvent effect) in comparison to the unsubstituted DPM implies a contraction of the charge distribution due to the distortion of the planar geometry (see the total charge density plot in figure 5.15) which result in faster isomerization rates.

Using the spectral shift and isomerization rate information, a proposed potential energy landscape of the ground state S_0 and the excited state S_1 of o-Me can be formed. Hence the specific form of the potential energy curves in figure 5.16 for o-Me is a result of the extracted data. For o-Me thus there is a definite increase in excitation energy ($S_0 \rightarrow S_1$) with a steeper slope on the S_1 curve on either sides of the minimum. The ground state of o-Me however is assumed to be identical to that of DPM. This assumption is the result of ground state DFT calculations which is summarized in theory [62]. Therefore photo-induced isomerization for o-Me follow a similar mechanism to that of DPM. Where $S_0 \rightarrow S_1$

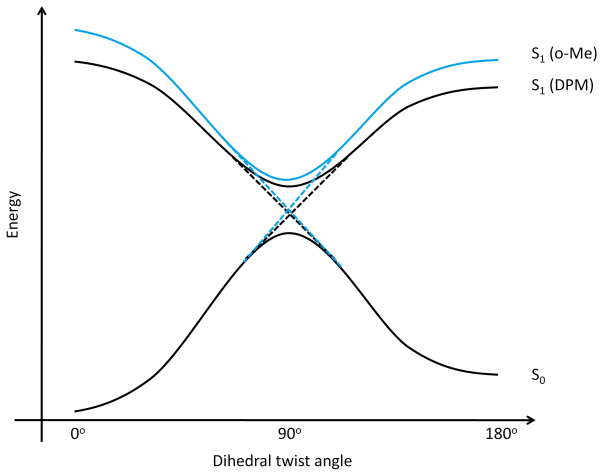

Figure 5.16: Schematic of the potential energy curves required for isomerization in o-Me and DPM.

photo-excitation generates a wavepacket at the Franck-Condon region which quickly moves (500 fs) towards the S_1 minimum penetrating the conical intersection. Here due to the potential energy curves slope the re-population of the orange isomer ground state (680 fs) occurs faster than the population the blue isomer ground state (1.7 ps).

5.4.2 Para - Sulfur Methyl Substitution

The rate at which isomerization occurs in the p-SMe substituted DPM molecule compared to the unsubstituted DPM as seen in table 5.3 is significantly slower suggesting a higher stability in the excited state. Apart from these kinetic differences between p-SMe and DPM, all of the wavelength maximum values are also red shifted. The implication of this dominant red-shift is that photo-induced isomerization requires less energy. Again the reasoning here is that increased elongation of the delocalized π orbitals (see figure 5.17) on the dithizonate backbone is akin to increasing the width of the potential well for a quantum mechanical particle trapped in a one dimensional box. The result of this is that the energy level spacings in the well decreases which explains the increase in excitation wavelength.

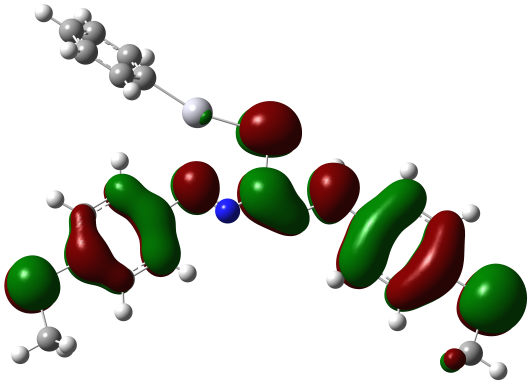

(a) p-SMe

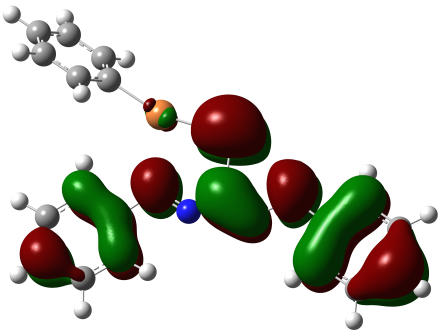

(b) DPM

Figure 5.17: Orange isomer of (a) para (p)-SCH_3(or SMe) and (b) DPM together the density plot of the HOMO for both.

An overview of the photo-induced isomerization pathway for p-SMe as compared to DPM is illustrated in figure 5.18. As the spectral data indicated the excited state S_1 for p-SMe is substantially lower than that of DPM. This means that the gradient of S_1 around the conical intersection region is very shallow, which supports the rather long lifetime (1.54 ps) of the excited orange state measured for p-SMe.

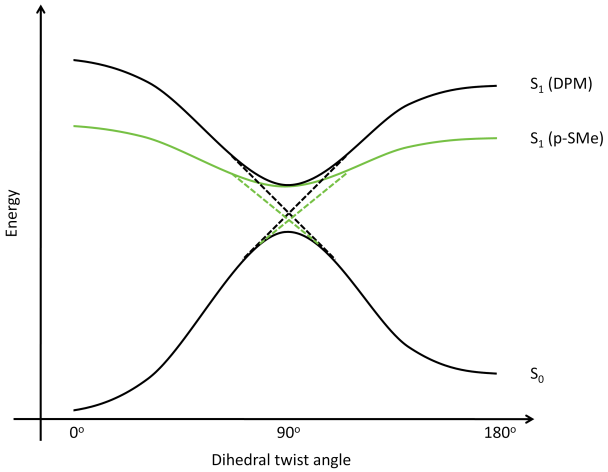

Figure 5.18: Schematic of the potential energy curves required for isomerization in p-SMe and DPM.

The slope also directly influences the formation (in 530 fs) of the intermediate state which subsequently have a longer lifetime (3.6 ps). This long lifetime serves as a bottleneck for the population of the orange isomer (in 3.79 ps) and the blue isomer (in 3.6 ps). Here this bottleneck phenomenon is valid seeing that radiationless decay through a conical intersection between the excited state S_1 and the ground state S_0 at orthogonal arrangement is the only channel, because no fluorescence is present (see appendix A).

6. Conclusions and Outlook

The body of work contained in this dissertation serves to increase the knowledge base for photo-induced processes. More particularly the photo-induced *cis-trans* isomerization around a C=N double bond, which is found in the photochromic test sample dithizonatophenylmercury(II) (DPM). DPM consists of two ligands (dithizonate and phenyl) which are complexed to a mercury. The dithizonate backbone has nitrogen rich conjugations which means DPM is a good light absorber and makes it an interesting metal complex because of the strong photochromism it exhibits in solution when illuminated with blue-green light. The colour change is from orange to blue, which indicates the disappearance of the reactant and appearance of the product making it ideal to be investigated through conventional ultrafast transient absorption spectroscopy (UTAS). UTAS was therefore performed on DPM in solution allowing for a description of the initial photochromic reaction which includes the dynamics and pathways involved in the isomerization process.

For UTAS purposes, the photochromic reaction for DPM in solution was initialized with a 40 fs pulse which had a center wavelength ($\lambda_0 \approx 470$ nm) close to the steady state absorption maximum (in the visible spectrum) of the orange isomeric form. This ultrashort pump pulse, excites the system from the ground electronic state S_0 to the first excited state S_1, where due to the bandwidth ($\Delta\lambda \approx 18$ nm) of the pulse a number of vibrational levels are simultaneously populated. The simultaneous (coherent) population of the vibrational levels result in the formation of a molecular wavepacket which propagate on the potential energy surface (PES) of S_1. Since the information of the dynamics and isomerization pathway is set by the motion of this molecular wavepacket, a whitelight continuum generated in a $3-5$ mm thick calcium fluoride crystal is used as probe pulse to resolve albeit partially resolve its motion. This is because the accompanying spectral changes which occur as the wavepacket moves are detected only within the whitelight wavelength range ($340-680$ nm). The main spectral features which were identified through UTAS was an excited state absorption band, the reactant's ground state band, an intermediate specie band and the product's ground state band. These features were temporally resolved down to the setup's temporal resolution of roughly 60 fs, giving a glimpse of the dynamics of the wavepacket which is not accessible in steady state spectroscopy.

From these measurements and theoretical evidence on similar but smaller molecular systems it was concluded that the photoinduced C=N isomerization reaction of DPM proceeds on the excited-state potential energy surface S_1 towards a conical intersection with the ground state S_0

located at orthogonal geometry along the twist coordinate. Once here the molecular wavepacket funnels through onto the ground-state PES where the reaction pathway splits with almost equal probability to the blue photoproduct and the orange reactant ground state. The latter being evident from the partial repopulation of the reactant. It was found that this initial photoreaction of DPM occurs in a variety of solvents (methanol, deuterated methanol and dichloromethane) and is completed in about 2 ps. The slight variations in time constants and spectral features which were seen in the UTA data for DPM dissolved in the solvents were attributed to variations in the PESs for the three solute-solvent systems.

Apart from the slight solvent effect, DPM was also electronically altered and studied through UTAS. The electronic alteration was done through the substitution of functional groups (-CH_3, -OCH_3, -SCH_3, -Cl and -F) with different electron affinities to the dithizonate backbone. It was shown that these alterations either slowed down (4 ps) or sped up (1 ps) the initial photochromic reaction, which was determined to be the result of the electronic disturbances to the delocalized π electron orbital distribution across the backbone. These electronic disturbances subsequently alters both the highest occupied molecular orbitals and the lowest unoccupied molecular orbitals of the different DPM derivatives leading to variations in the PESs.

Besides the photo-induced isomerization reaction from the orange isomeric form to the blue isomeric form of DPM, the reverse reaction was also investigated. Seeing that the reverse reaction is a thermal one, the lifetimes of the photo-product was determined through measuring the absorbance changes of the blue isomeric form as a function of time. From these measurements, a rather large solvent dependence was found in the lifetime of the blue photo-product. For example, the blue isomer of DPM dissolved in dichloromethane had a lifetime of 795 s, whilst for DPM dissolved in toluene it was determined as 47 s. Furthermore, in the case of the DPM derivative molecules, it was found that the lifetime of the photo-product depends more on sterical effects then it does on the electronic effects. Lastly, the thermal relaxation of the blue isomeric form towards the orange isomeric form, allowed for Arrhenius type measurements to be conducted. In these measurements the decay rate as a function of temperature is used to determine the potential energy barrier (64.8 kJ/mol) of the reverse path for DPM when dissolved in toluene.

From the results of both the initial photochromic reaction and the back reaction one question still remains. Is the back reaction also photo-active? If it turns out that the blue isomeric form can be optically changed to the orange isomeric form, it would make DPM an ideal system for molecular switching. Therefore further investigations on the reversibility of isomerization for DPM is still envisaged. A possible method to determine the optical reversibility is to design a

UTA system with two pump pulses and one probe pulse. The one pump pulse can be set to the wavelength for the forward reaction (reactant absorption), and the other pump pulse set to the wavelength for the possible reverse reaction (product absorption). During a measurement like this the delay between the two pump pulse can be sequentially changed as to see the effect this has on the yield of the reactant and product. Thus being proof of photo-activated molecular switching between the two isomeric forms.

APPENDIX A
Fluorescence Detection

In order to support the notion that the photo-excited DPM molecule and its derivatives in solution undergo non-radiative decay. It is vital to determine if any fluorescence is detectable. To this end a fluorescence quantum yield measurement for DPM dissolved in methanol is conducted. This particular measurement involves the referencing of the fluorescence quantum yield for DPM to a molecule with a known value. The reference molecule that is chosen, is 4- dicyano-methylene-2-methyl-6-p-dimethylaminostiryl- 4 H-pyran (DCM-not to be confused with dichloromethane) which like DPM absorbs light quite strongly in the blue part of the visible spectrum, but unlike DPM fluoresce in the red part of the visible spectrum. This photo-behaviour together with the fact that the fluorescence quantum yield for DCM is known made it an ideal candidate [44].

In order to quantify the quantum yield the single-point measurement technique is used in which the yield for DPM Q is expressed as follows,

$$Q = Q_{ref} \frac{I}{I_{ref}} \frac{OD_{ref}}{OD} \frac{n^2}{n_{ref}^2}. \tag{A.1}$$

Here Q_{ref} is the fluorescence quantum yield for DCM, I/I_{ref} the ratio of the measured fluorescence intensity of DPM to DCM, OD_{ref}/OD the ratio of the optical density of DCM to DPM at the excitation wavelength and finally n^2/n_{ref}^2 the ratio of the refractive indices of the solvents used. Seeing that the Q_{ref} for DCM is known the subsequent task is to determine the fluorescence intensities and optical densities of DPM and DCM. The optical densities of DPM and DCM at the excitation wavelength of 470 nm is determined through conventional UV/Vis steady state spectroscopy as $OD = 57300$ $M^{-1}{\cdot}cm^{-1}$ and $OD_{ref} = 42000$ $M^{-1}{\cdot}cm^{-1}$ respectively. However the measurement of the fluorescence intensities requires a fluorescence setup . Therefore a fluorescence setup was built (see figure A.1). Using this setup the fluorescence intensity values at 630 nm are $I = 50$ counts for DPM and $I_{ref} = 13801$ counts for DCM.

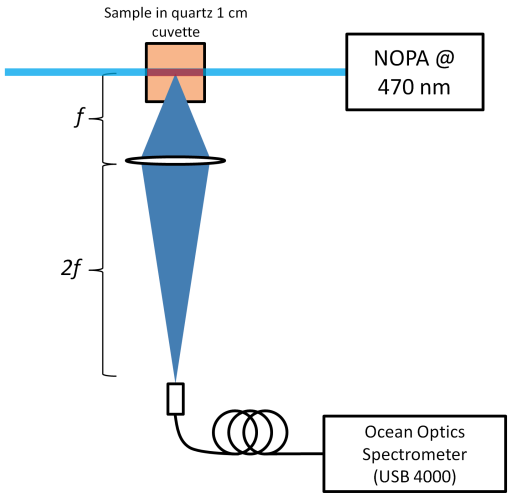

Figure A.1: Sketch of the fluorescence setup: The NOPA was used to generate light at 470 nm which is directed to the sample (DPM or DCM) in a 1 cm quartz cuvette. The fluorescence is then imaged using a lens ($f = 50$ mm) onto a fiber-coupled spectrometer (fiber diameter of 300 μm).

Lastly, the ratio of the refractive indices in eq. A.1 is however neglected because methanol is used as solvent for both DPM and DCM. Taking all the values into account it is determined using eq. A.1 that the fluorescence quantum yield for DPM dissolved in methanol is $Q = 1.14 \times 10^{-4} \approx 10^{-4}$. This low value for the quantum yield verifies that no flourescence in the visible spectrum is detected.

BIBLIOGRAPHY

[1] B. Honig, A. Warshel, and M. Karplus, Acc. Chem. Res. **8**, 92 (1975).

[2] M. Yan, D. Manor, G. Weng, H. Chao, L. Rothberg, T. M. Jedju, R. R. Alfano, and R. H. Callender, Proc. Nati. Acad. Sci. **88**, 9809 (1991).

[3] J. Kim, M. Tauber, and R. Mathies, Biochemistry **40**, 13774 (2001).

[4] G. Zgrablic, A. Novello, and F. Parmigiani, J. Am. Chem. Soc. **134**, 955 (2012).

[5] M. Klessinger and J. Michl, *Excited States and Photochemistry of Organic Molecules* (VCH, Weinheim, 1995).

[6] S. A. Kovalenko, R. Schanz, H. Hennig, and N. P. Ernsting, J. Chem. Phys. **115**, 3256 (2001).

[7] C. Jiang, R. Xie, F. Li, and R. Allen, Chem. Phys. Let. **474**, 263 (2009).

[8] S. Kovalenko, A. Dobryakov, I. Ioffe, and N. Ernsting, Chem. Phys. Let. **493**, 255 (2010).

[9] L. S. Meriwether, E. C. Breitner, and C. L. Sloan, J. Am. Chem. Soc. **87**, 4441 (1965).

[10] K. von Eschwege, J. Conradie, and J. Swarts, J. Phys. Chem. A **112**, 2211 (2008).

[11] H. Schwoerer, K. von Eschwege, G. Bosman, P. Krok, and J. Conradie, Chem. Phys. Chem. **12**, 2653 (2011).

[12] A. H. Zewail, J. Phys. Chem. A **104**, 5660 (2000).

[13] M. Ziolek, J. Kubicki, A. Maciejewski, R. Naskrecki, and A. Grabowska, Phys. Chem. Chem. Phys. **6**, 4682 (2004).

[14] S. Lochbrunner, K. Stock, and E. Riedle, J. Mol. Struc. **700**, 13 (2004).

[15] A. Yamaguchi, N. Nakagawa, K. Igarashi, T. Sekikawa, H. Nishioka, H. Asanuma, and M. Yamashita, Appl.Surf. Sci. **255**, 9864 (2009).

[16] T. Ngele, R. Hoche, W. Zinth, and J. Wachtveitl, Chem. Phys. Let. **272**, 489 (1997).

[17] R. de Vivie-Riedle, V. De Waele, L. Kurtz, and E. Riedle, J. Phys. Chem. A **107**, 10591 (2003).

[18] C. Schriever, M. Barbatti, K. Stock, A. Aquino, D. Tunega, S. Lochbrunner, E. Riedle, R. de Vivie-Riedle, and H. Lischka, Chem. Phys. **347**, 446 (2008).

[19] T. Wilhelm, J. Piel, and E. Riedle, Opt. Let. **22**, 1494 (1997).

[20] G. Yang and Y. R. Shen, Opt. Let. **9**, 510 (1984).

[21] A. Brodeur and S. L. Chin, J. Opt. Soc. Am. B **16**, 637 (1999).

[22] W. Liu, O. Kosareva, I. S. Golubtsov, A. Iwasaki, A. B. V. P. Kandidov, and S. Chin, Appl. Phys. B **75**, 595 (2002).

[23] A. Couairon, Phys. Rev. A **68**, 015801 (2003).

[24] A. K. Dharmadhikari, F. A. Rajgara, N. C. S. Reddy, A. S. Sandhu, and D. Mathur, Opt. Express **12**, 695 (2004).

[25] A. K. Dharmadhikari, F. A. Rajgara, and D. Mathur, Appl. Phys. B **80**, 61 (2005).

[26] A. Couairona and A. Mysyrowicz, Phys. Rep. **441**, 47 (2007).

[27] V. Kartazaev and R. R. Alfano, Opt. Let. **32**, 3293 (2007).

[28] G. G. Luther, J. V. Moloney, A. C. Newell, and E. M. Wright, Opt. Let. **19**, 862 (1994).

[29] W. Liu and S. Chin, Opt. Express **13**, 5750 (2005).

[30] R. L. Fork, C. V. Shank, C. Ifirlimann, R. Yen, and W. J. Tomlinson, Opt. Let. **8**, 1 (1983).

[31] A. Brodeur, F. Ilkov, and S. Chin, Opt. Comm. **129**, 193 (1996).

[32] W. Liu, S. Petit, A. Beckera, N. Akozbek, C. Bowden, and S. Chin, Opt. Comm. **202**, 189 (2001).

[33] C. Nagura, A. Suda, H. Kawano, M. Obara, and K. Midorikawa, Appl. Opt. **41**, 3735 (2002).

[34] M. Kolesik, G. Katona, J. Moloney, and E. Wright, Appl. Phys. B **77**, 185 (2003).

[35] A. K. Dharmadhikari, F. A. Rajgara, and D. Mathur, Appl. Phys. B **82**, 575 (2006).

[36] M. Lorenc, M. Ziolek, R. Naskrecki, J. Karolczak, J. Kubicki, and A. Maciejewski, Appl. Phys. B. **74**, 19 (2002).

[37] U. Megerle, I. Pugliesi, C. Schriever, C. Sailer, and E. Riedle, Appl. Phys. B **96**, 215 (2009).

[38] V. Bonacic-Koutecky and J. Michl, Theo. Chim. Acta **68**, 45 (1985).

[39] T. Arai, Y. Furuya, and K. Tokumaru, J. Photochem. Photobio. A **97**, 133 (1996).

[40] S. Ameer-Beg, S. M. Ormson, R. G. Brown, P. Matousek, M. Towrie, E. T. J. Nibbering, P. Foggi, and F. V. R. Neuwahl, J. Phys. Chem. A **105**, 3709 (2001).

[41] S. Zilberg and Y. Haas, Photochem. Photobiol. Sci. **2**, 1256 (2003).

[42] I. Conti, M. Garavelli, and G. Orlandi, J Am Chem Soc **130**, 5216 (2008).

[43] M. Han, D. Ishikawa, E. Muto, and M. Hara, J. Lum. **129**, 1163 (2009).

[44] J. M. Drake, M. L. Lesiecki, and D. M. Camaiont, Chem. Phys. Lett. **113**, 530 (1985).

[45] J. Mondal, S. Verma, H. Ghosh, and D. Palit, J. Chem. Sci. **120**, 45 (2008).

[46] K. Appenroth, M. Reichenbcher, and R. Paetzold, J. Photochem. **14**, 51 (1980).

[47] Y. Liu, B. Tang, H. Shen, S. Zhang, and B. Zhang, Opt. Express **18**, 5791 (2010).

[48] S. Yoon, P. Kukura, C. Stuart, and R. Mathies, Mol. Phys. **104**, 1275 (2006).

[49] R. Minns, D. Parker, T. Penfold, G. Worth, and H. Fielding, Phys. Chem. Chem. Phys. **12**, 15607 (2010).

[50] S. Matsika and P. Krause, Ann. Rev. Phys. Chem. **62**, 621 (2011).

[51] D. Polli, P. Altoe, O. Weingart, K. Spillane, C. Manzoni, D. Brida, G. Tomasello, G. Orlandi, P. Kukura, R. Mathies, et al., Nature **467**, 440 (2010).

[52] C. Middleton, K. de La Harpe, C. Su, Y. Law, C. Crespo-Hernandez, and B. Kohler, Ann. Rev. Phys. Chem. **60**, 217 (2009).

[53] D. R. Yarkony, Rev. Mod. Phys. **68**, 985 (1996).

[54] D. R. Yarkony, Acc. Chem. Res. **31**, 511 (1998).

[55] B. Kaduk and T. V. Voorhis, J. Chem. Phys. **133**, 061102 (2010).

[56] H. Hirai and O. Sugino, Phys. Chem. Chem. Phys. **11**, 4570 (2009).

[57] K. Appenroth, M. Reichenbcher, and R. Paetzold, J. Photochem. **14**, 39 (1980).

[58] K. Appenroth, M. Reichenbcher, and R. Paetzold, Tetrahedron **37**, 569 (1981).

[59] L. S. Meriwether, E. C. Breitner, and N. B. Colthup, J. Am. Chem. Soc. **87**, 4448 (1965).

[60] D. Lide, ed., *CRC Handbook of Chemistry and Physics: 75th Edition* (CRC Press, Inc., 1994).

[61] M. J. Frisch, G. W. Trucks, H. B. Schlegel, G. E. Scuseria, M. A. Robb, J. R. Cheeseman, G. Scalmani, V. Barone, B. Mennucci, G. A. Petersson, et al., *Gaussian 09 Revision A.1*, gaussian Inc. Wallingford CT 2009.

[62] O. Olaoye, Master's thesis, Stellenbosch University (2012).

[63] M. Boggio-Pasqua, M. J. Bearpark, P. A. Hunt, and M. A. Robb, J. Am. Chem. Soc. **124**, 1456 (2002).

[64] C. Ciminelli, G. Granucci, and M. Persico, Chem. Phys. **349**, 325 (2008).

[65] G. Kohler and K. Rechthaler, Pure & Appl. Chem **65**, 1647 (1993).

[66] B. Schwartz and P. Rossky, J. Chem. Phys. **105**, 6997 (1996).